STUDY OF TRANS-RECTAL NEAR-INFRARED DIFFUSE OPTICAL TOMOGRAPHY CONCURRENT WITH TRANS-RECTAL ULTRASOUND FOR PROSTATE IMAGING

By

ZHEN JIANG

Master of Science

Southeast University

Nanjing, China

2005

Submitted to the Faculty of the
Graduate College of the
Oklahoma State University
in partial fulfillment of
the requirements for
the Degree of
DOCTOR OF PHILOSOPHY
May, 2010

STUDY OF TRANS-RECTAL NEAR-INFRARED DIFFUSE OPTICAL TOMOGRAPHY CONCURRENT WITH TRANS-RECTAL ULTRASOUND FOR PROSTATE IMAGING

Dissertation Approved:

Dr. Daqing Piao

Dissertation Adviser

Dr. Jerzy Krasinski

Dr. Charles F. Bunting

Dr. Wei Chen

Dr. Albert T. Rosenberger

Dr. A. Gordon Emslie

Dean of the Graduate College

ACKNOWLEDGMENTS

First of all, I owe my greatest gratitude to my advisor, Dr. Daqing Piao, for sharing his abundance of knowledge and experience with me. He always found time to help me not only on research projects, but also on the writing and presentation. He is the most enthusiastic and encouraging advisor I have ever met. I learned a lot from his guidance and his own accomplishments.

I would like to acknowledge Dr. Bunting for teaching me electromagnetic theory and advising me on revision of the study report.

I also thank Dr. Rosenberger for helping me thoroughly understand the theory in "Physical Optics" which helped me build the imaging system and solve various problems.

Thanks Dr. Krasinski for his support on the devices and optical parts with which the numerous phantom tests of optical system can be successfully completed.

I am very grateful to Dr. Chen from University of Central Oklahoma, who is a pioneer on photoimmune response in the therapeutic application of light. He took two hours round trip to attend my preliminary exam, qualify exam and final defense. He also gave sharp critiques to my studies.

I am also particularly indebted to Dr. Bartels, Dr. Holyoak and Dr. Ritchey in Center for Veterinary Health Sciences. With their great clinical collaborations, the studies that lead to this dissertation have been demonstrated *in-vivo* with tumor models. They kindly interpreted the ultrasound imaging and pathology results and discussed the details of the operation with me.

Many thanks to my group members Guan Xu, Yuan Yuan Jiang, Anqi Zhang and Wei Sun, former group members Hao Xie and Cameron for all the fruitful as well as unfruitful discussions on the research.

At last, I would like to thank for my father Benshan Jiang, my mother Chengmei Sun, and my parent-in-law Renliang Zhu and Peixin Shi. Without their help, I would not get to the end of my PhD study.

This dissertation is finally dedicated to family, my wife Xianglan Zhu and my son Dylan Jiang, who give me great support, encouragement and happiness in my doctoral studies.

The research in this dissertation is mainly supported by the project "Trans-rectal Near-Infrared Optical Tomography for Prostate Imaging" from DOD prostate cancer research program (PC060814).

.

TABLE OF CONTENTS

LIST OF TABLES

LIST OF FIGURES

CHAPTER I

INTRODUCTION

Prostate cancer has been the most common non-skin cancer and the second leading cause of cancer-related death, affecting 1/6 American men. It is 35% more likely to be diagnosed with prostate cancer for a man than a woman is to be diagnosed with breast cancer [1]. The estimated new cases and deaths in 2009 by National Cancer Institute in United States are: 218,890 (New cases) and 27,050 (Deaths) [2]. Although only 1 in 10,000 under age 40 will be diagnosed, the rate shoots up to 1 in 39 for ages 40 to 59, and 1 in 14 for ages 60 to 69. In fact, more than 65% of all prostate cancers are diagnosed in men over the age of 65. The roles of race and family history are important as well. African American men are 61% more likely to develop prostate cancer compared with Caucasian men and are nearly 2.5 times as likely to die from the disease. Men with a single first-degree relative—father, brother or son—with a history of prostate cancer are twice as likely to develop the disease, while those with two or more relatives are nearly four times as likely to be diagnosed. The risk is even higher if the affected family members were diagnosed at a young age.

1.1 Prostate cancer

Human prostate (Fig. 1) is a gland in the male reproductive system. It surrounds the part of the urethra (the tube that empties the bladder) just below the bladder, and produces a fluid that forms part of the semen. The urethra runs directly through the prostate, the rectum, or the lower end of the bowel, sits just behind the prostate and the bladder. The seminal vesicles, two little glands that secrete about 60% of the substances that make up semen are above the prostate. What running alongside and attached to the sides of the prostate are the nerves that control erectile function.

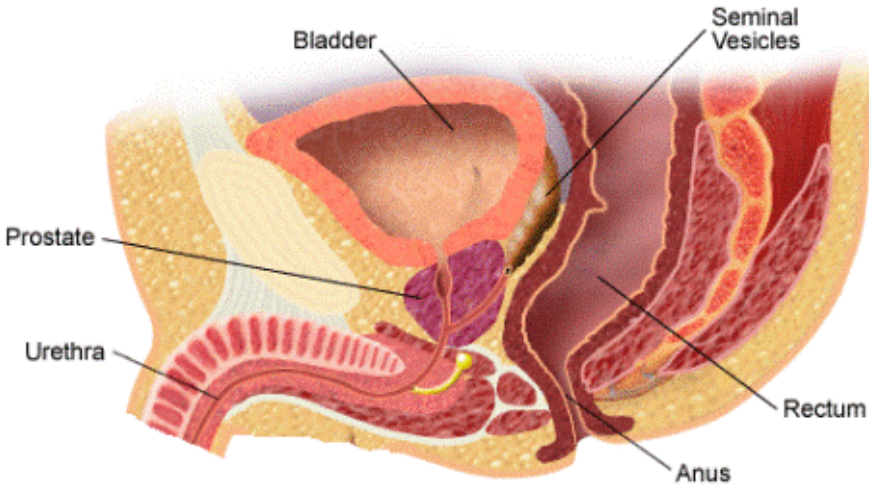

Figure 1 Human Prostate

In 1988, McNeal divided prostate anatomically into several zones which were shown in Fig. 2 with sagittal view and coronal view [3]. Those three zones include: Peripheral Zone (PZ) covering the dorsal, lateral and apical parts of the prostate; Transition Zone (TZ) consists of two lobes, located anteriorly between the proximal urethra and the lateral parts of the PZ; Central Zone (CZ) is cone-shaped with its base at the bladder neck and the tip at the verumontanum. Studies showed that about 68% of

prostate cancers arise in the PZ, 24% and 8% of other cancers arises in TZ and CZ respectively [4]~[6].

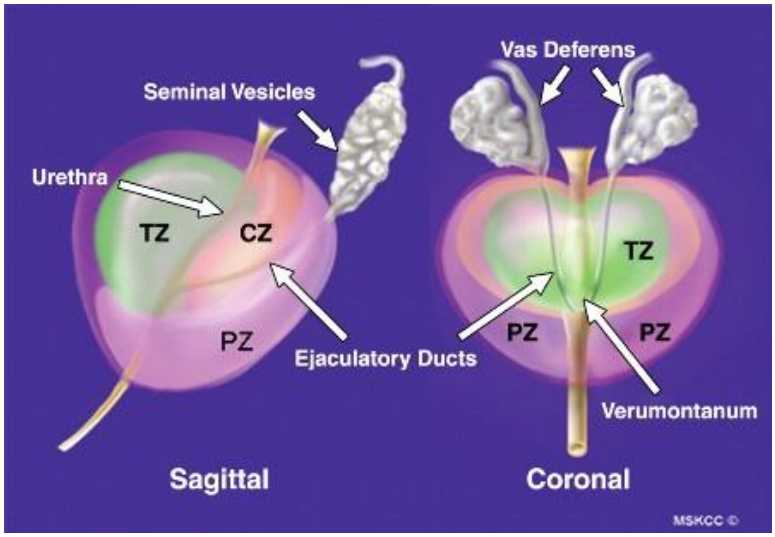

Figure 2 Anatomic zones of prostate:

PZ: peripheral zone; TZ: transition zone; CZ: central zone

Prostate cancer is hard to evaluate because of its unusually wide range of biological potential between incidence and mortality. Some patients died quickly after diagnosis while others could live as long as normal life span. Current prediction of prognosis for prostate cancer by combined histological grading and clinical staging was introduced by Gleason et, al., in 1974. The four stages of prostate cancer are described in Fig. 3. Stage I (Localized): cancer found in the prostate only; Stage II (Localized): cancer is more advanced but has not spread outside the prostate; Stage III (Locally advanced): cancer which has spread beyond the outer layer of the prostate to nearby tissues; Stage IV (Advanced/ metastatic): cancer has spread to other parts of the body [7][8].

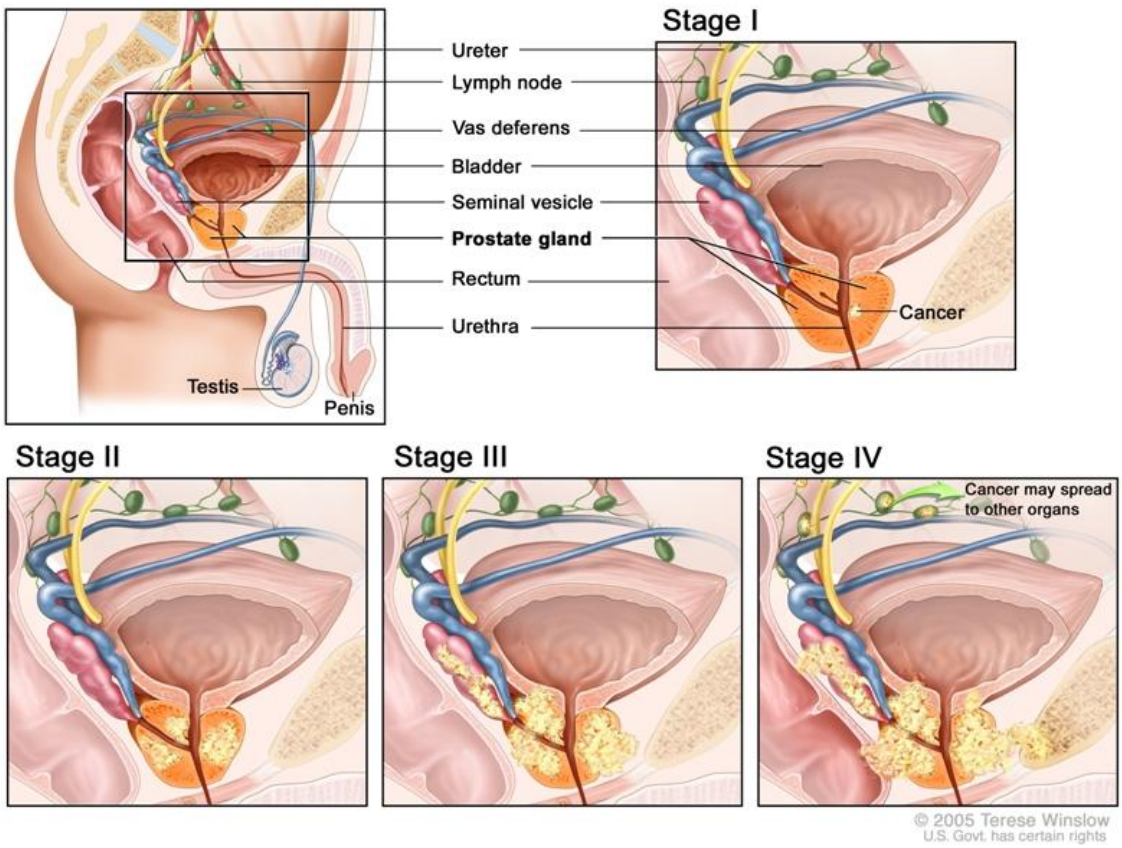

Figure 3 Different stages of prostate cancer

The Gleason grading system in Fig. 4 shows a five distinct patters of how prostate cancer cells awkward from normal tissue cells. Gleason 1 means that the tumor cells look almost the same as normal cells while Gleason 5 shows that the tumor cells look much different to normal cells. During the examination, pathologist assigns one Gleason grade to the most common pattern and a second Gleason grade to the next most common pattern. The sum of those two grades determines the patient's Gleason score [7].

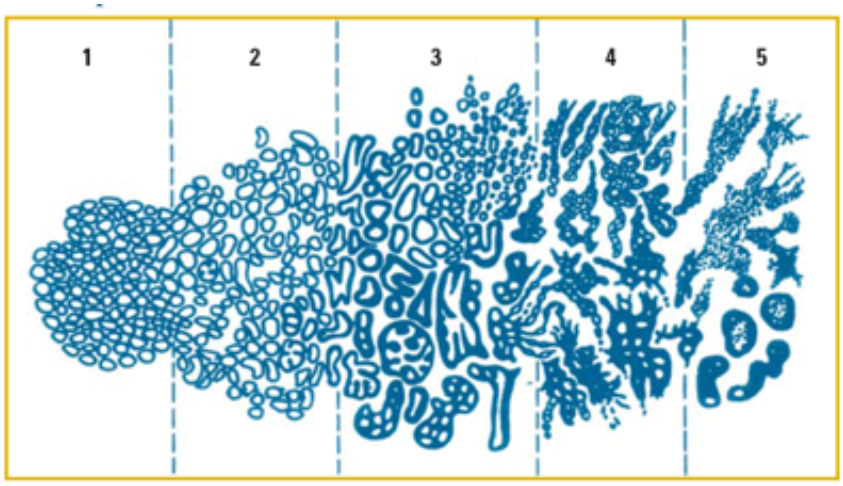

Figure 4 Gleason grading of prostate cancer [8].

1.2 Prostate cancer screening

Currently, prostate cancer early screening is performed by measurement of serum prostate-specific antigen (PSA), digital rectal examination (DRE) and a combination of these two tests. PSA is a protein produced by the prostate and released in very small amounts into the bloodstream. When there is a problem with the prostate, such as prostate cancer development and growth, more and more PSA is released, until it reaches a level where it can be easily detected in the blood. During a PSA test (Fig. 5a), a small amount of blood is drawn from the arm, and the level of PSA is measured. PSA levels less than 4 ng/mL are usually considered "normal," levels over 10 ng/mL are usually considered "high," and results between 4 and 10 ng/mL are usually considered "intermediate." However, PSA can also be elevated if other prostate problems are present and some men with prostate cancer may have "low" levels of PSA.

Another technique, DRE (Fig. 5b), is also used to detect the presence of disease as well. During a DRE exam, the experienced physician inserts a gloved, lubricated finger into the rectum and examines the prostate for any irregularities in size, shape, and texture.

Usually, the DRE can be used by urologists to help distinguish between prostate cancer and non-cancerous conditions [9]~[11].

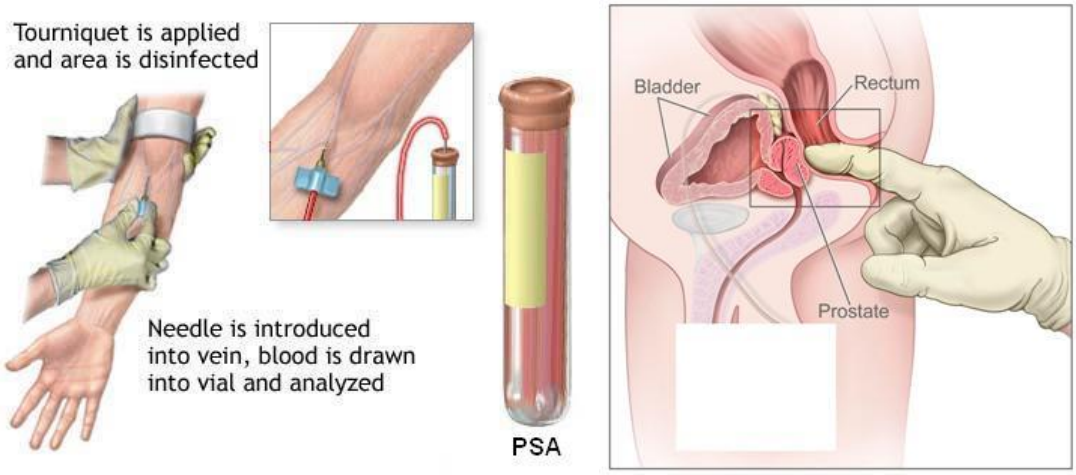

(a) (b)

Figure 5 Prostate screening PSA (a) and DRE (b)

In prostate detection, the sensitivity is defined by:

$$Sensitivity = \frac{Number \text{ of true positive results}}{Number \text{ of true positive results} + Number \text{ of false negative results}}$$

Equation 1

while the specificity is defined by:

$$Specificity = \frac{Number \text{ of true negative results}}{Number \text{ of true negative results} + Number \text{ of false positive results}}$$

Equation 2

and the detection rate is an averaged value of sensitivity and specificity.

Among those exams mentioned above, Prostate specific antigen (PSA) test turns on the alert of prostate cancer very early; however, because of the distribution of cancer and PSA in the population, the sensitivity and specificity of PSA for cancer detection for levels of 1.1, 2.6 and 4.0 mg/L are 83.4%/38.9%, 40.5%/81.1%, and 20.5%/93.8%,

respectively. The higher sensitivity of the PSA test will give lower specificity of the prostate cancer; while on the contrary, the higher specificity of the PSA level setting will lead to a lower sensitivity of the PSA test. The majority of the positive test results have been demonstrated as the false alarm between 60~70%. PSA test also has approximately 15% of false negative reassurance rate.

Digital rectal examination (DRE) augments PSA test when the nodule is palpable, but the sensitivity of DRE is low which mainly depends on the experience of physicians. Up to 20% of men with abnormal DRE results have prostate cancer; on the other hand, 60% of men with prostate cancer have normal DRE results. Among those prostate cancers detected by DRE alone, 70% of them have already spread beyond the prostate gland.

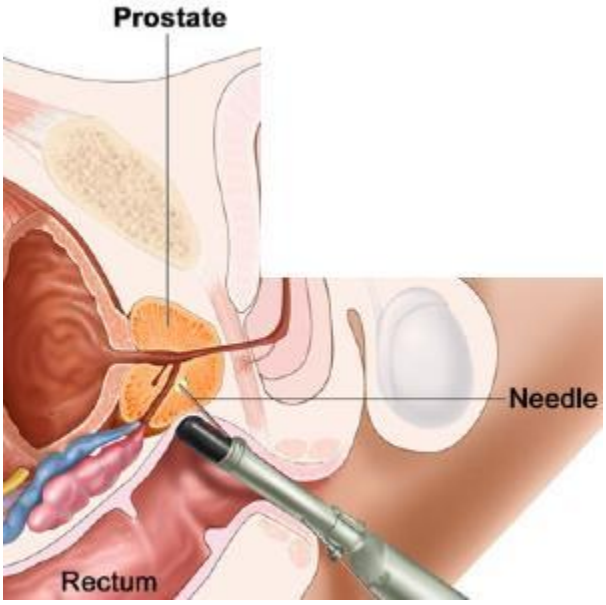

Figure 6 TRUS guided prostate biopsy

When there is a suspicion of prostate cancer, a biopsy must be taken to obtain the pathologic evidence as well to confirm neoplastic lesions and to determine their clinical significance for treatment planning. Currently, trans-rectal ultrasound (TRUS) guided prostate biopsy is the gold-standard of prostate cancer diagnostic. In TRUS-guided biopsy (Fig. 6), a biopsy needle loaded in a spring-action automatic biopsy device is commonly used to procure multiple prostate biopsy specimens. The tissue samples have to be taken throughout the prostate at minimum of 6 sites as a systematic yet random approach. The current standard of prostate biopsy routinely uses 10 to 12 cores of tissue obtained throughout the prostate for the initial assessment. Pathologists examined the biopsy samples under the microscope to tell if there are prostate cancer cells and how they grow. A cancer grade (Gleason Score) is to determine the degree how the tumor cells look different from normal cells. It should be noted that the majority of biopsies are found to be negative, and in men with persistent suspicion of prostate cancer after several negative biopsies, repeated biopsy and more extensive protocols (>12 cores) up to saturation biopsy (24 cores) represent a necessary diagnostic procedure [14][15].

1.3 Prostate imaging techniques

There are several imaging techniques that have been applied to prostate imaging. Among them: Ultrasonography, Magnetic Resonance Imaging (MRI), Computed Tomography (CT) and Positron Emission Tomography (PET) are the main imaging techniques in clinical applications or in the research [16].

Ultrasonography is a technique in which high-frequency sound waves are bounced off internal organs, with the echo pattern converted into a two-dimensional image of the structures beneath the transducer. For prostate imaging, trans-rectal

ultrasonography is the most commonly used imaging technique to determine the prostate size, zonal anatomy and potential lesions because of its portability, low cost and capability to perform real-time imaging [17].

MRI, formerly called nuclear magnetic resonance imaging (NMRI), uses a powerful magnetic field to align the nuclear magnetization of hydrogen atoms in water in the body. Radio frequency field is used to systematically alter the alignment of this magnetization, causing the hydrogen nuclei to produce a rotating magnetic field detectable by the scanner. MRI allows anatomical and functional assessment of the prostate which has better soft-tissue resolution than any other imaging method enabling more-accurate lesion detection and local staging [18].

CT is a technique with ionizing radiation that uses multiple two-dimensional X-ray images, taken around a single axis of rotation to generate a three-dimensional image of an object. Although it is a widely used modality in both diagnosis and follow-up of nearly all malignancies, it has limited role in the imaging of prostate cancer due to its poor soft-tissue contrast resolution. The major role of CT in prostate imaging is for the detection of bony involvement and in nodal staging [19].

PET is a nuclear medicine imaging technique which produces a three-dimensional image of functional processes in the body. It detects pairs of gamma rays emitted by a positron-emitting radionuclide (tracer), which is introduced into the body on a biologically active molecule. Images of tracer concentration in 3-dimensional or 4-dimensional space within the body are then reconstructed by computer analysis. PET has high sensitivity with only a small amount of radioactive compound. Its signal is

proportional to tracer which makes it a quantitative imaging method except a limited spatial resolution [20].

Considering the advantages of imaging speed and system expense, current standard prostate biopsy procedure is guided by trans-rectal ultrasound (TRUS) when indicated by elevated serum prostate-specific antigen (PSA) levels or abnormal digital rectal examination (DRE) [21][22].

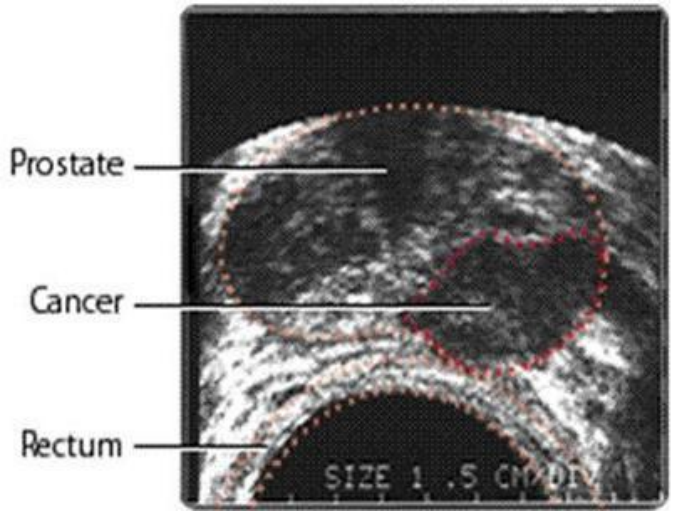

Figure 7 TRUS image of prostate cancer

However, TRUS has some unique limitations on the prostate cancer diagnosis. Fig. 7 is an axial trans-rectal ultrasound image of prostate. Although the resolution of the sono-graphic imaging of the prostate is high enough to define the prostate region from the capsule, the contrast of ultrasound imaging cannot reliably tell the lesion from the normal tissue. Statistically less than 60% of neoplastic lesions appear hypoechoic on TRUS while most of the remaining neoplastic lesions appear isoechoic. Therefore, most of the ultrasound guided biopsies performed following a “systematic sampling” strategy. Some templates with 6~12 cores cover two lobes (prostate right lobe and left lobe) from cranial aspect to caudal aspect. Although some advanced techniques like Doppler-ultrasound

may detect the regions of hyper-vascularity, but most small tumors are not angiogenic that limits this technique in the prostate cancer diagnosis at early stage. The ultrasonographic finding of the classic hypoechoic peripheral zone lesion has a sensitivity of 85.5%, specificity of 28.4%, positive predictive value of 29%, negative predictive value of 85.2% and overall accuracy of 43% in prostate cancer detection. The prevalence of isoechoic or nearly invisible prostate cancers visualized with TRUS ranges from 25 to 42%. As a result, the overall cancer detection rates for patients undergoing repeat prostate needle biopsy with various biopsy templates range from 10% - 38%[23]~[28].

Since there are no significant biologic differences noted between isoechoic and hypoechoic prostate cancers, TRUS does not reliably differentiate neoplastic from benign tumors. Improving the cancer detection rate using TRUS-guided biopsy requires TRUS imaging be augmented or aided with a potentially pathognomonic indicator of prostate cancer development that can be detected non-invasively [29][30].

1.4 Near-infrared diffuse optical tomography

Near-infrared (NIR) diffuse optical tomography (DOT) has been demonstrated as a non-invasive diagnostic imaging technique with high functional contrast between the malignant tissue and normal tissue since 1970s. This optical measurement has several centimeter imaging depth in tissue because the tissue is dominated by water which has low absorption in NIR region (600~1000nm).

Recently near-infrared diffuse optical tomography approach has been widely used to detect breast cancer, by providing sufficient contrast between the normal breast tissue and the lesion [31]~[36]. Some groups, including ours, have extended this method toward prostate imaging. It has been suggested that the accuracy of prostate biopsy may be

improved if the TRUS imaging could be augmented with a functional or "surrogate" marker of a prostate tumor. Based on decades of research on cancer imaging and prostate measurements, near-infrared (NIR) tomography, being non-ionizing and minimally-invasive similar to TRUS, has the potential of providing such functional or "surrogate" markers. NIR optical tomography, if carried out trans-rectally, may improve the specificity of TRUS imaging such that prostate biopsies could be directed to the most suspicious lesions [37]~[39].

1.5 Thesis overview

The objectives of this work are to develop an endo-rectal NIR imaging applicator coupled with TRUS in sagittal plane, to validate the performance of the trans-rectal NIR tomography with or without the incorporation from the TRUS *prior*, and to demonstrate the combined trans-rectal US/NIR system by *in-vivo* experiments with animal model. The successful outcome of this research will pave the way to increase the imaging contrast and help radiologists to locate the suspicious lesions in the prostate which will ultimately improve the biopsy accuracy.

Chapter I is a brief introduction of the prostate cancer and commonly used prostate cancer imaging and diagnostic methods. In Chapter II, a review of the NIR diffuse optical tomography describes the optical imaging reconstruction algorithm in detail. Previous studies on the prostate optical measurement are also presented in Chapter II. Chapter III describes the design of the combined endo-rectal US/NIR imaging applicator and system. Chapter IV provides comprehensive experimental results to validate the combined imaging system. The *in-vivo* optical measurements on canine prostate with a tumor model are reported in Chapter V at single wavelength. Dual-band

optical imaging on canine prostate with tumor model to map the prostate total hemoglobin concentration and oxygen saturation is presented in Chapter VI.

CHAPTER II

NEAR INFRARED DIFFUSE OPTICAL TOMOGRAPHY

In near–infrared (NIR) diffuse optical tomography, illumination from several sources into a diffuse medium is observed by several detectors. A model for light propagation in a diffuse-dominant medium is applied to localize the optical properties of target. The first optical imaging of bio-tissue could be traced back to 1920s of the trans-illumination experiment through breast originally proposed by Cutler [40]. With the derivation of theory and the development of the techniques, multiple wavelength optical measurements to quantify the oxygen and de-oxygen hemoglobin concentration was introduced in 1970s by Jobsis [41] which was considered as the most important demonstration of the potential NIR spectroscopic measurement for tissue volume. In recent NIR imaging studies on human subjects, the contrast of hemoglobin of cancerous tissue and normal tissue has been estimated within the range of 2:1 to 3:1. This chapter will introduce some basic concepts and the imaging reconstruction algorithm of this technique [42]~[46].

When light propagates through the biological tissue, the attenuation of the light power was caused by optical absorption and optical scattering which can be obtained by diffuse optical tomography (DOT).

2.1 Optical absorption

Optical absorption in molecular transitions includes electronic transition and vibrational transition. Electronic transition allows electrons to move freely up and down the different energy levels (or quantum states). In vibrational transition, the nuclei of the atoms within a molecule vibrate resonantly with wavelengths in the infrared spectrum. For pure optical absorbing medium, the relation between the attenuation of light power I and the optical path-length l follows a relation which was discovered by Bouguer (1729) and Lambert (1760) [46]:

$$\frac{I}{I_0} = e^{-\mu_a l} \qquad \text{Equation 3}$$

Where I is the light intensity after passing through the medium and I_0 is the incident light intensity, l (mm) is the optical path length, and μ_a is the absorption coefficient (mm^{-1}).

In 1852, Beer found that the compound optical absorption was related to the concentration C of those absorbing species in the medium which can be expressed as:

$$\mu_a(\lambda) = \varepsilon_1(\lambda)\cdot c_1 + \varepsilon_2(\lambda)c_2 + \cdots + \varepsilon_n(\lambda)c_n = \sum_{i=1}^{n} \varepsilon_i(\lambda)c_i \qquad \text{Equation 4}$$

Then Equ. 4 becomes:

$$\frac{I}{I_0} = e^{-\mu_a l} = e^{-\sum_i^n \varepsilon_i(\lambda)c_i} \qquad \text{Equation 5}$$

Where ε_i is the extinction coefficient (mm^{-1}/Mol) with respected to different wavelength λ and c_i is the concentration of the species in the medium (Mol).

2.2 Optical scattering

Light scattering occurs when charged particles in a medium are set into oscillatory motion by the electric field of the incident wave and re-emit light of the same frequency as the primary wave. This re-radiation pattern is in the form of a dipole pattern. As the dipoles collapse and re-radiate their energy, the radiation patterns from all dipoles will interfere destructively in the off-axis directions and will constructively interfere in the forward and backward directions. The time delay in the process of dipole formation and re-radiation after dipole collapse causes a slower light speed than that in vacuum. The ratio of those two different speeds is presented by refractive index:

$$n = \frac{c_0}{c_m} \qquad \text{Equation 6}$$

Where c_0 is the light speed in vacuum, and c_m is the light speed in the medium.

The scattering coefficient μ_s is defined as the probability of photon scattering in a medium per unit path length. For single scattering, it can be expressed as:

$$\mu_s = \rho_s \sigma_s \qquad \text{Equation 7}$$

Where ρ_s is the concentration of the scattering objects and σ_s is the scattering cross-section which can be described as:

$$\sigma_s = Q_s A \qquad \text{Equation 8}$$

Where Q_s is the scattering efficiency and A is the area of the cross-section.

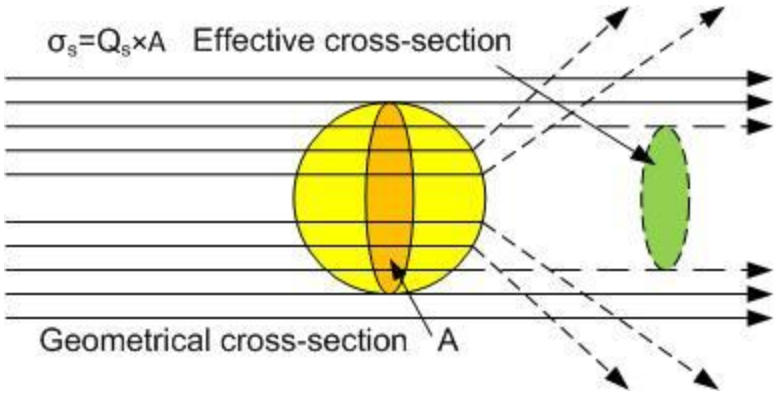

Figure 8 Optical scattering

Another parameter often used in biomedical optics is the reduced scattering coefficient:

$$\mu_s' = (1-g)\mu_s \qquad \text{Equation 9}$$

The "anisotropy" g is the projection of the scattered angle θ onto the forward direction as the following equation:

$$g = \langle \cos(\theta) \rangle = \int_0^{\pi} p(\theta)\cos(\theta)\cdot 2\pi \sin(\theta)\cdot d\theta \qquad \text{Equation 10}$$

For biological tissues, a typical value for g is in the range of 0.90~0.95 The probability density function $p(\theta)$ for isotopic scattering which is equal at all directions is $\frac{1}{4\pi}$. For a given value of g, a commonly used scattering function in biomedical optics is the Henyey-Greensein phase function:

$$p(\theta) = \frac{1}{4\pi}\cdot\frac{1-g^2}{\left(1+g^2-2g\cos\theta\right)^{\frac{3}{2}}} \qquad \text{Equation 11}$$

When a photon travels in a tissue, it travels one mean free path (MFP= $\frac{1}{\mu_S}$) before being scattered. And after traveling a "reduced mean free path" (MFP'= $\frac{1}{\mu_S'}$), it becomes isotropic scattering.

In biological tissue, large objects like mitochondria, nuclei and collagen fiber bundles are usually comparable or larger than the wavelength of NIR light. The scattering pattern is dominated by Mie scattering which is wavelength dependant. Studies have found an empirical relation between the reduced scattering and different wavelength.

$$\mu_s = a\lambda^{-b} \qquad \text{Equation 12}$$

Where *a* is the scattering amplitude and *b* is the scattering power. The value of both scattering power and amplitude depend on the scatterer size and density. For large scatterers, *b* and *a* values are usually lower than small scatterers. When the scatterer size is much smaller than the wavelength, *b* is close to 4 as expected from Rayleigh scattering. Table 1 lists some measured scattering amplitude and power of different tissues from previous studies.

Table 1 Fitted scattering amplitude and power of biological tissue

Study	Phantom (λ in μm)	Amplitude	Power
Saidi et al, 1995 [47]	1% Intralipid	1.41	0.758
Solonenko et al, 2002 [48]	Bowel (canine)	0.70	1.24
Solonenko et al, 2002 [48]	Kidney (canine)	1.23	1.51
Solonenko et al, 2002 [48]	Prostate (canine)	0.97	0.876
Srinivasan et al, 2007 [49]	Breast (Human)	1.2±0.25	0.7±0.44
Svensson et al, 2008 [50]	Prostate (human)	31	1.6

2.3 Diffusion approximation

As the electromagnetic wave propagation described by Maxwell's equations, the propagation of light in turbid media can be expressed by the radiative transport equation (RTE). The time domain RTE is [51]~[54]:

$$\left(\frac{1}{c_m}\cdot\frac{\partial}{\partial t}+\hat{s}\cdot\nabla+\mu_{tr}(r)\right)\phi(r,\hat{s},t)=\mu_s(r)\int_{S^{n-1}}\Theta(\hat{s}\cdot\hat{s}')\phi(r,\hat{s}',t)d\hat{s}'+q(r,\hat{s},t) \qquad \text{Equation 13}$$

where c_m is the velocity of light in the medium, $\phi(r,\hat{s},t)$ is the number of photons per unit volume at position r and time t with velocity in direction $\hat{s}$. $\Theta(\hat{s},\hat{s}')$ is the normalized scatter phase function giving the probability of photon scattering from direction $\hat{s}$ to $\hat{s}'$. $q(r,\hat{s},t)$ is the light source at r and time t travelling in direction $\hat{s}$. $\hat{s}$ is a normalized vector that can be expressed as:

$$\hat{s}=\begin{pmatrix}\sin\vartheta & \cos\varphi\\ \sin\vartheta & \sin\varphi\\ \cos\vartheta & \end{pmatrix} \qquad \text{Equation 14}$$

The transport cross section $\mu_{tr}(r)=\mu_a(r)+\mu_s(r)$, where $\mu_a(r)$ and $\mu_s(r)$ are the absorption cross section and scattering cross section at position r accordingly.

RTE describes that the radiance at position r and direction $\hat{s}$ equals to the sum of all the mechanisms which increase the radiance minus those effects that reduce it.

When applying $\frac{\partial}{\partial t}\Leftrightarrow i\omega$, the frequency domain RTE can be derived as:

$$\left(\frac{i\omega}{c_m}+\hat{s}\cdot\nabla+\mu_{tr}(r)\right)\phi(r,\hat{s},\omega)=\mu_s(r)\int_{S^{n-1}}\Theta(\hat{s}\cdot\hat{s}')\phi(r,\hat{s}',\omega)d\hat{s}'+q(r,\hat{s},\omega) \qquad \text{Equation 15}$$

Since the RTE does not consider the wave effects, its application is focused on the wavelength much smaller than the dimensions of the study object. In optical tomography,

the solution for the light field at points in large 3D volume is extremely computationally expensive which motivates the need to develop a simpler model.

By using the spherical harmonics $Y_{n,m}$ the radiation ϕ and source term q in time domain expression can be expanded as [53]:

$$\phi(r,\hat{s},t)=\sum_{n=0}^{\infty}\sum_{m=-n}^{n}\phi_{n,m}(r,t)Y_{n,m}(\hat{s}) \qquad \text{Equation 16}$$

and $q(r,\hat{s},t)=\sum_{n}^{\infty}\sum_{m=-n}^{n}q_{n,m}(r,t)Y_{n,m}(\hat{s})$ Equation 17

The term for n=0 and m=0 represents the isotropic component, while the terms n=1 and m=0, ±1 are the anisotropic components. The larger the n becomes, the more accurate the approximation model is, but the computational expense will be increased quickly. When applying P_1 approximation and the assumption that the photon flux changes slowly and the light source is isotropic, the RTE becomes the following equations:

$$\left(\frac{1}{c_m}\cdot\frac{\partial}{\partial t}+\mu_a(r)\right)\Phi(r,t)+\nabla\cdot J(r,t)=q_0(r,t) \qquad \text{Equation 18}$$

and $\left(\frac{1}{c_m}\cdot\frac{\partial}{\partial t}+\frac{1}{3D(r)}\right)J(r,t)+\frac{1}{3}\nabla\Phi(r,t)=q_1(r,t)$ Equation 19

where the photon density $\Phi(r,t)=\int\phi(r,\hat{s},t)d\hat{s}$ and photon current $J(r,t)=\int\hat{s}\phi(r,\hat{s},t)d\hat{s}$

The diffusion approximation gives the assumption that the scattering is a dominant effect when light propagates in the medium, implying that $\mu_a << \mu_s'$ and requires the following relations [51]~[53]:

$$\frac{\partial J}{\partial t}=0 \text{ and } q_1=0,\ J(r,t)=-D\nabla\Phi(r,t)$$

Then the diffusion equation can be derived as:

$$-\nabla\cdot\kappa(r)\nabla\Phi(r,t)+\mu_a(r)\Phi(r,t)+\frac{1}{c_m}\cdot\frac{\partial\Phi(r,t)}{\partial t}=q_0(r,t) \qquad \text{Equation 20}$$

and the frequency domain form can be expressed as:

$$-\nabla\cdot\kappa(r)\nabla\Phi(r,\omega)+\mu_a(r)\Phi(r,\omega)+\frac{i\omega}{c}\Phi(r,\omega)=q_0(r,\omega) \qquad \text{Equation 21}$$

where $\kappa(r)$ and $\mu_a(r)$ are the diffusion coefficient and absorption coefficient respectively, and are functions of the position r.

2.4 Imaging reconstruction

The imaging reconstruction method used in this study is based on the software package called "Near Infrared Fluorescence and Spectral Tomography (NIRFAST)" which was developed by Dartmouth NIR Imaging research group. NIRFAST calculates the data acquired from the frequency domain measurement [55].

In the forward model, the frequency domain diffusion equation (Equ.21) was applied to calculate the photon fluence rate Φ at position r with modulation frequency ω based on the finite element method (FEM). The fluence rate $\Phi(r)$ can be approximated as [53]~[55]:

$$\Phi^h(r)=\sum_{i=1}^{V}\Phi_i u_i(r)\Omega^h \qquad \text{Equation 22}$$

where Ω^h is a finite dimensional subspace spanned by basis functions $\{u_i(r), i=1\ldots V\}$ chosen to have limited support. Then the diffusion equation in the FEM framework can be replaced by a system of linear algebraic equations [53]~[55]:

$$\Phi=\left[K(D)+C\left(\mu_a+\frac{i\omega}{c_m}\right)+\frac{1}{2A}F\right]^{-1}q_0 \qquad \text{Equation 23}$$

where

$$K_{i,j} = \int_{\Omega} D(r)\nabla u_i(r) \cdot \nabla u_j(r) d^n r$$

$$C_{i,j} = \int_{\Omega} \left[\mu_a(r) + \frac{i\omega}{c_m(r)} \right] u_i(r) u_j(r) d^n r$$

$F_{i,j} = \int_{\partial\Omega} u_i(r) u_j(r) d^{n-1} r$, and

$$q_{0_i} = \int_{\Omega} u_i(r) q_0(r) d^n r$$

At the boundary, NIRFAST adopts the type III boundary condition (known as Robin boundary condition) representing the boundary between air and tissue. The fluence at the tissue boundary exits but does not return. The flux leaving the external boundary is equal to the fluence rate at the boundary weighted by a factor that accounts for the internal reflection of light back into the tissue [55]:

$$\Phi(\xi,\omega) + 2A\hat{n} \cdot \kappa(\xi)\nabla\Phi(\xi,\omega) = 0 \qquad \text{Equation 24}$$

where ξ is a point on the external boundary, $\hat{n}$ is the outward pointing normal and A depends on the relative refractive index mismatch between the tissue and air.

$$A = \frac{\frac{2}{1-R_0} - 1 + \left|\cos(\theta_c)\right|^3}{1 - \left|\cos(\theta_c)\right|^2} \qquad \text{Equation 25}$$

where $\theta_c = \arcsin\left(\frac{n_{air}}{n_{tissue}}\right)$ and $R_0 = \frac{\left(\frac{n_{tissue}}{n_{air}} - 1\right)^2}{\left(\frac{n_{tissue}}{n_{air}} + 1\right)^2}$

Since those matrices K, C and F are sparse, the solution can be obtained by standard methods such as Cholesky reduction, substitution or biconjugate gradient in the

complex case. For 3D imaging, a direct sparse solver such as conjugate gradients can be applied [53].

The inverse problem is to solve the optical properties $\mu_a(r)$ and $D(r)$ at each FEM node. Assuming n×2 vector $x=(\mu_a, D)$, the objective of the inverse problem is to find the solution which minimizes the difference between the measurement and the calculation of the forward model based on Equ.23. The least square is the generally applied to seek the minimization of the residue [55][56]:

$$\min(\Psi):\ \Psi=\left\|\Phi^c(x)-\Phi^m\right\|^2=\left(\Phi^c(x)-\Phi^m\right)'\cdot\left(\Phi^c(x)-\Phi^m\right) \qquad \text{Equation 26}$$

where Φ^c and Φ^m are the calculated and measured optical fluence. In order to avoid the ill-conditioned and singular matrix that could give non-unique solutions, Tikhonov regularization is applied and the minimization objective becomes:

$$\min(\Psi):\ \Psi=\left\|\Phi^c(x)-\Phi^m\right\|^2+\lambda\left\|x-x_0\right\|^2 \qquad \text{Equation 27}$$

where λ is regularization factor defined as the ratio of the variances of the measurement data and optical properties $\lambda=\frac{\sigma^2_{\Phi^M}}{\sigma^2_x}$, and x_0 is the initial estimate of the optical properties which can be obtained from data calibration or *a priori* optical properties distribution. By taking the first order derivative of the objective and ignoring those higher order terms, Equ.27 becomes:

$$\frac{\partial\Psi}{\partial x}=0\Rightarrow\left(\frac{\partial\Phi^c}{\partial x}\right)^T\left(\Phi^m-\Phi^c\right)-\lambda\left(x-x_0\right)=0 \qquad \text{Equation 28}$$

where $\frac{\partial\Phi^c}{\partial x}$ is known as the Jacobian matrix J referring to the weighted or sensitivity matrix. In NIRFAST, which is a frequency domain imaging reconstruction algorithm, the

Jacobian matrix consists of 4 sub-matrices (amplitude I, phase θ, μ_a and D), which can be expressed as:

$$J = \begin{vmatrix} \frac{\delta \ln I_1}{\delta D_1} & \frac{\delta \ln I_1}{\delta D_2} & \cdots & \frac{\delta \ln I_1}{\delta D_N} & \frac{\delta \ln I_1}{\delta \mu_{a1}} & \frac{\delta \ln I_1}{\delta \mu_{a2}} & \cdots & \frac{\delta \ln I_1}{\delta \mu_{aN}} \\ \frac{\delta \theta_1}{\delta D_1} & \frac{\delta \theta_1}{\delta D_2} & \cdots & \frac{\delta \theta_1}{\delta D_2} & \frac{\delta \theta_1}{\delta \mu_{a1}} & \frac{\delta \theta_1}{\delta \mu_{a2}} & \cdots & \frac{\delta \theta_1}{\delta \mu_{aN}} \\ \frac{\delta \ln I_2}{\delta D_1} & \frac{\delta \ln I_2}{\delta D_2} & \cdots & \frac{\delta \ln I_2}{\delta D_N} & \frac{\delta \ln I_2}{\delta \mu_{a1}} & \frac{\delta \ln I_2}{\delta \mu_{a2}} & \cdots & \frac{\delta \ln I_2}{\delta \mu_{aN}} \\ \frac{\delta \theta_2}{\delta D_1} & \frac{\delta \theta_2}{\delta D_2} & \cdots & \frac{\delta \theta_2}{\delta D_N} & \frac{\delta \theta_2}{\delta \mu_{a1}} & \frac{\delta \theta_2}{\delta \mu_{a2}} & \cdots & \frac{\delta \theta_2}{\delta \mu_{aN}} \\ \vdots & \vdots & \vdots & \vdots & \vdots & \vdots & \vdots & \vdots \\ \frac{\delta \ln I_M}{\delta D_1} & \frac{\delta \ln I_M}{\delta D_2} & \cdots & \frac{\delta \ln I_M}{\delta D_M} & \frac{\delta \ln I_M}{\delta \mu_{a1}} & \frac{\delta \ln I_M}{\delta \mu_{a2}} & \cdots & \frac{\delta \ln I_M}{\delta \mu_{aN}} \\ \frac{\delta \theta_M}{\delta D_1} & \frac{\delta \theta_M}{\delta D_2} & \cdots & \frac{\delta \theta_M}{\delta D_N} & \frac{\delta \ln I_M}{\delta \mu_{a1}} & \frac{\delta \ln I_M}{\delta \mu_{a2}} & \cdots & \frac{\delta \ln I_M}{\delta \mu_{aN}} \end{vmatrix} \quad \text{Equation 29}$$

where M is the number of measurement and N is the FEM mesh nodes. With Jacobian Matrix, the Equ.28 could be replaced by following equation:

$$\left(J^T J + \lambda I\right)\delta x = J^T \delta\Phi - \lambda\left(x_i - x_0\right) \quad \text{Equation 30}$$

Assuming $\delta x = x_i - x_0$, then Equ.30 becomes:

$$\left(J^T J + 2\lambda I\right)\delta x = J^T \delta\Phi \quad \text{Equation 31}$$

In NIRFAST, the optical properties at all mesh nodes were updated in each iteration:

$$x_{k+1} = x_k + \alpha \cdot [J^T(x_k)J(x_k) + \bar{\lambda} I]^{-1} J^T(x_k)\Delta\Phi(x_k) \quad \text{Equation 32}$$

where $\bar{\lambda}$ is a penalty or regularization term, and another small term α is used to stabilize the convergence.

2.5 Continuous wave steady-state measurement

With the development of the analytic or numerical model of the DOT theory, there are several different measurement techniques which have been applied in DOT. The first is time-domain measurement provides information on the increased path length of light in tissue due to multiple scattering events, thus improving the ability to separately recover absorption and scattering properties [57][58]. The second is frequency-domain measurement, when the phase shift of a sinusoidal wave passing through a tissue volume is recorded, provide a less expensive and perhaps stable manner of acquiring time-based information [59][60]. The third one called Continuous Wave steady-state measurement uses the DC light source and directly measure the attenuation of the light power [61]~[63]. It was applied in the DC-based imaging reconstruction algorithm. Although time-domain and frequency-domain based methods may provide more optical information than CW approaches, a number of researchers have been interested in CW image reconstruction for several years, in part because of the relative simplicity, high signal-to-noise ratio, and low cost of CW techniques [64]. Recent studies have demonstrated that absorption and reduced scattering coefficients can be reconstructed quantitatively from steady-state measurements, by updating the D and μ_a distributions to minimize a weighted sum of the squared difference between computed and measured data [65]~[67]. The method is equivalent to performing the same minimization as Equ.27 by mapping the DC signal to frequency-domain, which has been utilized in the reconstruction of this study. A recent study showed that, when appropriate de-convolution is applied, CW data appears to provide significantly better spatial resolution than frequency-domain data. To date, significant progress in CW DOT has been made with both phantom and *in-vivo* clinical

data which suggests that research of CW DOT should be performed parallel to that of other methods.

In the continuous wave (CW) steady state measurement, ω=0, the diffusion equation for a photon density Φ at position $\vec{r}$ becomes [66]:

$$\nabla \cdot D(\vec{r})\nabla\Phi(\vec{r}) - \mu_a(\vec{r}) \cdot \Phi(\vec{r}) = -q(\vec{r}) \qquad \text{Equation 33}$$

For infinite homogeneous medium and semi-infinite medium, the diffusion equation has analytic solutions in spherical coordinates [67]:

$$\Phi_{Infinite} = \frac{S}{4\pi D\rho} e^{-k\rho} \qquad \text{Equation 34}$$

where $k = \sqrt{\frac{\mu_a}{D}}$

$$\Phi_{Semi} = \frac{S}{4\pi D l_r} e^{-kl_r} - \frac{S}{4\pi D l_i} e^{-kl_i} \qquad \text{Equation 35}$$

where $l_r = \sqrt{\rho^2 + R_a^2}$, $l_i = \sqrt{\rho^2 + (2R_b + R_a)^2}$, $R_a = \frac{1}{\mu_s'}$, R_b=2AD and ρ is the physical distance between the source and detector.

In inverse problem, the iteration follows the calculation same as the Equ.32. Since there is no phase information, the Jacobian matrix only includes the amplitude related items which becomes Equ.36 while the absorption coefficient and *D* are still both updated by the LM algorithm as Equ.32.

$$J_{CW} = \begin{vmatrix} \frac{\delta \ln I_1}{\delta D_1} & \frac{\delta \ln I_1}{\delta D_2} & \cdots & \frac{\delta \ln I_1}{\delta D_N} & \frac{\delta \ln I_1}{\delta \mu_{a1}} & \frac{\delta \ln I_1}{\delta \mu_{a2}} & \cdots & \frac{\delta \ln I_1}{\delta \mu_{aN}} \\ \frac{\delta \ln I_2}{\delta D_1} & \frac{\delta \ln I_2}{\delta D_2} & \cdots & \frac{\delta \ln I_2}{\delta D_N} & \frac{\delta \ln I_2}{\delta \mu_{a1}} & \frac{\delta \ln I_2}{\delta \mu_{a2}} & \cdots & \frac{\delta \ln I_2}{\delta \mu_{aN}} \\ \vdots & \vdots & \cdots & \vdots & \vdots & \vdots & \cdots & \vdots \\ \frac{\delta \ln I_M}{\delta D_1} & \frac{\delta \ln I_M}{\delta D_2} & \cdots & \frac{\delta \ln I_M}{\delta D_N} & \frac{\delta \ln I_M}{\delta \mu_{a1}} & \frac{\delta \ln I_M}{\delta \mu_{a2}} & \cdots & \frac{\delta \ln I_M}{\delta \mu_{aN}} \end{vmatrix} \qquad \text{Equation 36}$$

2.6 Optical measurement of prostate

The optical measurement of the prostate was initialized in the 1980s which mainly focused on the initial work on photodynamic therapy (PDT) by interstitial optical measurement. In the 1990s, an intraluminal fiber reflectometry was introduced for prostate measurement which made it possible for the internal noninvasive measurement of optical properties. The measurement compared the human prostate and dog prostate optical absorption and scattering within the wavelength from 650nm to 750nm. There have been a number of studies on prostate optical properties which have been summarized by Svensson in 2007 and Piao in 2009. Although these studies were conducted at different wavelengths, different samples and different methods, they offered invaluable information to understand the potentials of detecting prostate cancer and difficulties in terms of the prostate optical measurement [68]~[72]. The previous studies on the human prostate optical absorption, reduced scattering and effective coefficient are summarized in Table 2.

Table 2 Human prostate optical properties (cm^{-1})

Study	Description	λ(nm)	N	μ_a	μ'_s	μ_{eff}
Lee [73]	*in-vivo*, CW, untreated PC	630	7			3.5±0.7
Pantelides [74]	ex *vivo*, CW, normal whole prostates	633	3	0.7±0.2	8.6±0.5	4.3±0.5
Whitehurst [75]	*in-vivo*, CW, untreated BPH and PC	633	11			3.6±0.2
Lee [76]	*in-vivo*, CW, untreated BPH and PC	633	11			3.9±0.5
Wei et al. [77]	*in vitro*, CW, BPH	640	29	8.85~9.55	15.6~16.6	
Svensson [71]	*in-vivo*, TD, untreated PC	660	9	0.5±0.1	8.7±1.9	3.6±0.8
Lee [76]	*in-vivo*, CW, untreated BPH and PC	665	11			3.2±0.5
Zhu [78]	*in-vivo*, CW, recurrent PC	732	13	0.4±0.2	11.8±8.2	3.3±0.5
Zhu [79]	*in-vivo*, RC Pca	732	2	0.11~1.6	1.2~40	0.19~6.3
Li [80]	*in-vivo*, 2D map, RC Pca	732	1	0. 1~1	5~45	
Wang [81]	*in-vivo*, 3D map, RC Pca	732	1	0.1~0.7	1~55	
Weersink [82]	*in-vivo*, CW, recurrent PC	762	22	0.4±0.2	3.4±1.6	2.0±0.6
Svensson [71]	*in-vivo*, TD, untreated PC	786	9	0.4±0.1	7.1±1.6	2.9±0.7
Svensson [71]	*in-vivo*, TD, PCa	830	1	0.34	2.5~10	
Wei [77]	*in vitro*, CW, BPH	880	29	4.43~4.55	11.2-12.0	
Svensson [71]	*in-vivo*, TD, untreated PC	916	9	0.6±0.1	7.7±1.8	3.8±0.8
Sevensson [50]	*in-vivo*, TD, Pca	916	1	0.42	6.4	
Essenpreis [83]	*ex vivo* integrating sphere data, normal prostates	1064		1.5±0.2	6.4	
Roggan [84]	*ex vivo*, Normal	1064		0.03	0.4	0.2

In Table 2, CW means steady state data and TD is time resolved data. BPH is the benign prostatic hyperplasia and PC indicates the prostate cancer. All the measurements were performed invasively, and some of studies were aimed to measure the effective attenuation coefficient which can be expressed as:

$$\mu_{eff} = \sqrt{\frac{\mu_a}{D}} = \sqrt{3\mu_a\left(\mu_a + \mu_s'\right)} \qquad \text{Equation 37}$$

Previous research has demonstrated that the optical reduced scattering coefficient of prostate is around 10 times higher than prostate optical absorption coefficient which indicated that prostate can be considered as an optical scattering dominant tissue. The photon propagation in prostate can be modeled by the diffusion equation described in Equ.20 and Equ.21.

Studies also found the significant intersubject and intraorgan heterogeneities of human prostrates, different separation of the source and detector of PDT would give a different measured optical properties of absorption and scattering. The intraorgan heterogeneity gives a substantial challenge to differentiating malignant tissue from normal tissue and may also partially contribute to the similar effective attenuation coefficients of benign and malignant human prostate tissues [85].

It must be noted that none of the previous measurements of prostate optical heterogeneities have been examined on intact prostate *in-vivo*. In order to demonstrate if or which type of intrinsic optical property contrasts could be useful for differentiating the malignant prostatic tissue from benign or normal tissue, a system which aims at imaging the intact prostate in its real-time *in-vivo* condition is expected.

CHAPTER III

INSTRUMENTATION

There are several NIR tomography applicators designed for the brain imaging and breast imaging that employed well designed spherical or ring type NIR imaging probes. Prostate imaging requires different types of applicator as it is an internal organ in human body. The common size of the prostate is only 50mm along the maximum dimension which is much smaller than brain or breast as well. The feasible way to imaging prostate for NIR optical tomography is through the rectum while it brings some unique challenges particularly for the fabrication of an endo-rectal NIR applicator, which is more challenging if it is integrated with TRUS probe. First, the combination with ultrasound imaging system renders accurate and real-time anatomic information to correlate NIR optical system. The structural information obtained from TRUS may further provide the required *a priori* information to improve the accuracy of NIR image reconstruction; second, the axial dimension of the probe is restricted within 20~30mm (diameter). Thirdly, TRUS-coupled endo-rectal NIR applicator requires deploying many optodes in a very limited space. It has been suggested that arranging optodes longitudinally is an appropriate configuration that would allow interrogating deep prostate tissue in a sagittal imaging geometry [86]~[89].

3.1 Trans-rectal optical imaging applicator

According to the simulation study of different optode configurations on the trans-rectal imaging geometry, a proto-type of the combined TRUS coupled trans-rectal NIR imaging probe was fabricated by parallelly deploying 7 by 7 optical source and detector channels. The integrated sagittal-imaging trans-rectal NIR/US applicator consists of a custom-built NIR probe and a commercial bi-plane TRUS transducer (for canine prostate imaging), as shown in Fig.9. The bi-plane TRUS probe was equipped with a proximal 7.5MHz sagittal-imaging transducer and a distal 5MHz transverse-imaging transducer. The sagittal TRUS transducer occupies a 60mm×10mm window. The diameters of the sagittal and transverse imaging sections of the TRUS probe are 18mm and 20mm, respectively. Adapting to the un-even TRUS cross-section, the NIR applicator was fabricated to a cap-shape and attached to the TRUS probe (Fig. 9(a) ~ (e)). The NIR array substrate was machined from a black polycarbonate material to minimize the surface reflection. This substrate was then connected to an aluminum bracket and securely fastened to the TRUS handle using a bottom clamp. The rectangular TRUS handle (Fig.9 (f) ~ (g)) ensured aligning the NIR applicator to the TRUS transducer. A slot of 60mm×10mm was opened up in the NIR applicator to expose the sagittal TRUS transducer [90][91].

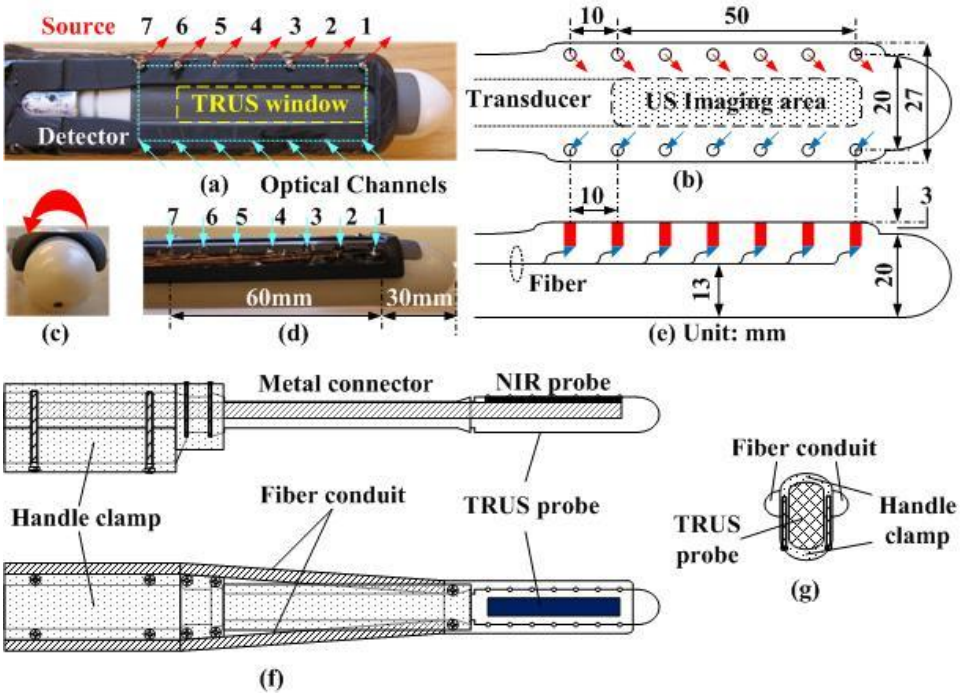

Figure 9 Design of combined trans-rectal US/NIR probe

The NIR probe consists of two linear-arrays, one for the source and the other for the detector, separated by 20mm and placed on each side of the sagittal TRUS transducer. Each linear-array consists of 7 channels spaced 10mm apart and covering 60mm in length. The 60mm long NIR array is aligned precisely with the 60mm window of the sagittal TRUS transducer.

A 600μm-core diameter (750μm with metal coating) fiber (Oxford Electronics HP SIR 600CB) is chosen for its thin cladding and mechanical strength. The 7 fibers of each linear-array are packaged into one groove of ~4mm×4mm in cross-section formed in the black substrate. Bending the fiber inside the small groove for side-firing at the probe surface is impractical. The minimum bend radius of this fiber for long term is 100 times of fiber radius which is 75mm (for short term is 40 times of the radius which is 30mm). Instead, micro-optics components were used for deflecting the light side-ways. As shown

in Fig. 10, each source channel includes 2 gradient-index (GRIN) lenses and 1 prism attached to the fiber while each detector channel has 1 GRIN lens and 1 prism attached to the fiber. The GRIN lens (Newport Corporation) has a pitch of 0.25, a diameter of 1mm, a length of 2.61mm, and a numerical aperture of 0.46. The prism is a coated 1mm right angle micro-prism with enhanced Aluminum coating on hypotenuse (Tower Optics) with reflection efficiency around 80%. Each fiber is polished and epoxied to a prism and a GRIN lens is attached to the other side of the micro-prism for illumination and detection at the probe surface. In this micro-optics assembling, under the monitoring by microscope, each piece was aligned accurately with other optical parts by home-designed stages and mounts with 3-dimension freedom for GRIN lens & Micro-prisms. The epoxy (NORLAND 81) with a viscosity of 300cps is hard and resilient. After curing, the epoxy has a refractive index of 1.56 and good adhesion to glass, metals and glass filed plastics. The optimum adhesion reached after room temperature aging for one week and it can be accelerated by aging at 50°C for 12 hours.

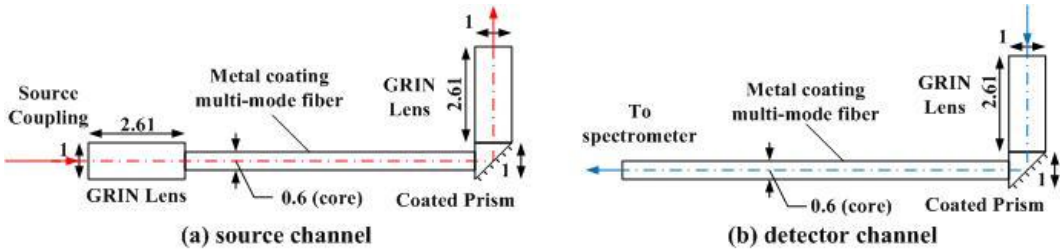

Figure 10 Micro-optics assembling of on-probe optical channels

As depicted in Fig. 10, each source channel has one GRIN lens attached to the proximal end of the fiber for coupling the light. The GRIN lens has larger diameter and numerical aperture than the metal-coated fiber that is expected to give a higher coupling efficiency for collimated light. Simulation by ZEMAX (ZEMAX Development Co.)

showed that for collimated incident beam using a GRIN lens and a prism gives 38% more coupling than without the GRIN lens (assuming micro-prism has 80% reflection at NIR band that is typical for enhanced aluminum coating). A coupling efficiency improvement of 10%~15% is observed experimentally from the completed fiber channels. The overall coupling efficiencies of the 14 home-assembled fiber channels are shown in Table 2. The overall coupling efficiency of each channel is about 50%, which could be improved if the assembly can be made more precise.

Table 3. Measured coupling efficiency of the source/detector fiber channels

Source channels	s1	s2	s3	s4	s5	s6	s7
Coupling efficiency	46%	48%	49%	49%	51%	43%	49%
Detector channels	d1	d2	d3	d4	d5	d6	d7
Coupling efficiency	54%	48%	49%	51%	53%	52%	50%

In the optical system design, there are two set up of optical systems that have been used for different application from system calibration to clinical application. One is called spectral-encoded system which was mainly used in experiments of system calibration for its highs speed data acquisition; the other is a source switching time-multiplex optical system which was applied during *in-vivo* animal experiments because of its higher coupled light power.

3.2 Spectral-encoded imaging system

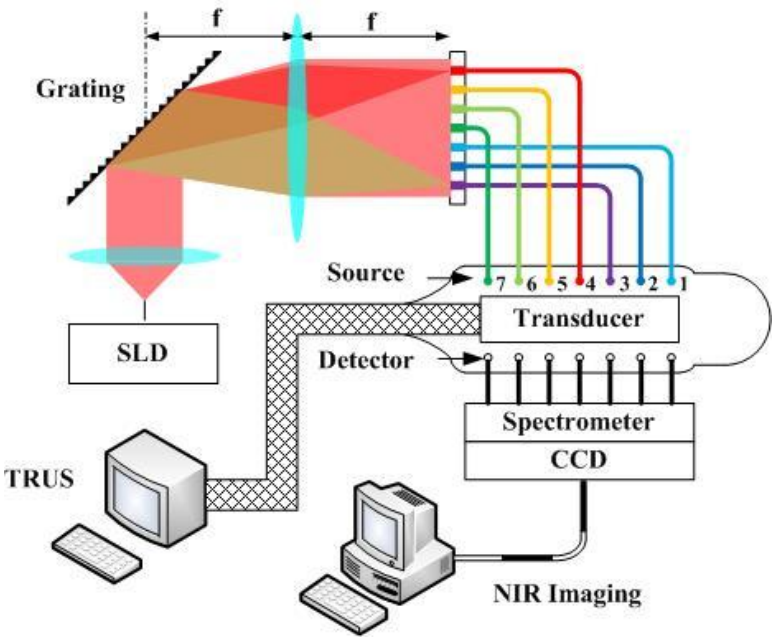

Figure 11 System diagram

In the system calibration, we use the spectral-encoded optical imaging system [92]~[94] which has a relative short data acquisition time (<200ms for most of the known value solid phantom experiments). The combined trans-rectal NIR/US imager is schematically illustrated in Fig. 11 and the photograph is given in Fig. 12. The US scanner is an ALOKA SSD-900V portable machine. The US images are transferred to the main computer of the combined imager by a PCI image acquisition card (National Instruments PCI-1405). For ALOKA SSD-900V US system, the calibrated US scanner range in longitudinal dimension is 50mm which corresponded to the optical channels from source/detector 1 to source/detector 6.

The NIR imager uses a custom-designed superluminescent diode (SLD) (Superlumdiodes Inc.) that is pigtailed to a multi-mode fiber and delivers 100mW of

840nm NIR light with 14.2nm FWHM bandwidth. In the schematic of Fig. 11, the SLD output beam is dispersed by a 1200 groves/mm grating. As described by Equ.37, different wavelength light will be dispersed into different directions and collimated unto linearly aligned 7 fibers connecting to the source channels on NIR applicator.

$$d(\sin\alpha + \sin\beta) = m\lambda \qquad \text{Equation 38}$$

Where *d* is the period constant of grating (1/1200 mm^{-1}), α and β are the incident and output angle of light (respected to the normal of the grating), *m* is the order of the diffraction (*0* means the none dispersed light beam/ specular reflection beam).

NIR light with slightly different wavelengths are coupled to the 7 fibers to form a spread-spectral-encoding of the source channels. In this system configuration, one source channel coupled around 1nm bandwidth light which centered at 840nm. The remitted lights collected by the 7 detection channels are coupled to a spectrometer (Acton Research 2300i). The signal corresponding to the individual source channels are discriminated horizontally by the spectrometer (1/1200 mm^{-1} grating). The signals corresponding to the individual detector channels are differentiated vertically based on the position of the detection channels on the spectrometer entrance slit. A 16-bit intensified CCD camera (Princeton Instruments PIMAX) acquires a complete set of NIR imaging data. The exposure time for one frame of data is in the range of 100s milliseconds, depending on the medium being imaged. When controlled by the software of Winspec, the CCD data acquisition time is set to the default value at 300ms. The NIR system resides on a custom-built cart that also houses the US scanner.

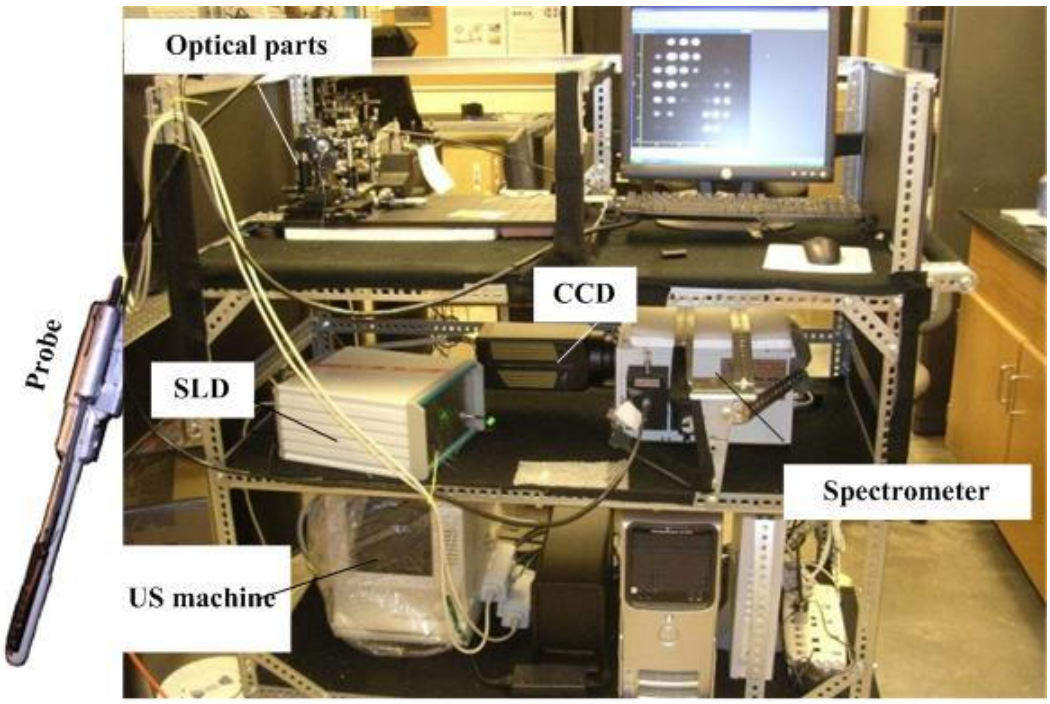

(b)

Figure 12 Spectral-encoded imaging system and photograph

The spectrometer (SpectraPro 2300i) has a focal length of 300mm-f/3.9. It has three different grove grating mounted in a rotational stage. The different resolutions of the different gratings are listed in Table 3:

Table 4 Parameters of SpectraPro 2300i

Grating	Resolution (per Pixel)
300	0.22nm
600	0.1nm
1200	0.046nm

The CCD was PI-MAX from Princeton instruments. It has a stand-alone controller ST-133 offering a data transferring at speed of 5M pixel/second and standard

video output for focusing and alignment. The basic parameters of the CCD are shown in the following table 4:

Table 5 Parameters of CCD

CCD ARRAY	WELL Capacity	Read Noise	Sensitivity
512×512 19×19μm	450 ke^- for single pixel; 1.2Me^- with binning	<8 e- rms@100kHz <35e- rms@1MHz <50e- rms@5MHz	1 to 80 ADU/photoelectron

The CCD was air cooled down to ~-20°C to reduce the amount of dark charge, which can improve the signal to noise ratio. The minimum value of the CCD image readout intensity is around 70 (Maximum is 65535), while the averaged value over one frame image (512×512) is around 90~100.

The 16bit CCD has a maximum dynamic range of 48dB, which may not be sufficient to accommodate the full dynamic range of the signals when a medium is highly absorptive, as the minimum and maximum source-detector distances of the trans-rectal NIR array are 20mm and 63mm, respectively. Reducing the total dynamic range of the signal is possible by proper use of the Gaussian spectrum of the SLD source. The actual light coupling configuration is given in Fig. 13(a), where the stronger spectral components are coupled to the peripheral NIR channels (such as 1 and 7), and the weaker spectral components are coupled to the middle NIR channels (such as 3-5). Comparing with the configuration of coupling the uniform light to all 7 source channels, the strategy in Fig. 13(a) offers a 15dB reduction of the overall signal dynamic range for a medium of

0.0023mm^{-1} absorption coefficient and 1.0mm^{-1} reduced scattering coefficient (equivalent to a 1% Intralipid solution) in Fig. 13(b).

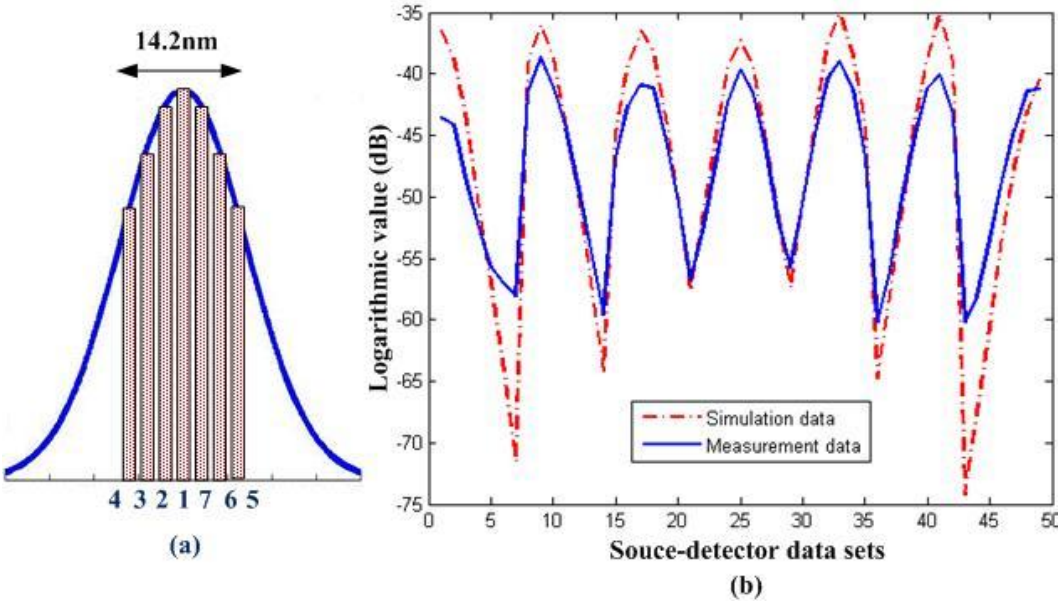

Figure 13 Spectral-encoded source coupling sequence

3.3 Switching-source optical imaging system

In the previous spectrum-encoded optical imaging system, the coupled light power efficiency with respect to the SLD output will be no higher than 40%. It mainly comes from the grating dispersion (~60% reflective efficiency at 1st order) and the lost light spectrum and the specular reflection cannot be coupled into source channels unless using some special designs. The averaged light power coupled in each optical channel is around 5mw. In the system calibration tests which mainly used the 1% intralipid as background, the coupled light power was acceptable which had an exposure time in the range of 100ms. When it is moved on to the tests of high absorptive bio-tissue like canine or human prostate (μ_a~0.01mm^{-1}), the acquisition time was much longer (>4s) in order to get the weakest signal. The longer data acquisition time will not only extend the

experiment time but also introduce strong noise into the measured data interfering the signals especially for those weak channels. In order to minimize the test time in the examination and improve the signal-to-noise ratio, strong light power was expected for each source channel. In Fig. 14, we coupled the entire SLD source power (100mw) into one source channel. A translation linear stage (Zaber Technologies) was used to switch the SLD light sequentially along the source channels from 1 to 7. The measured coupling efficiency of the switching setup before the source channel is over 95%. The exposure time at each source switch position is minimized to 100ms. The total test time with 7 channel switching is no more than 3 seconds which mainly relied on the readout time of CCD with a typical value of 309.6ms for each frame. The detection components of the system in Fig.14 are the same as previous spread-spectrum-encoded system described in section 3.2.

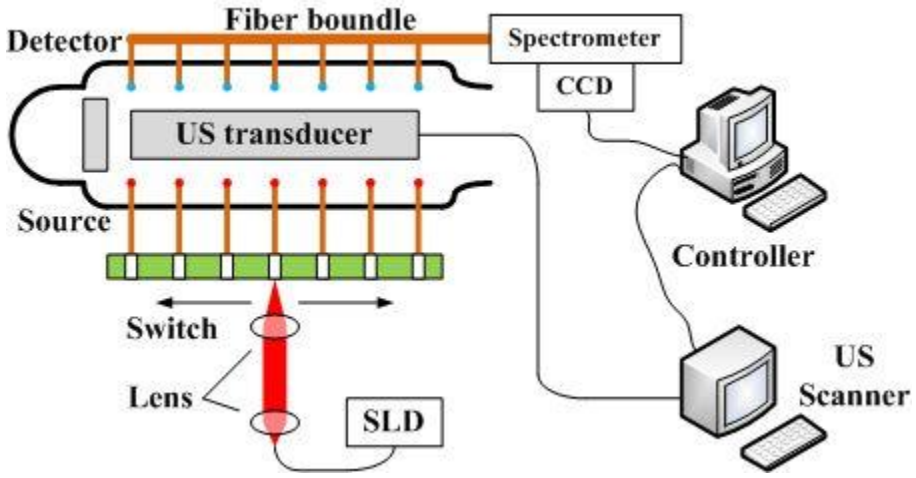

Figure 14 Switching source coupling system

The source switch was mainly built on a linear motorized slide (T-LSR 75B series from Zaber technologies Inc.). It has a built-in controllers and RS232 computer-interface with manual control. The maximum travel distance is 75mm and the maximum centered

load is 200N (44.9 lb.). The accuracy of the position is ±8μm while repeatability is <2.5μm. The liner stage is controlled by Labview8.5 program and the resolution of the minimum controllable step is 0.496μm. The translational slide is photographed in Fig. 15.

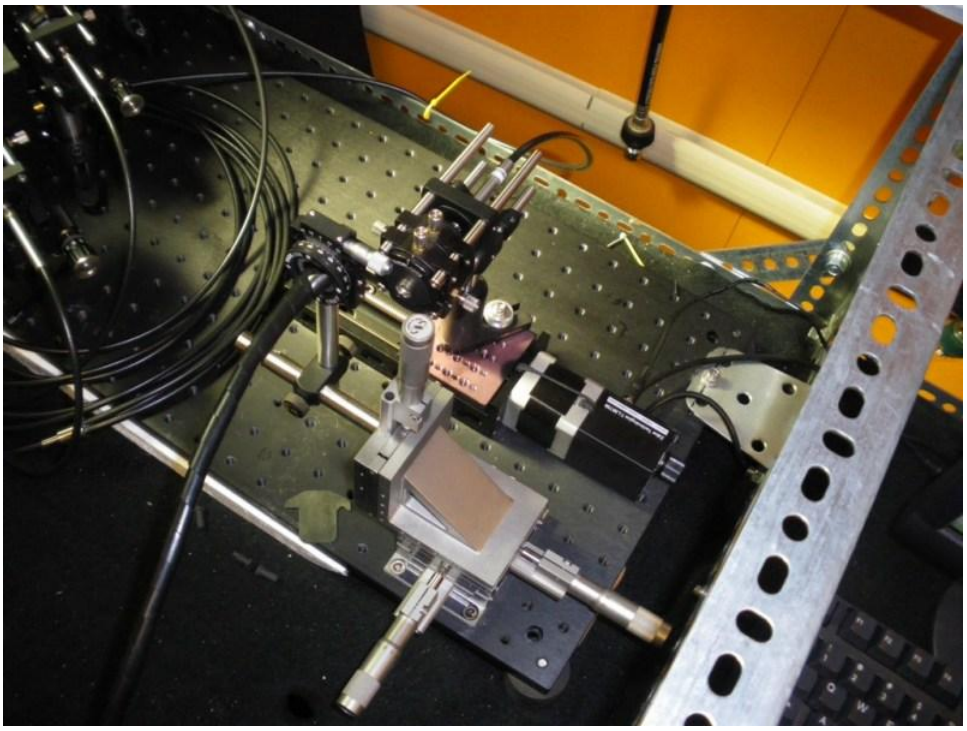

Figure 15 Photography of switching coupling system setup

The synchronization of the movement of the translation stage and CCD acquisition is the most important part in this time-multiplex switching system set up. Fig. 16 sketches the controller system diagram in which the CCD data acquisition is controlled by the software of Winspec by accepting the outside trigger signal. The triggered signal was generated by a DAQ/PCI card from the Labview program which controlled the translation stage movement.

PCI-6251 is a 16bit data acquisition card which has a sampling clock speed at 1MHz (multichannel)/1.25MHz (single channel). There are 16 differential/single-end analog input ports and 2 output ports.

The US scanner was also controlled by Labview to acquire and save the US images coupled to NIR images. The real-time ultrasound image was obtained by PCI-1405, single-channel color image acquisition (IMAQ) device, through a BNC cable connected with the output of the US scanner (Aloka US 900). The video output of the ultrasound scanner is the NTSC stream at 30 frames/s speed.

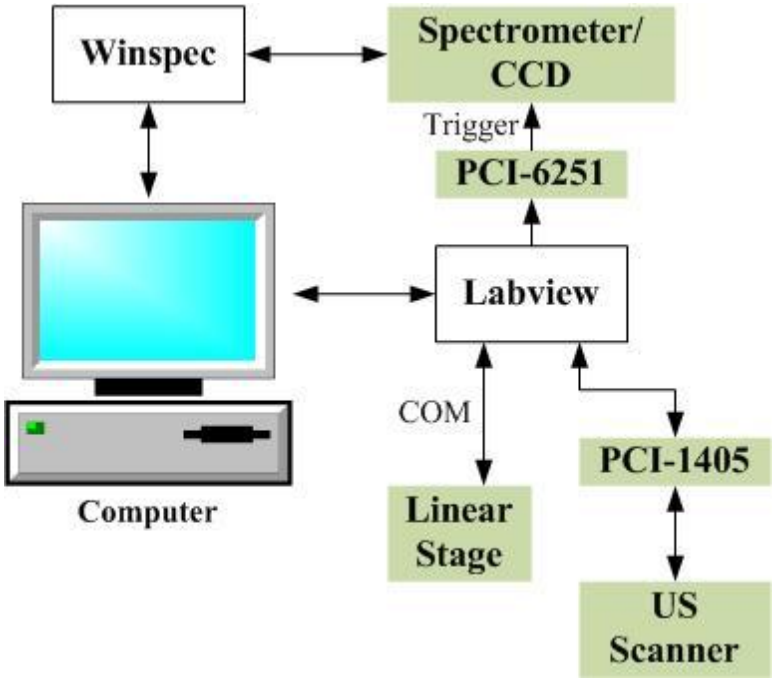

Figure 16 Design of control system

Each position of the motor-stage staying for coupling the light into each source channel was calibrated with maximum coupled light power and was saved in a text file. In Fig. 17, the Labview program firstly loaded the text file including those 7 positions that the linear stage was going to switch then started to move. When the stage arrived at a

position, it gave a response to Labview of this arrival that triggered the data acquisition (DAQ) function to generate the TTL signal to start the CCD data acquisition process which was controlled by Winspec with a pre-defined exposure time. After the CCD got one frame image of data, Labview instructed the linear stage to move to next the position. Those commands were iteratively processed for 7 times.

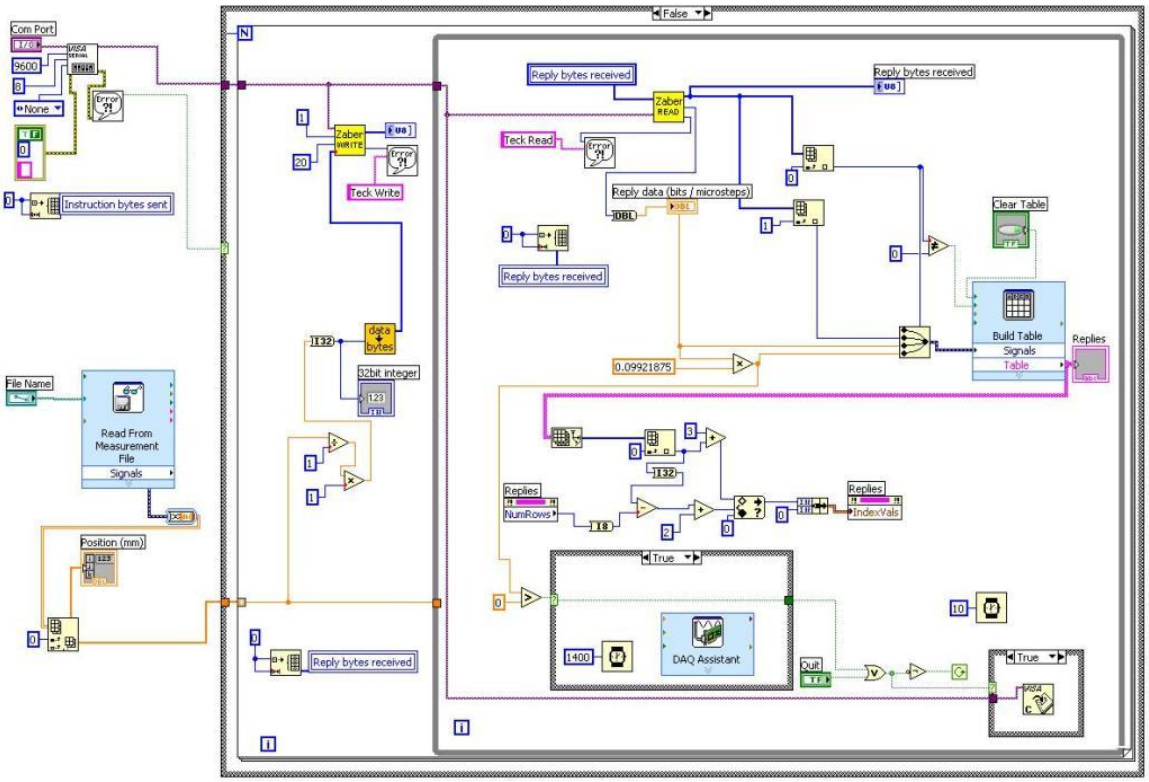

Figure 17 Labview program of system control

The operating interface of the Labview is shown as the following Fig. 18. Each response of the stopping position was visualized in the program during the operation:

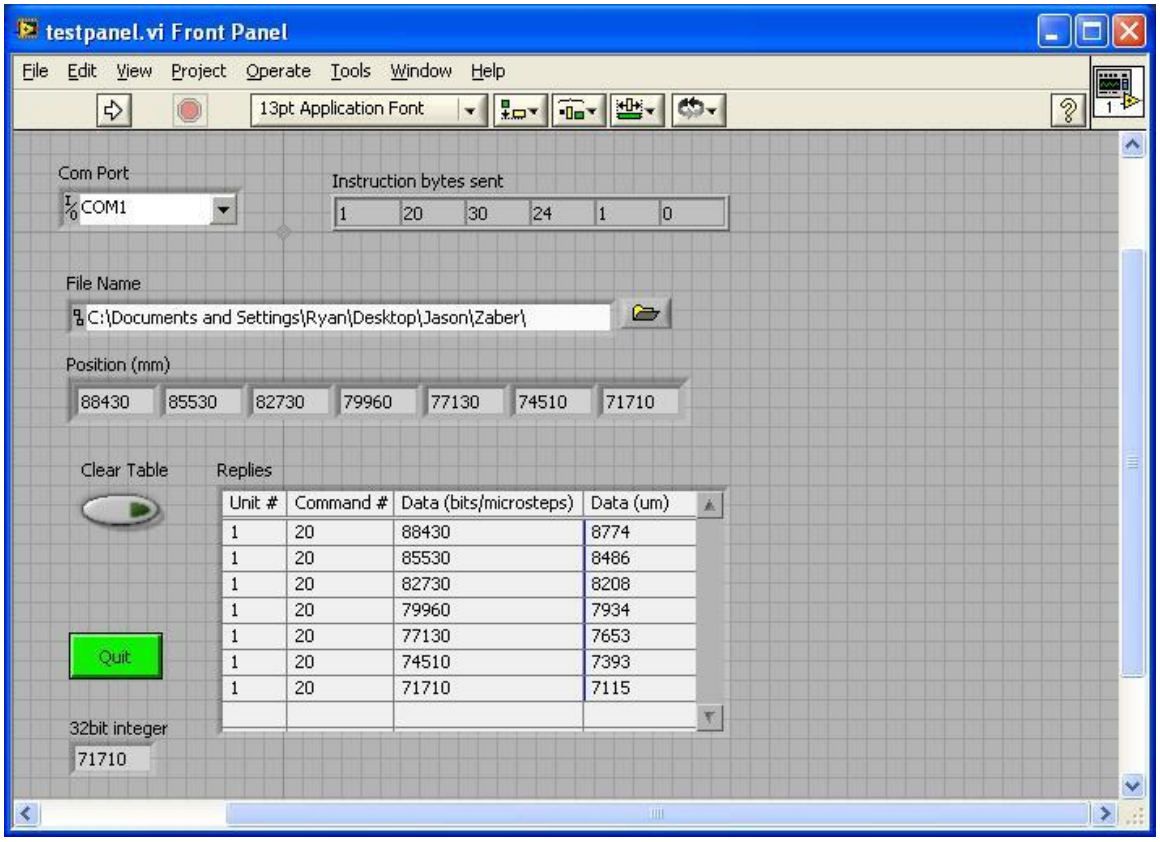

Figure 18 Labview program operation interface of the NIR optical imaging system

CHAPTER IV

SYSTEM PERFORMANCE

The combined US/NIR probe and system enables concurrent acquisition of trans-rectal NIR tomography and TRUS images on the same sagittal plane. The system was first calibrated by known value phantom experiments and further demonstrated by tissue sample tests. Previous studies also have validated that incorporating TRUS *a priori* information allows trans-rectal NIR tomography to recover an absorption target accurately. In this chapter, it was first demonstrated that trans-rectal NIR imaging could recover an absorptive target without spatial *prior*. When incorporating the *a priori* information, the system performance was quantified with accurate reconstruction of target absorption. In tests, 2-dimensional TRUS image was used to locate a suspected TVT target, and NIR optical tomography allowed 3-dimensional imaging. The geometrical relation of the 2D ultrasound image and 3D optical image was shown in Fig. 19. The ultrasound imaging plane was right at the middle-sagittal plane of the 3D optical imaging volume. Most of the later optical images were taken at this plane for the comparison with US images [95]~[98].

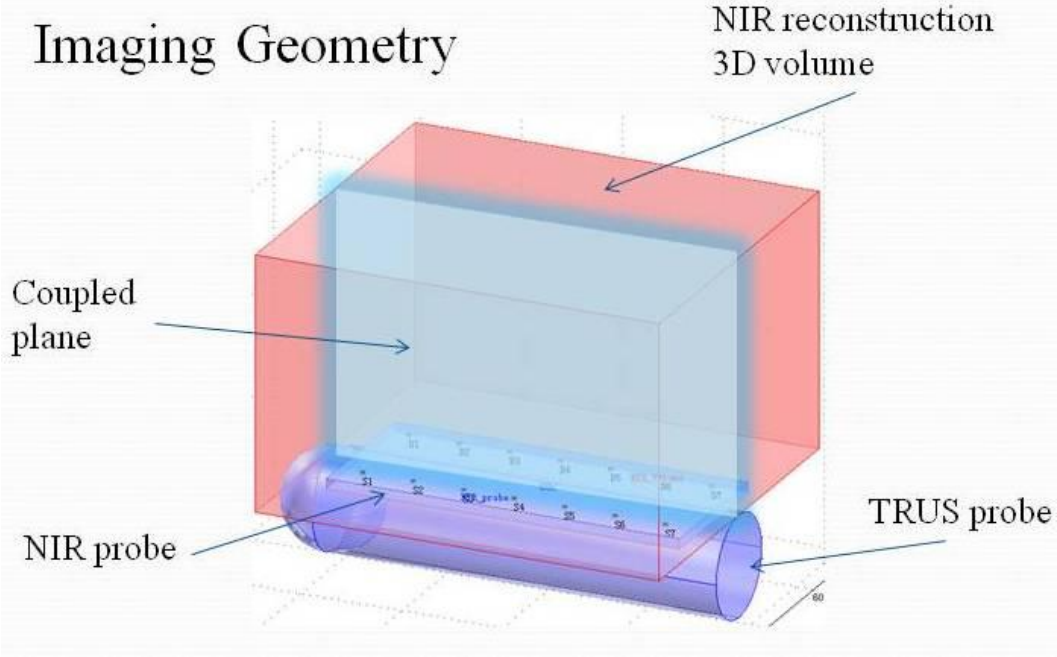

Figure 19 Imaging geometry of the 3D optical reconstruction and 2D US image

In the system performance testing, the calibration will be a first step which is a very important procedure to caliper the system response from steady-state continuous wave (CW) measurement to minimize the effects from the variation of optical source power, background noise of CCD detection, the coupling difference among those optical channels such as the characteristics of each optical fiber, grin lens and prism. In this combined system calibration, the performance of known value solid phantom imaging by the endo-rectal NIR applicator was evaluated in order to quantify the system response. The solid phantom was fabricated from a bulk material that was provided and calibrated by the NIR optical imaging laboratory of Dartmouth College. The phantom (Fig. 20a) was machined to a cylinder-shape with 15mm in diameter and 25mm in length. It has a measured absorption coefficient of 0.0056mm^{-1} and a reduced scattering coefficient of 1.03mm^{-1}. The target was put into a tank which was filled with 1% intralipid with an

estimated optical absorption of 0.0023mm^{-1} and 1.0mm^{-1} of reduced optical scattering. The testing set up was depicted in Fig. 20(b). The target was mounted on the 3-axis freedom stage which can be displaced in 3 dimensions with respect to the fixed trans-rectal NIR optical imaging probe.

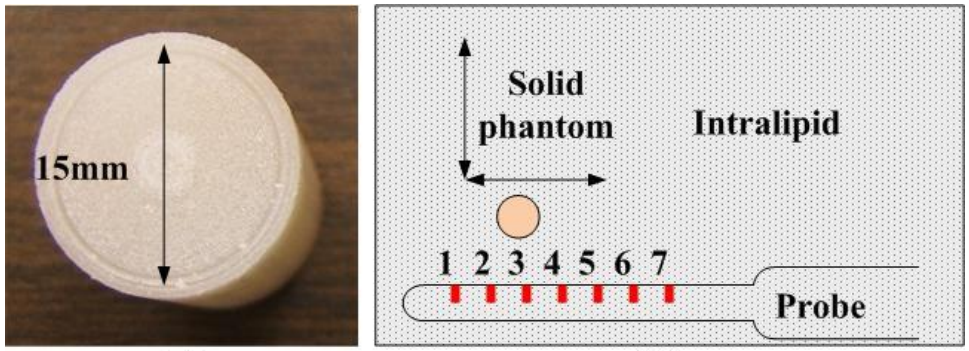

Figure 20 Solid phantom and experimental set up

From the description in section 2.4, the initial guess was very important for the imaging reconstruction. Accurate background absorption was expected in the system calibration for the performance quantification. Several test results of the homogeneous intralipid background with different absorptions added by diluted ink were measured by spectrophotometer as shown in Appendices 1. The following background absorptions were obtained from those results.

4.1 Semi-infinite boundary condition

In the known value phantom system calibration, the spectral-encoded optical system gave a raw data acquired by CCD of the spectrum-encoded optical imaging system shown in Fig. 21(a). If the SLD spectral components were coupled orderly to the source channels from 1 to 7, the higher intensity signals would have been located along a

diagonal line in the CCD acquired image. As previous discussed in Section 3.2, the source coupling sequence from the short wavelength to long wavelength is source 4, 3, 2, 1, 7, 6, 5. Each row represents the detected 7 signals of one detection channels along 7 different wavelengths, and each column indicates how much power of each source channel coupled to 7 detector channels. The modified source coupling configuration described in Fig. 13 leads to the pattern of diagonal-shifted high-intensity signals as shown in Fig. 21(a) which was taken from a homogenous 1% intralipid background with 0.0023mm^{-1} absorption and 1.0mm^{-1} reduced scattering [99].

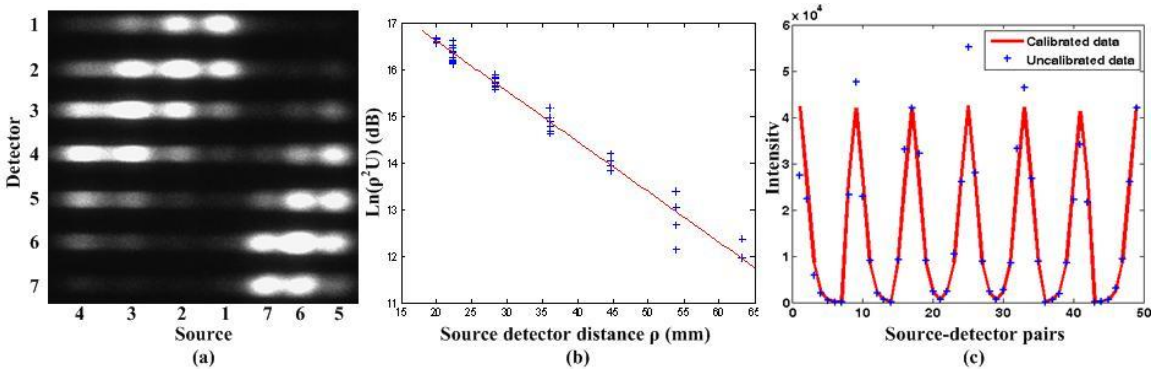

Figure 21 Spectral-encoded system data calibration

Our imaging probe is a slab shape that was put with a cylinder shape trans-rectal ultrasound probe. Recent study on the convex geometry gave an analytical solution of the photon density which can be simplified at large radial dimension and longer source-detector distance (>20mm). The simulation results showed that it can be approximately to the semi-infinite boundary condition. For a collimated source and a detector at a semi-infinite boundary, the diffuse reflectance may be described by:

$$U(\rho)=\frac{S}{4\pi D\rho^2}\left[-4\left(\mu_a/D\right)^{1/2}\left(z_b^2+z_b/\mu_s^{'}\right)\right]\cdot\exp\left[-\left(\mu_a/D\right)^{1/2}\rho\right] \qquad \text{Equation 39}$$

where ρ is the source-detector distance, and z_b is a length term determined by the refractive index mismatch on the boundary. The linear relationship between $\ln\left[\rho^2U(\rho)\right]$ and ρ can be derived from Equ. 39 [100]~[102]:

$$\ln\left|\rho^2U(\rho)\right|=-\sqrt{\frac{\mu_a}{D}}\rho+\ln\left|\frac{S}{4\pi D}\right|+\ln\left|-4\sqrt{\frac{\mu_a}{D}}\left(z_b^2+\frac{z_b}{\mu_s'}\right)\right|=A\rho+B \qquad \text{Equation 40}$$

Fig. 21(b) showed one calibrated data set corresponding to the complete 7×7 source-detector pairs is displayed. And in fig. 21(c) gave a comparison between the calibrated data and non-calibrated one. The slope derived in Equ.39 could be defined by the effective attenuation coefficient which is expressed by Equ.36 in previous Section 2.6.

4.2 Stand-alone optical reconstruction

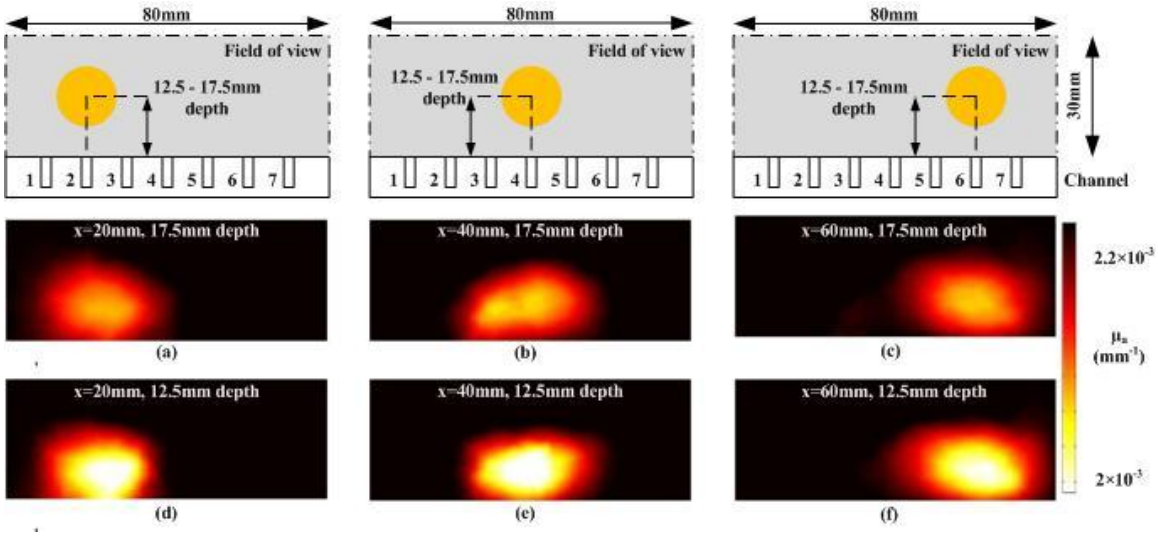

Figure 22 Stand-alone optical reconstruction

Figure 22 lists the images reconstructed with stand alone optical reconstruction method which has been described detail in previous Section 2.4. The FEM based reconstruction used a mesh of homogenous density throughout the entire NIR imaging volume. The optical properties are certainly updated element-by-element in order to recover the heterogeneity being imaged. The solid phantom is placed at the mid-sagittal plane. The NIR images are displayed with a field of view of $80\times30mm^2$. The left most optode is located at 10mm right to the left edge of the image, and the right-most optode is 10mm left to the right edge of the image. The (a), (b), and (c) correspond to the target depth of 17.5mm at longitudinal locations of 20, 40 and 60mm (counted from left edge), respectively. The (d), (e) and (f) correspond to the phantom depth of 12.5mm at longitudinal locations of 20, 40 and 60mm, respectively. The target is identified clearly against satisfactorily recovered background; however, the absorption contrast of the target is significantly underestimated [98]~[103].

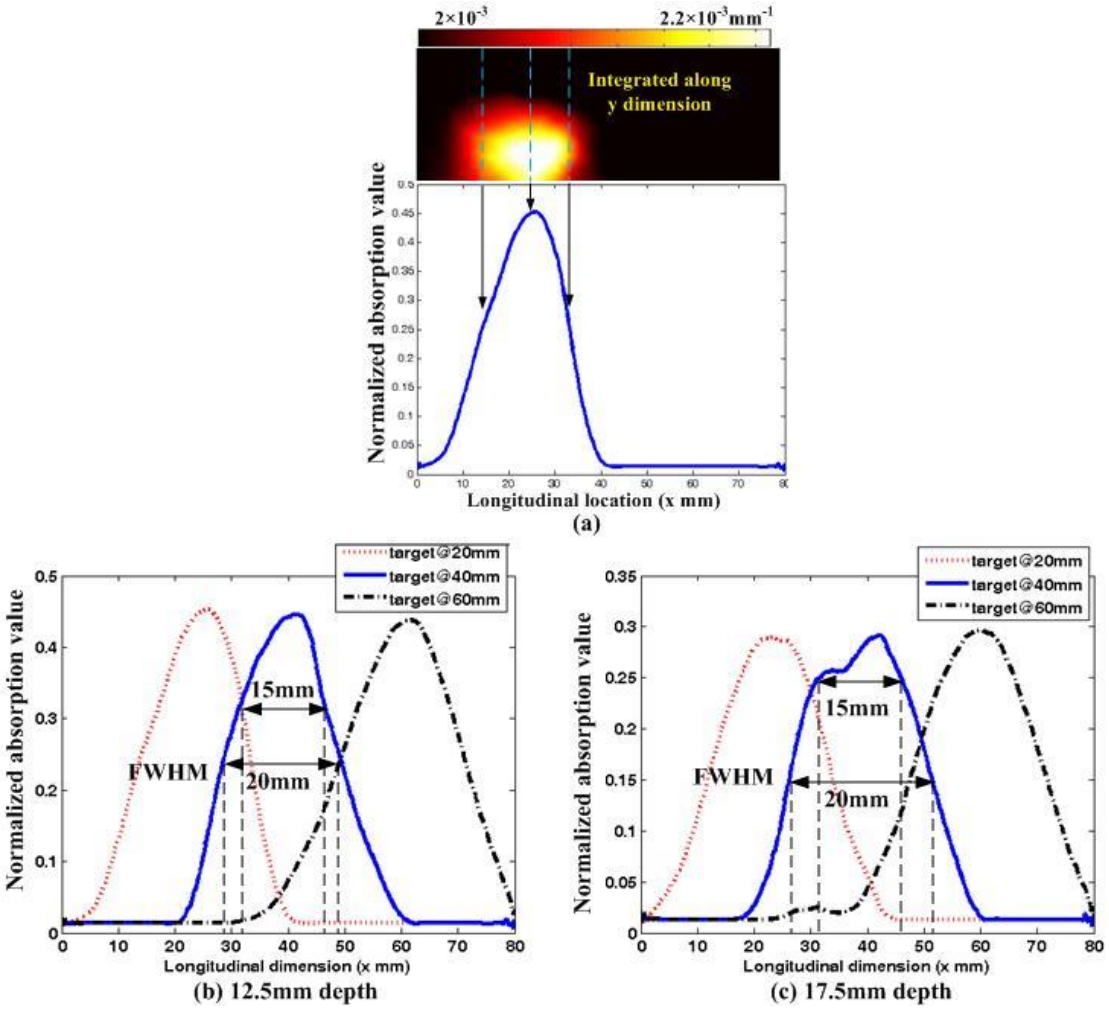

Figure 23 Normalized reconstructed absorption value vs. different longitudinal positions.

Figure 23(a) describes the contours of the normalized reconstructed absorption value. Fig. (b) and (c) depict the normalized absorption contour at three longitudinal locations with different depth accordingly (b) 12.5mm and (c) 17.5mm. At lower depth (b), the contour width is quite narrower than (c) and the peak value is higher than (c) which indicates a more accurate reconstruction in absorption value and size of the suspicious target.

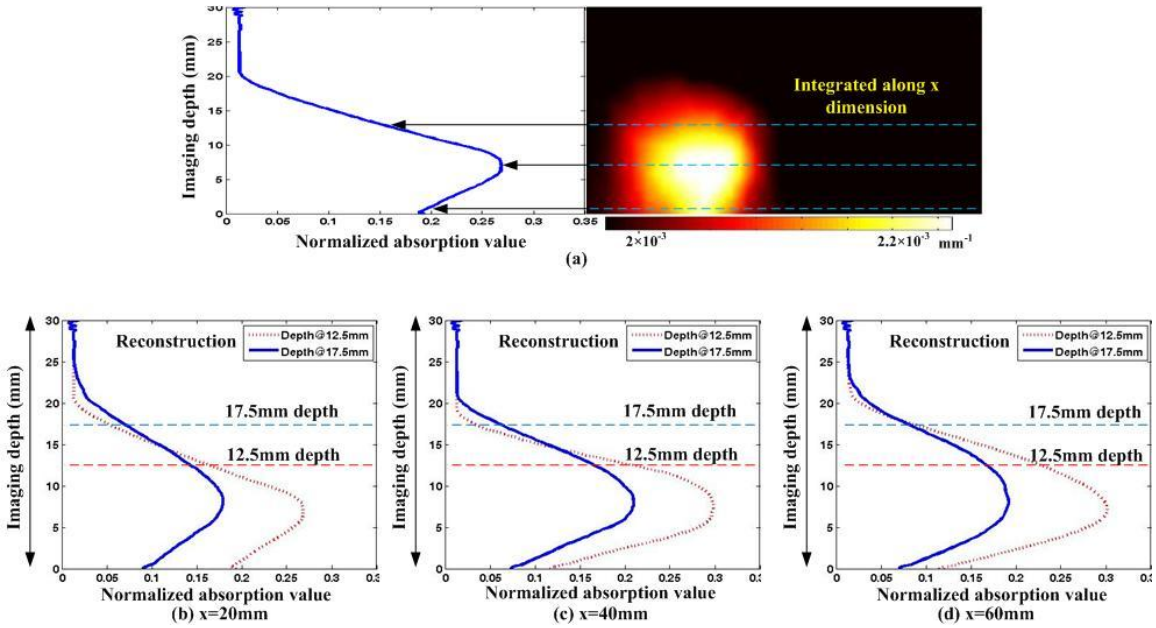

Figure 24 Normalized reconstructed absorption value vs. different target depths

Another contour in one target depth was described in Fig. 24(a). The horizontal axis is the normalized absorption value and the vertical axis is the depth in millimeter unit. (b), (c) and (d) are corresponding to the three longitudinal displacements (x=20, 40 and 60mm) in Fig. 23. It shows only a little differences of the peak when the target was moved from 12.5mm to 17.5mm. The deeper target seems to be reconstructed at the same longitudinal location but with lower recovered absorption value at lower imaging depth.

Figure 25 gives a simulation results at the coronal plane and axial plane when the solid phantom was displaced in the middle-axial plane. In simulation the target was a spherical shape with 10mm in diameter. In the reconstructed optical images, the dash circled area corresponds to positions of the target in coronal or axial plane. The displacement of the target can be fairly recognized in a small range.

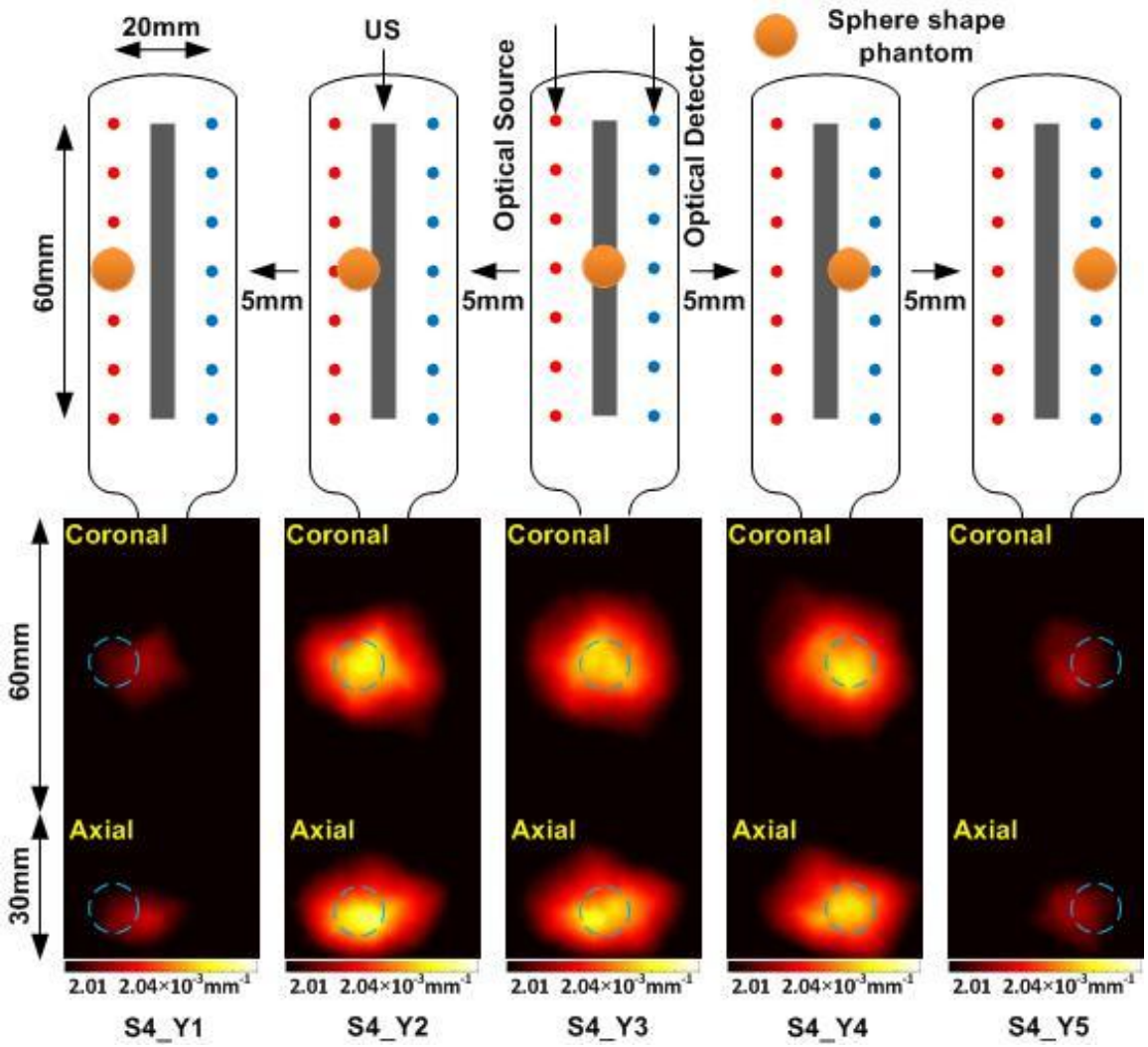

Figure 25 Simulation results when target was displaced in the middle-axial plane

Because of the difficulty of the fabrication of a spherical target, in the experiments, it was replaced by a cylinder shape with 10mm in diameter but 20mm in length. Also, the dashed area in the reconstructed axial and coronal plane is the location of the target. The changes of different target locations can only be recognized in about 10mm range.

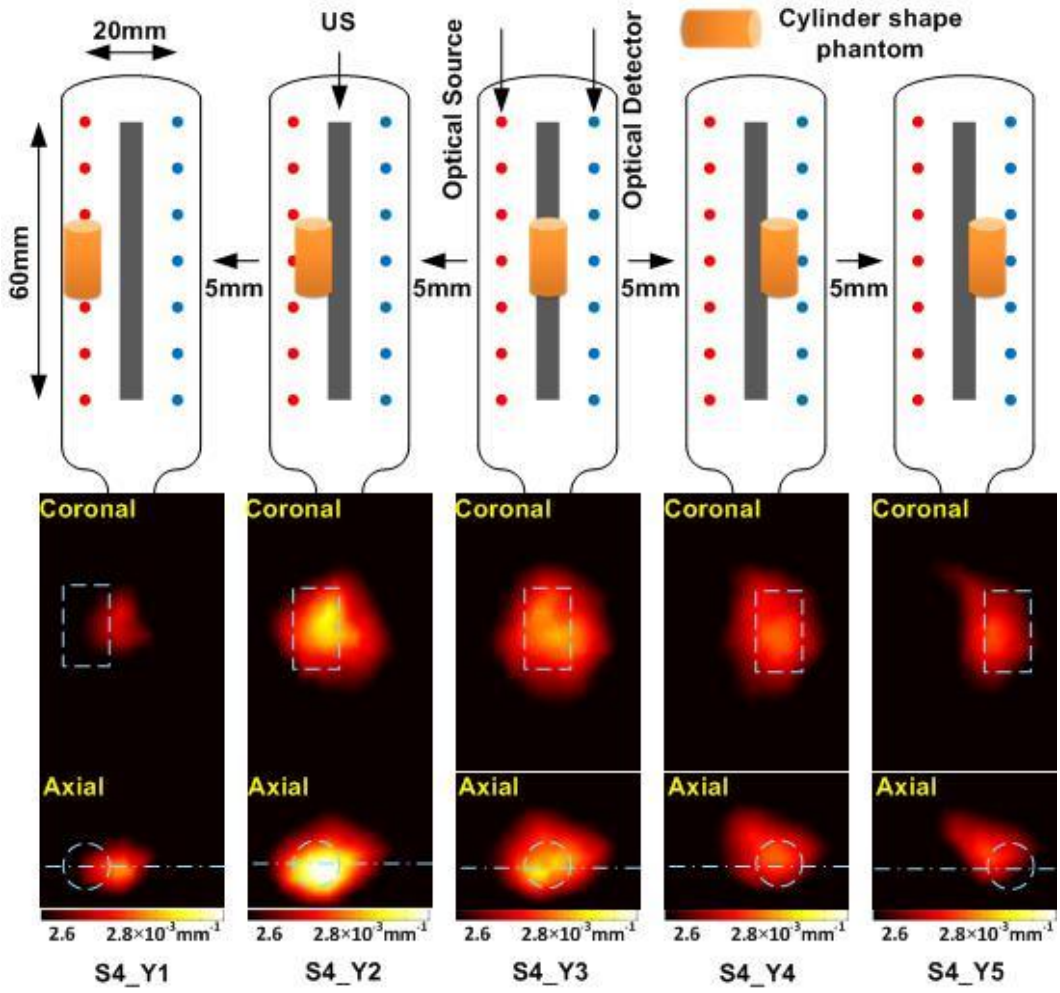

Figure 26 Measurement of the displacement of the target in middle-axial plane

Comparing those simulation and testing results from Fig. 22~ Fig. 26, the system response when a target moved in the sagittal plane was much sensitive than it moved in the axial and coronal plane. This sensitivity problem comes from the inherit reconstruction algorithm discussed in Section 2.4 and also an effect of the probe geometry. The sensitivity issue discussed in previous study is described in Fig. 27.

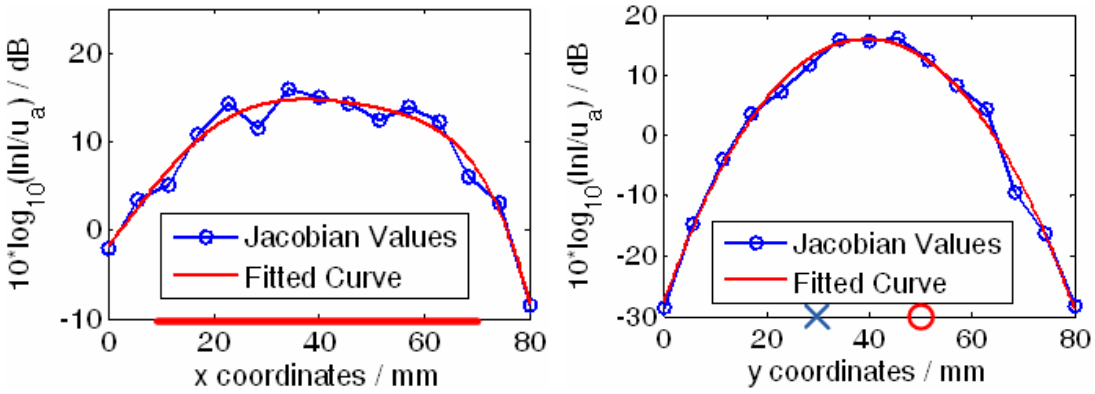

(a) Longitudinal sensitivity (b) Lateral sensitivity

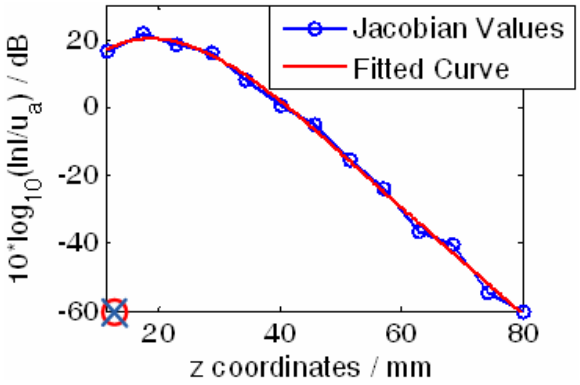

(c) Depth sensitivity

Figure 27 Sensitivity profile of 7 by 7 source-detector optical channel deployment

Figure 27 gave a sensitivity profile calculated by projecting the Jacobian values along a line in the imaging volume with optical properties of μ_a=0.01mm^{-1} and μ'_s=1.0mm^{-1}. The probe occupies a length of 60mm from 10mm to 70mm in (a). In the center part of the probe from 20mm to 60mm corresponds to the source/detector 2 to source/detector 6. The variation of the sensitivity is about 5dB, while in lateral and the depth sensitivity, the displacement of 20mm gives a 20dB changes. This sensitivity analysis explains why in the sagittal plane, the position correlation of reconstructed optical image was overall better than that in the axial and coronal plane [66].

4.3 Imaging reconstruction with *a priori* information

In NIR breast cancer imaging studies, it is found that by incorporating *a priori* information, the optical imaging will be improved both in high imaging resolution and accurate reconstructed optical coefficients. By extending this method to this trans-rectal prostate NIR imaging study, imaging reconstruction with *prior* is described in Fig. 28. The location and the size information of the target obtained from US image were used to generate a dual-density mesh with two regions of background and suspicious area. Both the optical properties of absorption and scattering are set to be homogenous in those two regions (background and ROI). In this case, the Jacobian matrix in CW (Equ. 35) imaging reconstruction will be simpler.

$$J = \begin{vmatrix} \frac{\delta \ln I_1}{\delta D_1} & \frac{\delta \ln I_1}{\delta D_2} & \frac{\delta \ln I_1}{\delta \mu_{a1}} & \frac{\delta \ln I_1}{\delta \mu_{a2}} \\ \frac{\delta \ln I_2}{\delta D_1} & \frac{\delta \ln I_2}{\delta D_1} & \frac{\delta \ln I_2}{\delta \mu_{a1}} & \frac{\delta \ln I_2}{\delta \mu_{a2}} \\ \vdots & \vdots & \vdots & \vdots \\ \frac{\delta \ln I_M}{\delta D_1} & \frac{\delta \ln I_M}{\delta D_2} & \frac{\delta \ln I_M}{\delta \mu_{a1}} & \frac{\delta \ln I_M}{\delta \mu_{a2}} \end{vmatrix} \qquad \text{Equation 41}$$

Where the notation 1 and 2 indicate the region of the homogeneous background and interested. In the iteration, there are only 2 sets of different optical properties updated in each round. The dramatic decreased variables make the reconstruction value become more accurate and faster [56].

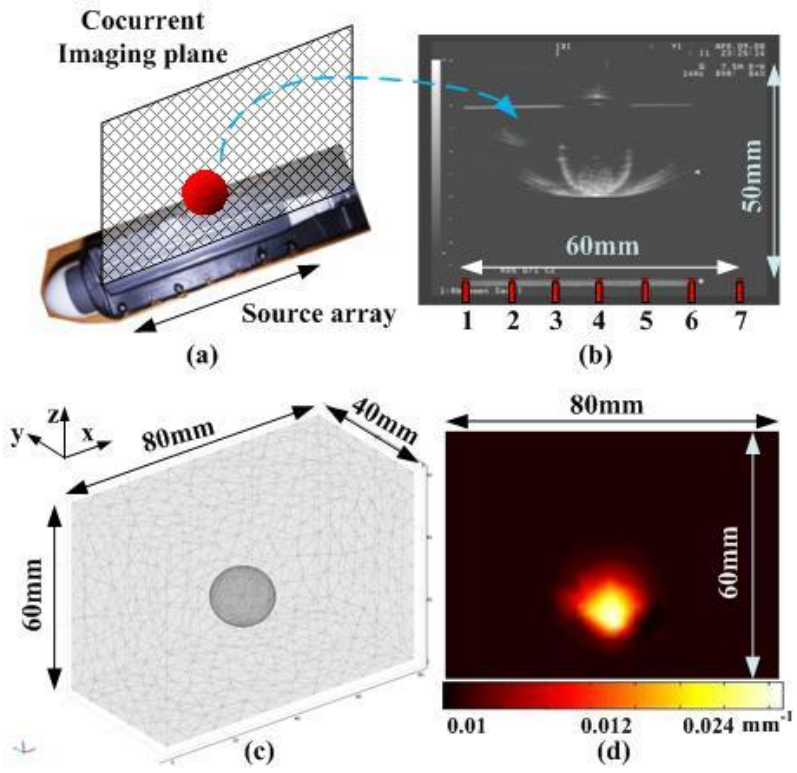

Figure 28 Reconstruction with spatial *a priori* information

In Fig. 28 simulation, the NIR image reconstruction uses a 3-dimensional mesh representing $80\times40\times60mm^3$. The NIR image is reconstructed and displayed at the mid-sagittal plane to correlate with TRUS image. The absorption coefficient is correctly recovered with this *a priori* information. The image reconstruction typically takes ~10 minutes on a 3.0GHz Pentium(R) 4 PC for 10 iterations.

The same data sets in Fig. 22 were reconstructed in Fig. 29 using the target *a priori* information obtained from TRUS. The TRUS image, similar to the one in Fig. 28(b), has artifacts around and shows only the lower half of the cylinder owing to the shadow effect. This image/artifact pattern is specific to the solid cylinder target that reflects much of the US signal on its surface. This type of artifact may not be

representative for tissue imaging in situ. The artifact is thereby ignored when incorporating the spatial information of the target, by generating a mesh having a homogenous background region and a circular target region as shown in Fig. 28(c). As there are only two regions to reconstruct, the hierarchical iteration routine involves only 2-steps. The reconstructed values are given in Table 6. The absorption coefficient of the background medium is reconstructed at 0.002mm^{-1} for all images and the target is recovered to within 14% of the true value [91].

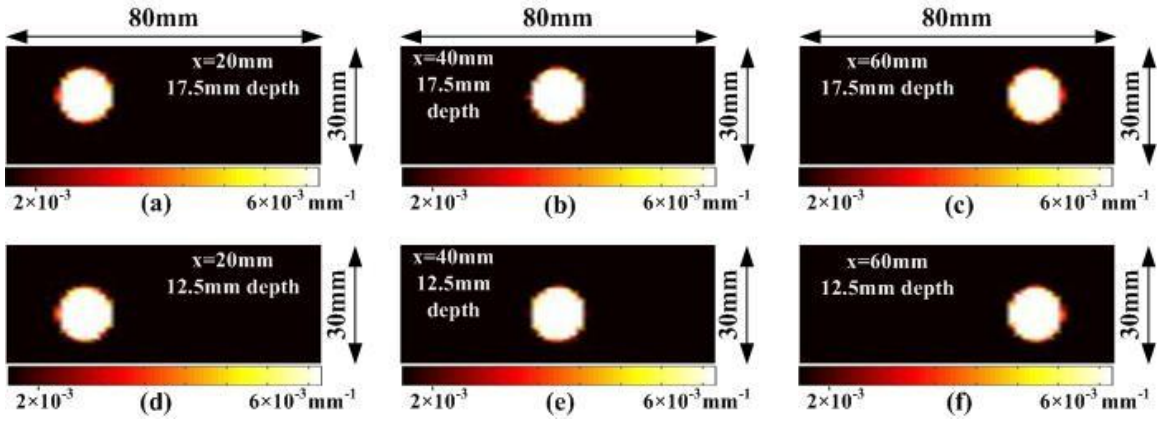

Figure 29 *prior*-guided reconstruction of solid phantom

Table 6. NIR image reconstruction guided by TRUS spatial *prior*

Center depth	12.5mm		
Longitudinal location (x)	20mm	40mm	60mm
True Value (mm^{-1})	0.0056	0.0056	0.0056
Reconstructed value (mm^{-1})	0.0067	0.0064	0.0063
Center depth	17.5mm		
Longitudinal location (x)	20mm	20mm	20mm
True Value (mm^{-1})	0.0056	0.0056	0.0056
Reconstructed value (mm^{-1})	0.0064	0.0063	0.0061

4.4 Imaging of dual targets

The capability of recovering more than one target by the endo-rectal NIR probe was also examined. Two cylinder-shaped solid tissue phantoms, including the one shown in Fig. 20, were used as the target. Both targets were 15mm in diameter and 25mm in length. The newly added solid phantom has an absorption coefficient of $0.0064mm^{-1}$ and a reduced scattering coefficient of 0.91 mm^{-1} in comparison to the other one of $0.0056mm^{-1}$ and $1.03mm^{-1}$. Fig. 30(a) and (b) are the images for placing the two targets at depths of 17.5mm and 22.5mm, respectively, in the mid-sagittal plane, with 20mm longitudinal spacing. When the reconstruction is performed without the target spatial information, the two targets can barely be differentiated at the depth of 17.5mm by the normalized contour same calculated as section 4.2, and not discriminated at the depth of 22.5mm. The absorption contrasts of the targets are also significantly underestimated and

overlapped in both cases. Fig. 30(c) indicates the results of using the spatial information from the TRUS image. The two targets can be recovered as having different absorption contrasts at both depths. The reconstructed absorption coefficients listed in Table 7 are also close to the true values.

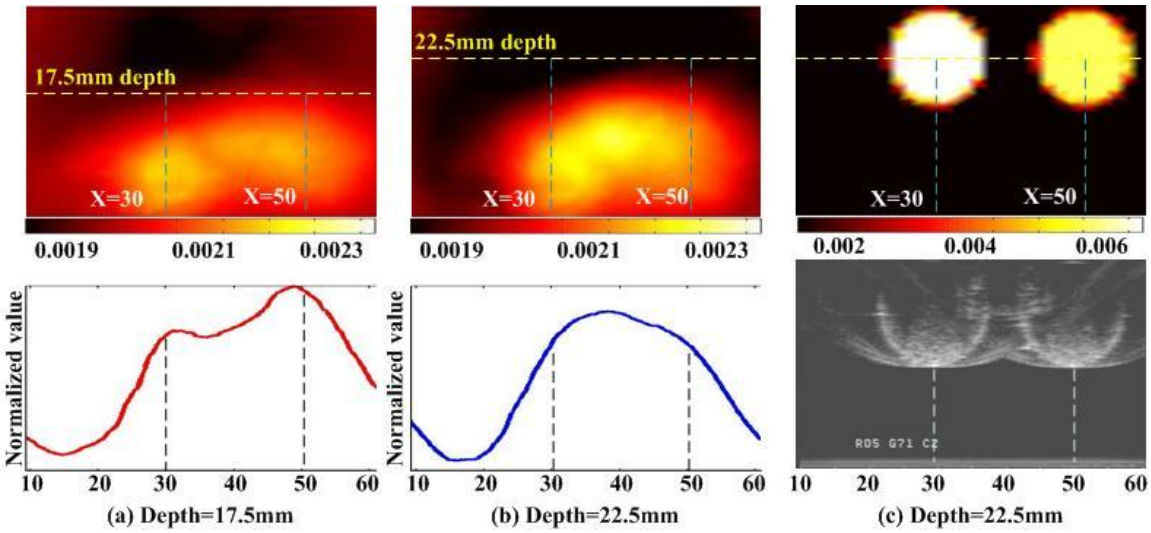

Figure 30 Imaging of dual targets using solid phantoms

Table 7 Reconstructed absorption coefficients with spatial *prior*

Target optical absorption	Target 1	Target 2
True value (mm^{-1})	0.0064	0.0056
Reconstructed value (mm^{-1})	0.0067	0.0058

4.5 Effect of condom

The TRUS probe is always covered with a regular latex condom when imaging the prostate. Therefore the TRUS-coupled NIR applicator has to be applied with a condom if used in the clinic. In the previous applications of NIR tomography imaging

there was no need of applying a latex barrier between an NIR applicator and the tissue being interrogated, therefore the effect of a latex condom on NIR tomography was not reported which was firstly reported in this study.

The test being carried out used the setup and solid phantom shown in Fig. 31, by applying US gel to the NIR/US probe, covering the NIR/US with a condom, and then pressing the condom to eliminate any gas between the condom and the probe. US gel is not applied on top of the condom when imaging the intralipid, but is applied for all the tissue imaging tests presented in Section 4.6~4.9. The absorption coefficient of the target reconstructed using TRUS information is listed in Table 8. The overall distribution of the reconstructed absorption coefficient of the target is plotted in Fig. 31(b), and the distribution specific to target position is plotted in Fig. 31(c). These results, which are consistent with those presented in Table 6, demonstrate that the condom has minimum effects on NIR imaging. Nevertheless, an attenuation of the light power is observed, as it takes 10% longer exposure time for CCD to integrate the same amount of signal when the condom is applied.

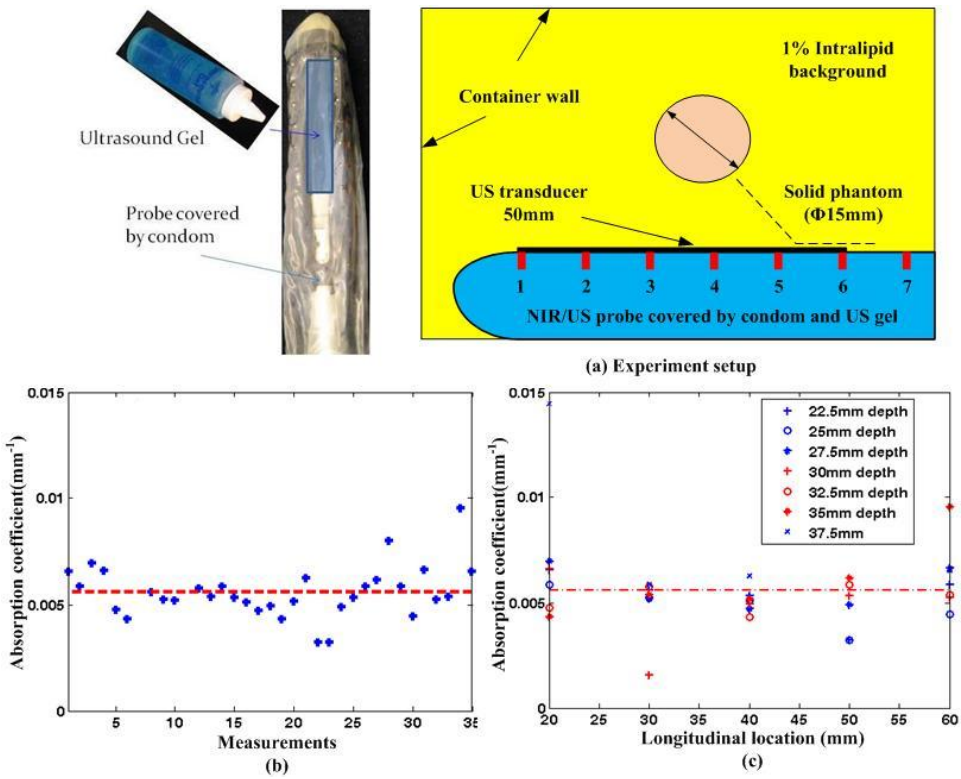

Figure 31 Condom effect measured from solid phantom

Table 8 Absorption coefficient reconstructed with the use of condom (mm^{-1})

Depth (mm)	22.5	25	27.5	30	32.5	35	37.5
True value	0.0056	0.0056	0.0056	0.0056	0.0056	0.0056	0.0056
X=20mm	0.0065	0.0058	0.0070	0.0066	0.0048	0.0043	0.014
X=40mm	0.0053	0.0051	0.0047	0.0049	0.0043	0.0052	0.0063
X=60mm	0.0059	0.0045	0.0066	0.0052	0.0054	0.0095	0.0065

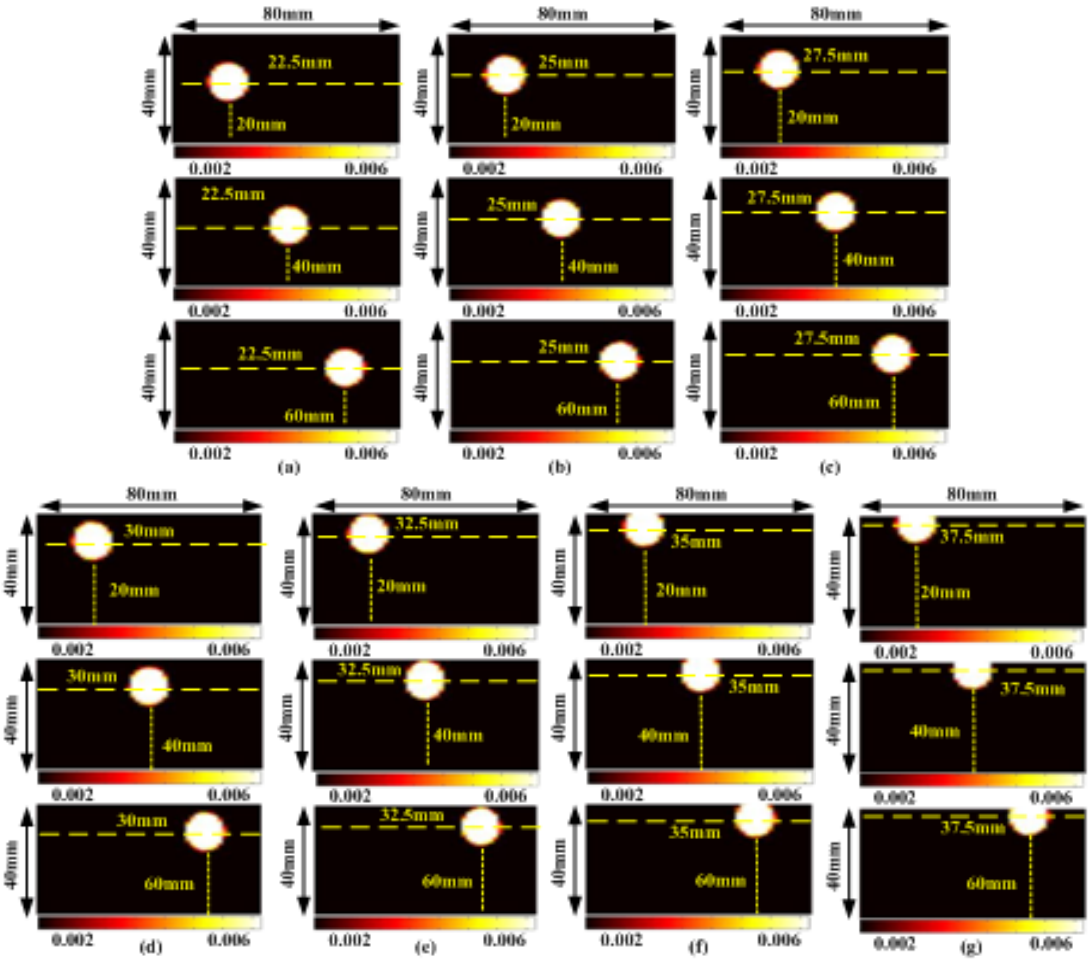

Figure 32 *a priori* reconstruction images of condom tests

The reconstructed images corresponding to Table 8 are listed in Fig. 32. The tests in Fig. 32 represent the most favorable conditions in which there is only one target in an otherwise homogenous medium. For the given condition in Fig. 32 the target can actually be recovered at depth up to 40mm when it is located at the longitudinal center of the probe. This is not unexpected as the maximum longitudinal sensitivity occurs at the center of the probe, and the lower edge of the tissue phantom is actually 32.5 from the probe surface. When the tissue phantom is moved to either longitudinal side of the probe,

the imaging depth degraded to 30~35mm, which is apparently due to the degraded sensitivity at the probe edges.

4.6 Imaging solid absorbing object embedded in avian tissue

The condom-covered NIR/US probe was enclosed within thick layers of chicken breast tissue $\mu_a = 0.006mm^{-1}$, $\mu_s' = 0.757mm^{-1}$, and a black object (10mm diameter ×10mm length) was embedded as a high absorptive target. The photographs in Fig. 33(a) and (b) show the setup of tissue sample and the absorbing target being embedded. The tissue without the absorbing target is also imaged as a baseline test. The baseline images by US and NIR are shown in Fig. 33(c), where the NIR image is reconstructed using a homogenous mesh as there was no indication of a target on US. Figure 33(d) to (f) correspond to target being embedded at different longitudinal locations at slightly different depths. The embedded object is clearly visible in the US images as anechoic shadows. The NIR imaging without *a priori* information can clearly recover the object, but with inconsistent and potentially much under-estimated absorption coefficients. When the target location and size information are used to guide the NIR image reconstruction, the target is recovered with consistent absorption coefficients indicating a strongly absorbing object [104].

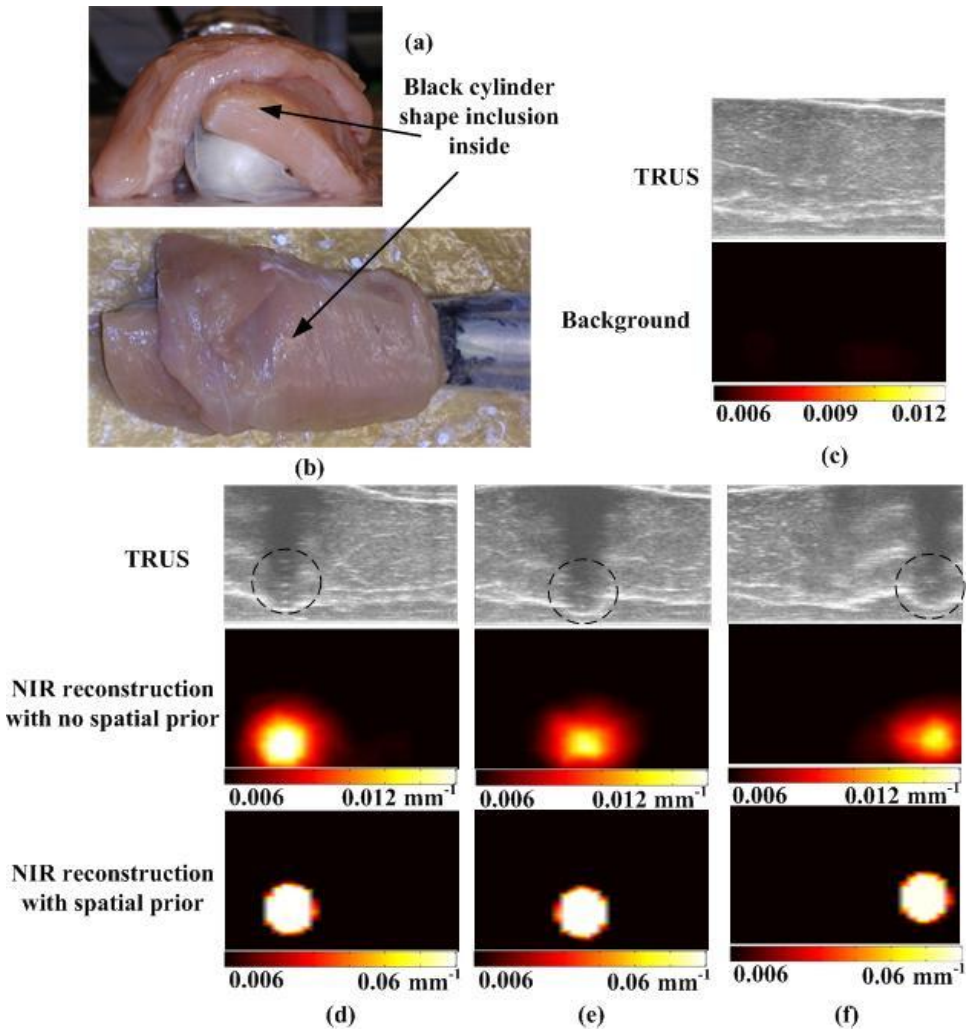

Figure 33 Avian tissue imaging with embedded solid target

(a) front view; (b) top view; (c) no inclusion; (d) inclusion is at 20mm; (e) 35mm; (f) 58mm, longitudinally, respectively.

4.7 Internal imaging of avian tissues

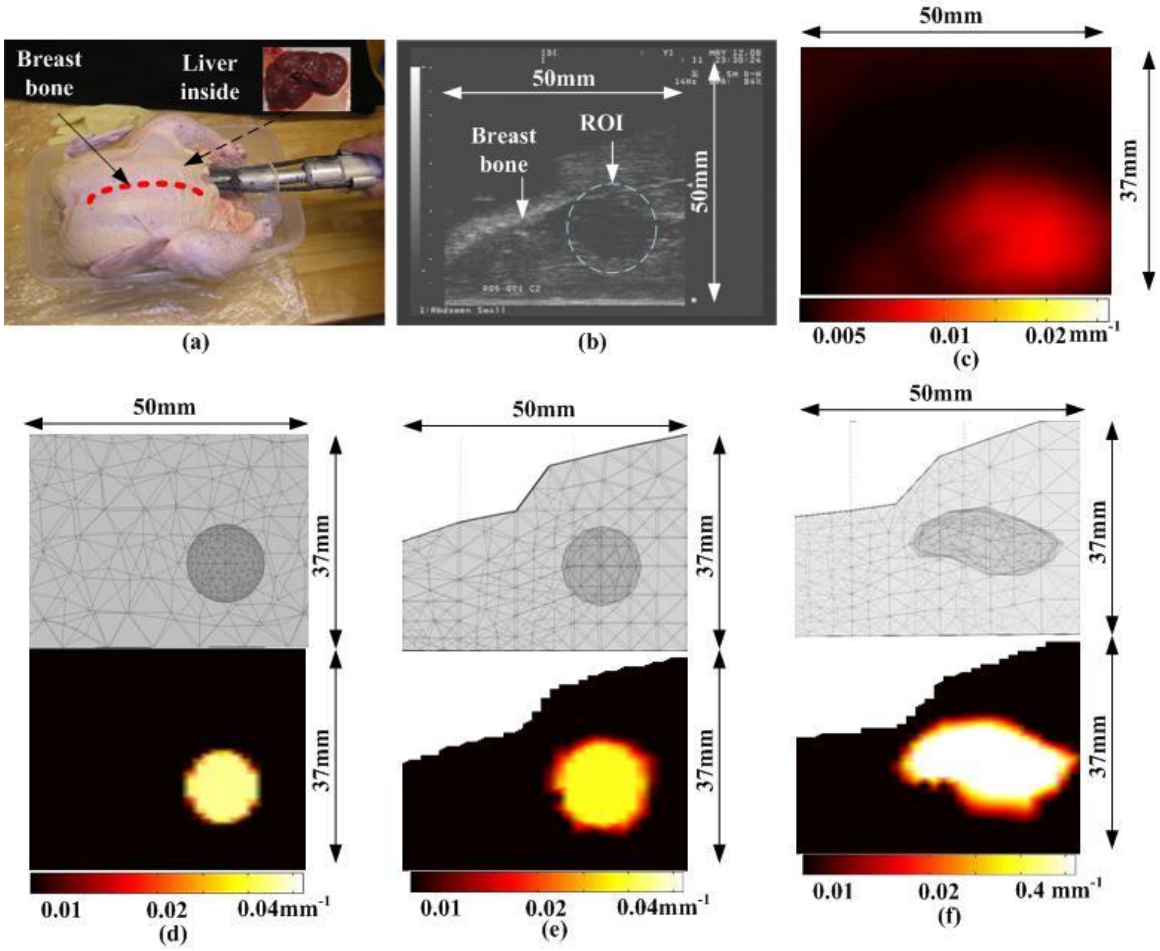

Figure 34 Internal imaging of avian tissue embedded with a piece of liver

As shown in Fig. 34(a) the empty abdomen of a whole chicken was filled with chicken breast tissue and a piece of chicken liver was embedded within the breast tissue. The embedded liver shows up as the hypo-echoic region circled in Fig. 34(b). The NIR image reconstructed without any target information is given in Fig. 34(c), in which the absorptive mass does correlate longitudinally with the liver tissue. Fig. 34(d) shows NIR image reconstructed by treating the liver mass as a sphere. Fig. 34(e) shows the NIR image reconstructed by excluding the non-tissue region from the background of Fig.

34(e). Fig. 34(f) shows the NIR image reconstructed by taking into account the irregular shape of the liver mass. Among the 3 spatial *prior* implementations, the one in Fig. 34(f) is the most accurate wherein the absorption coefficient of the chicken liver mass is also the closest to the realistic value [104].

4.8 TRUS-coupled trans-rectal NIR tomography of canine prostate *in situ*

TRUS-coupled trans-rectal NIR imaging of the prostate is conducted on a canine cadaver. The prostate was exposed and approximately 0.33ml of homogenized foal liver was injected ventral-dorsally, para-median in the left lobe of the prostate. The prostate was then enclosed in thick layers of peri-prostate tissues. On the TRUS image of Fig. 35(a) the injected liver tissue is visible by the mass proximal to the center of the prostate and the vertical hyper-echoic strip at the ventral side of the prostate. The large hypo-echoic region at the upper half was due to air. The mesh generated in Fig. 35(b) has excluded the air based on the US image. The rectum wall was not outlined in the mesh because of its close proximity and near opposition to the US transducer due to the small size of this canine cadaver. The rectum layer may be included when imaging a larger subject. The finalized mesh given in Fig. 35(b) shows nested-domains where there is a relatively small prostate and a much smaller target in the prostate. The NIR image in Fig. 35(c) is reconstructed by applying the 3-step hierarchical reconstruction method introduced in the previous paper. A highly absorptive mass is clearly recovered out of the injected liver tissue. The absorption coefficient of the foal liver tissue in Fig. 35(c) is lower than that of the avian liver tissue in Fig. 35(f); nevertheless both values are at the order of $0.1mm^{-1}$, indicating high absorption by both tissues. The reconstructed absorption coefficients of the prostate and the peripheral tissue are given in Table 9. It is

very interesting to observe that the numbers agree with the values suggested by the literature [104].

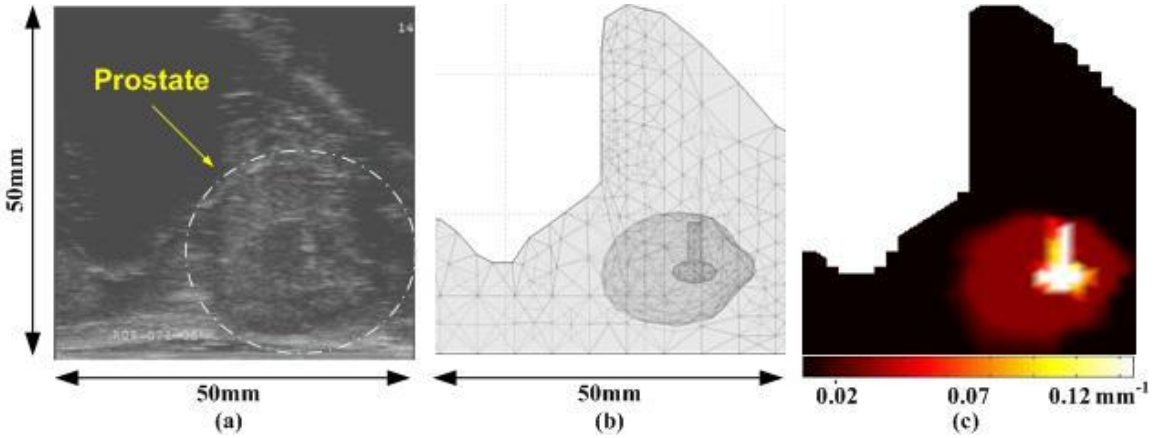

Figure 35 Trans-rectal NIR / US imaging of canine prostate *in situ*

Table 9 Reconstructed absorption value of *ex vivo* canine prostate

Region	Background	Prostate	Injected liver
Reconstructed value (mm^{-1})	0.0062	0.0309	0.1301

4.9 Trans-rectal NIR tomography of target ambiguous to TRUS

In all the tests presented in previous work, the target of interest is visible or at least sensitive to US, therefore US spatial information of the target is readily rendered to guide the NIR image reconstruction. If the target is ambiguous to US, it may still be recognizable by NIR-only reconstruction. One example is given in Fig. 36 wherein a piece of chicken breast tissue was dyed with diluted India ink (Pelikan Schwarz – black) and then placed in the middle of the natural chicken breast tissue. The approximate boundary of the dyed tissue is marked with the dash-circle in the US image. This embedded tissue is hardly distinguishable in the TRUS image; therefore the NIR image

reconstruction was performed without any *a priori* information. The target is identified by NIR even though the depth and size were not accurate. This result may show positive indication on the clinical application of trans-rectal NIR/US measurement providing the fact that up to 40% of prostate tumors are not sensitive to US. Besides using NIR information to characterize US-sensitive lesions, if the NIR imaging is able to discover a lesion that is otherwise non-suspicious on US, the overall sensitivity and specificity of TRUS-based prostate imaging may be improved [66][91]

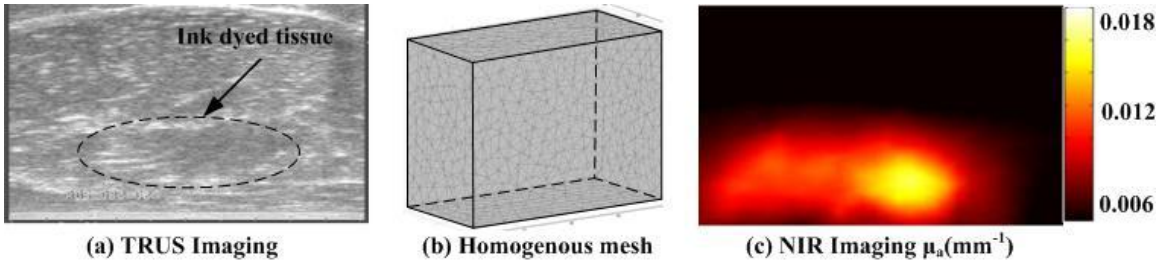

Figure 36 Images of a tissue mass that is ambiguous to TRUS but sensitive to NIR.

CHAPTER V

IN-VIVO OPTICAL IMAGING OF CANINE PROSTATE

Dog has been previously used for prostate tumor model studies because of the morphological and functional similarities between canine and human prostate glands. The studies were conducted in Center for Veterinary Health Sciences at Oklahoma State University under a protocol approved by the university's Institutional Animal Care and Use Committee. It was also inspected on site by DOD. Three dogs have been used for the prostate tumor model study up to the completion of this thesis. The first one is 4 years of age dog, 20 kg sexually intact, adult mixed-breed, but the injected tumor failed to grow in its prostate. The second one is a 12 kg sexually intact adult purpose-bred Beagle dog which successfully grew a transmissible venereal tumor (TVT). This dog was measured by single wavelength optical system at 840nm which gave associated high contrast of optical absorption and optical scattering. The third one is an adult 20-kg, intact male, foxhound estimated to be six years of age. It also had TVT grown in its prostate and was measured by dual-band optical system at 785nm and 830nm that could provide the contrast of total hemoglobin concentration [HbT]. The physical examination and ultrasound revealed normal prostate for these dogs before the injection of the transmissible venereal tumor (TVT) cells.

5.1 Canine prostate imaging geometry

As shown in Fig. 37, the dog was anaesthetized during the experiment. The rectum was cleaned and filled with ultrasound gel. The combined TRUS/NIR probe was covered by condom and inserted through the rectum to imaging the prostate. In the experiment, the probe was handled by experienced veterinarians and those different positions were monitored by the real-time TRUS.

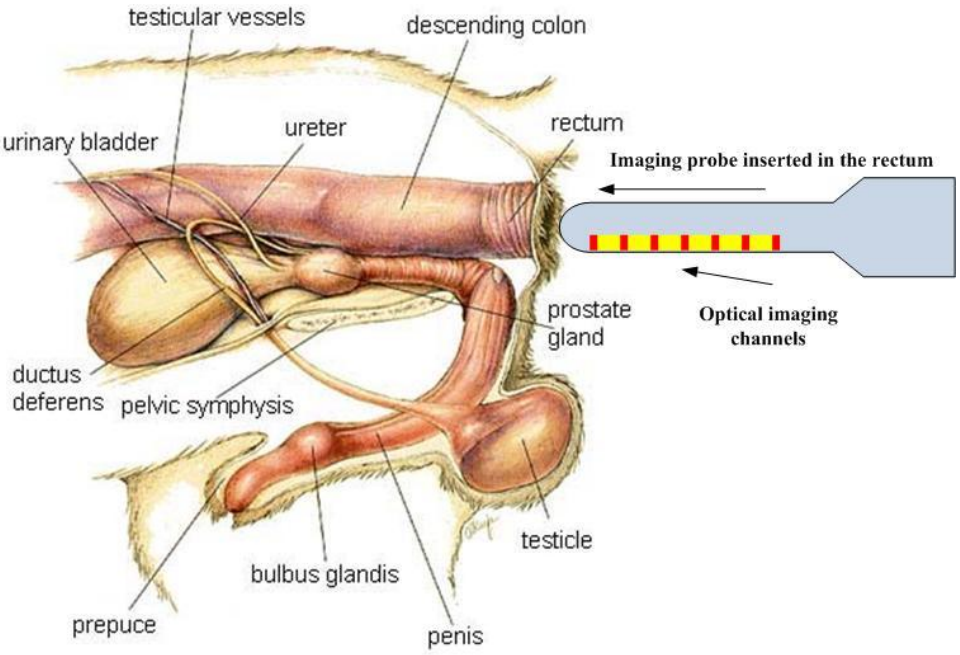

Figure 37 Canine prostate

Figure 38 shows the axial and sagittal ultrasound of the canine prostate. In the clinical axial plane imaging, the left side of the image actually indicates the prostate right lobe, the right side of the image shows the left lobe of prostate as well. The prostate region can be well defined by the capsule line shown in the ultrasound image. In the sagittal plane image, the bladder and pelvic bones can also be used to correlate the

location of the prostate with respect to the probe since the bladder has a clear hypo-echoic region and the pelvic bone has a distinct hyper-echoic region in US images.

Figure 38 TRUS images of prostate at axial and sagittal plane

In each experiment, the probe was put into five different angles with respect to the prostate in order to imaging five different parts of prostate from right lobe edge to left lobe edge as shown in Fig. 39 which were labeled as “Right lobe edge”, “Right lobe middle”, “Middle line”, “Left lobe middle” and “Left lobe edge”.

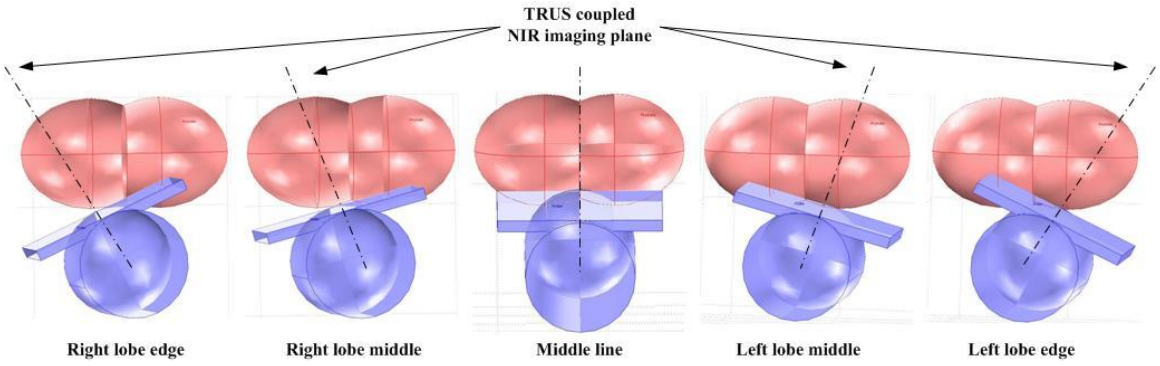

Figure 39 Five sagittal planes for *in-vivo* of canine prostate

At each sagittal imaging plane, the probe was put into three different longitudinal positions from cranial side, middle to the caudal side (Fig. 40).

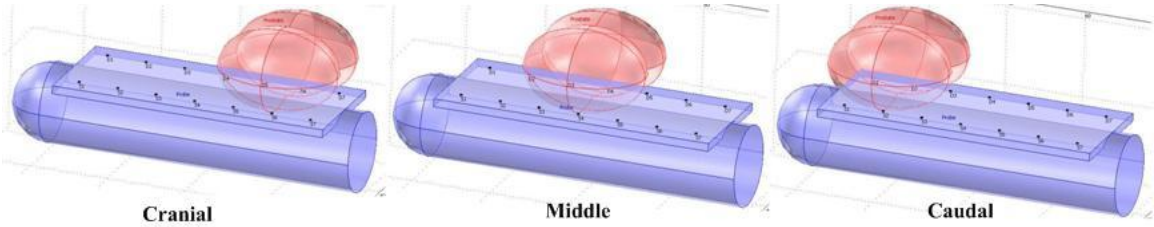

Figure 40 Three longitudinal locations for *in-vivo* imaging of canine prostate

5.2 Canine Transmissible Venereal Tumor (TVT)

The unique canine TVT is a round cell tumor that mainly affects the external genitalia and can be transmitted from animal to animal during copulation, regardless of histocompatibility. TVT cells can be propagated in immunocompromised (SCID) mice and transferred to different tissues of the dog to result in a neoplastic mass effect useful for imaging studies (Fig. 41) [105].

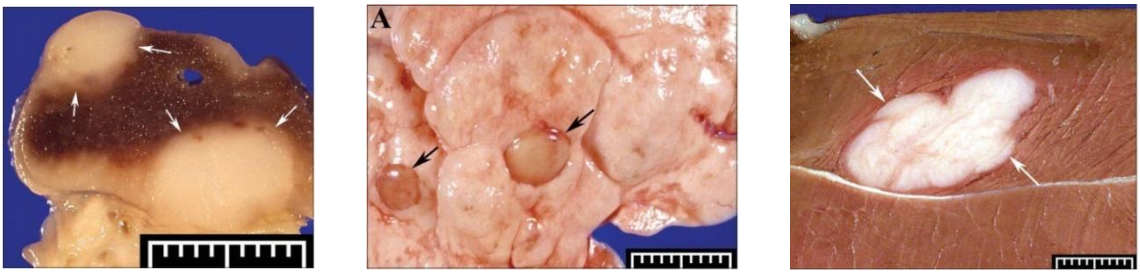

(a) Liver (b) Lung (c) Muscle

Figure 41 cTVT grown on different tissue of canine

As shown in Fig. 42, compared with the normal prostate tissue, the TVT tumor has a distinct boundary from its higher cell density, and the TVT cells has fewer chromosomes than normal cells. The photomicrography of TVT cells also showed that it has a large hyperchromatic nucleus and single conspicuous nucleolus which could introduce a higher optical absorption and scattering.

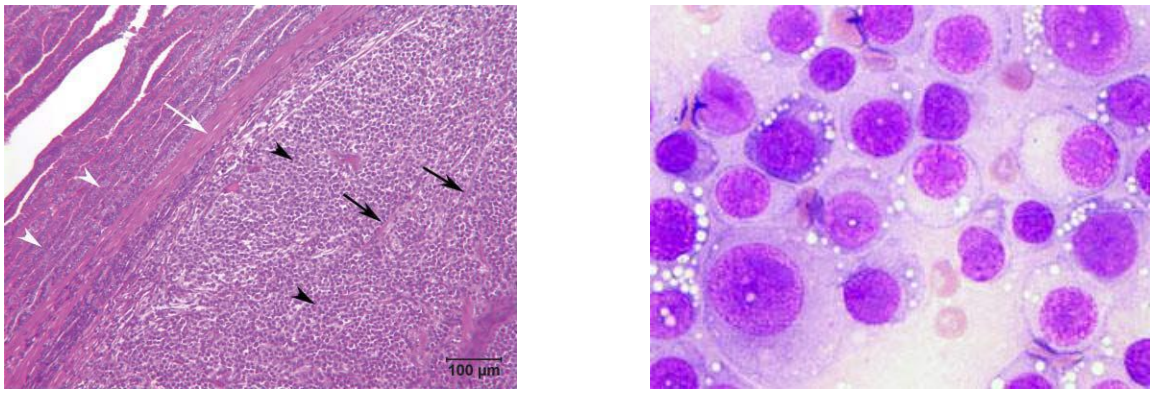

Figure 42 Photomicrography of cTVT in prostate

In this project, the TVT cell line was obtained cryopreserved from MD Anderson Cancer Center (Houston, TX). Following two cycles of inoculation into the subcutis of non-obese-diabetic/severe-combined-immunodeficiency (NOD/SCID) mice, neoplastic cells were recovered and homogenized for injection into the canine prostate gland. Fig. 43 showed a TRUS monitored injection. Approximately 3 cc of TVT cells were aseptically injected transperineally into the right lobe of the prostate using a 6-inch 16 gauge hypodermic needle under TRUS visualization.

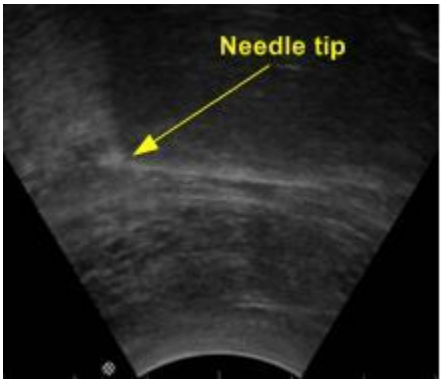

Figure 43 TRUS monitored the TVT injection

5.3 Imaging of normal canine prostate

Figure 44 gives three sets of sagittal TRUS/NIR imaging of the normal canine prostate at right lobe, middle-line and left lobe. The dimension of NIR image is the same as the TRUS with 50mm (cranial to caudal) × 30mm (dorsal to ventral). In each column, the absorption, scattering and effective attenuation coefficients are reconstructed from one measurement data set [106].

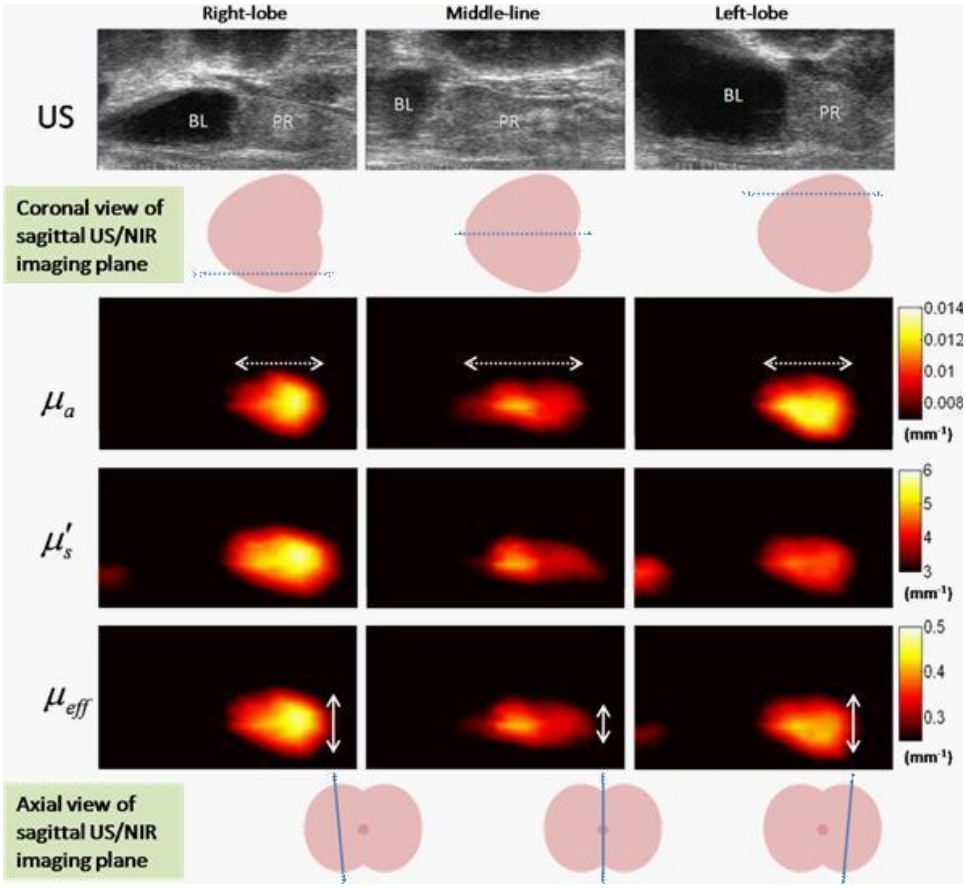

Figure 44 NIR images of normal canine prostate

The NIR absorption coefficient images are displayed at a color-scale of [0.007 0.014] mm^{-1}. The NIR transport scattering coefficient images are displayed at a color-scale of [3.000 6.000] mm^{-1}. The NIR effective attenuation coefficient can be calculated

by previous Equ. 36 From the experiments, the calculated μ_{eff} of normal canine prostate is in the range of [0.250 0.500] mm^{-1}. The color-scales in all images represent a background threshold at half of the maximum value of the color-scale. At this scale, the locations of the NIR regions indicated the prostate had excellent position correlation with prostatic images obtained using TRUS. The urinary bladder is shown as an anechoic structure on TRUS, which is similar to images using NIR. Most of the peri-rectal tissues are also not identified using NIR except at the periphery of the urinary bladder. The prostate is consistently demonstrated in NIR images as having positive-contrast with respect to the peri-prostatic tissues, with an average of more than 2-folds of contrast in absorption, reduced scattering, and effective attenuation. In addition, the prostate is more optically heterogeneous in the middle-line and more optically attenuating toward the internal aspects of the prostate than in the peripheral aspects of the gland.

5.4 Single wavelength NIR imaging of canine prostate with TVT

The TVT model was successfully cultivated on the second dog. The injection procedure was the same as previous description in Section 5.2 and shown in Fig. 45 (a). During retraction of the injection needle, it was assumed that TVT cells could leak from the prostate injection site and be "seeded" along the needle insertion tract.

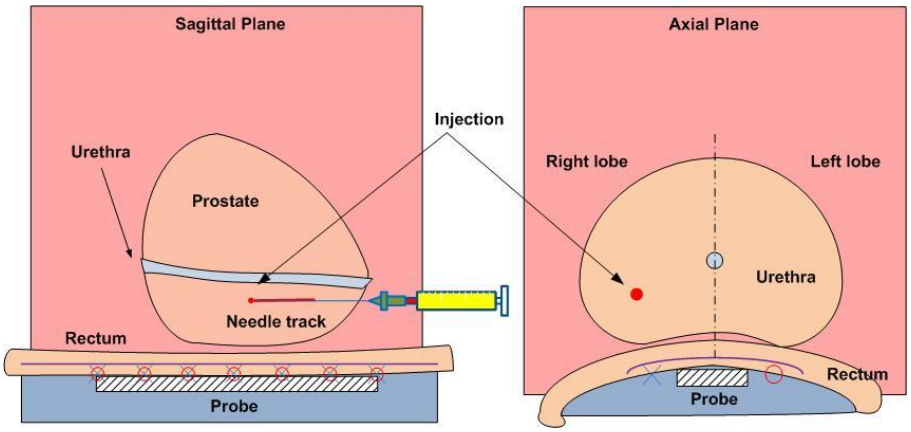

(a) TVT injection of Buck

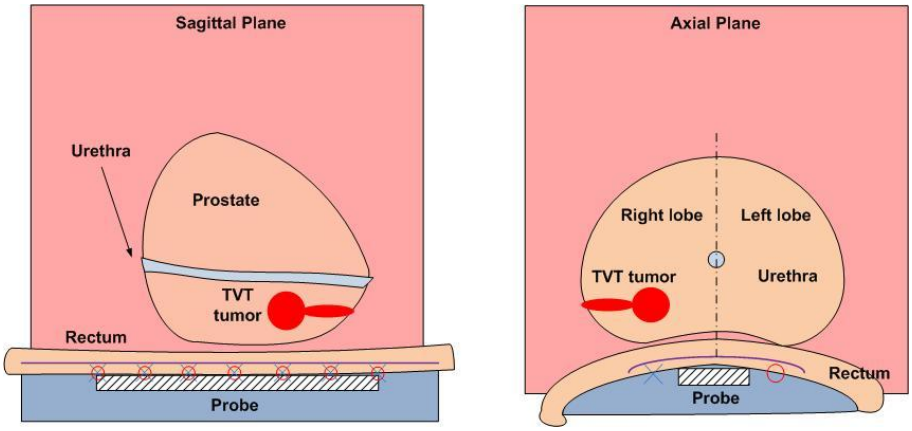

(b) TVT growth ~2 weeks after injection

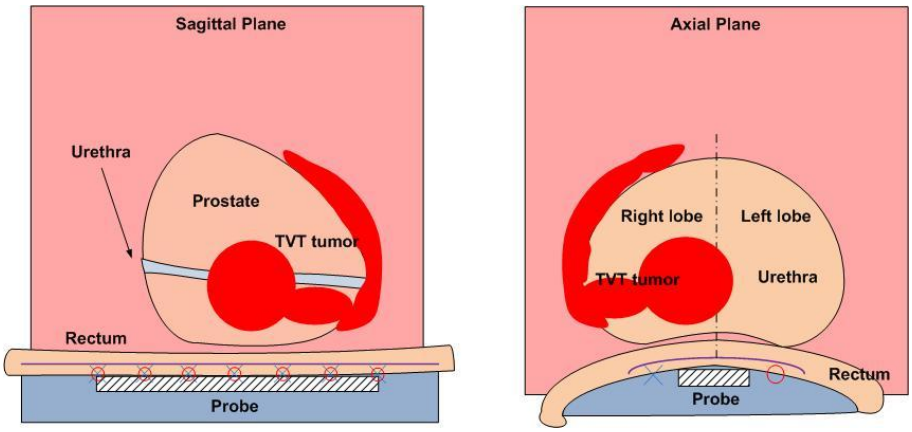

(c) TVT growth ~6 weeks after injection

Figure 45 TVT growth from injection to 6 weeks

In Fig. 45(b), after about 2 weeks, the injected TVT cells grew up both inside of prostate and along the needle track. Some leaked TVT cells started to grow outside of prostate. When 5~6 week passed, in Fig. 45 (c), the inside prostate TVT tumor grew bigger that it crossed the middle line and extended to the left lobe. The outside TVT tumor also became large enough to cover the entire right lobe. All those tumors sketched in Fig. 45 (c) were actually connected with each other [107].

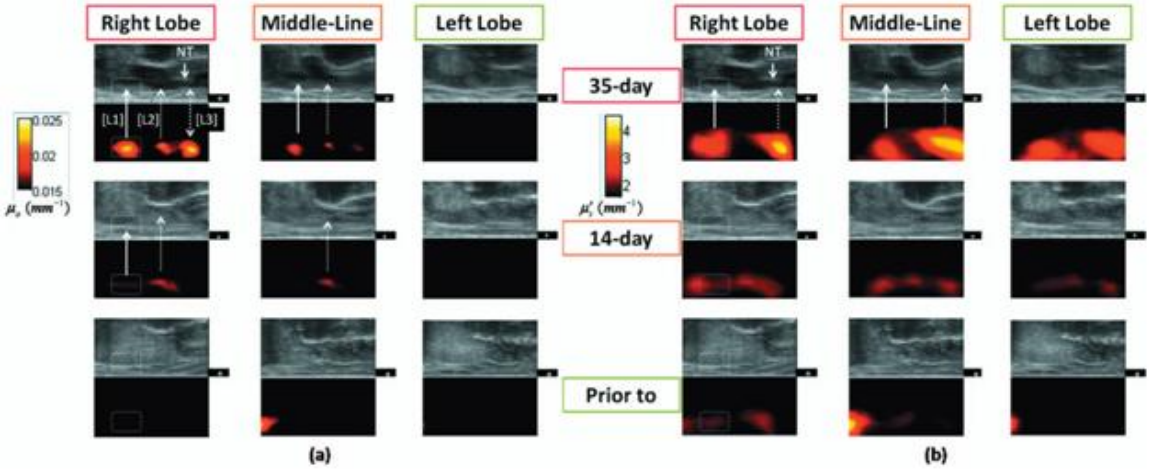

Figure 46 Monitoring of optical absorption and reduced scattering at right lobe, middle-line and left lobe of prostate before the injection, 14 days after injection and 35 days after injection.

Figure 46 presents the trans-rectal NIR and TRUS images acquired at the middle of the right lobe, the middle-line of the prostate, and the middle of the left lobe, which were obtained before the TVT injection, 2 weeks after the TVT injection (when US and rectal examination showed no evidence of tumor growth), and 5 weeks after the TVT injection (when the tumor growth was evident on both US and rectal examination). The absorption (a) and reduced scattering (b) images correlate to the same set of US. The

image dimensions are all 60mm×30mm (cranial-caudal×dorsal-ventral). On the 5th week TRUS images of the right lobe and middle-line, corresponding to Fig. 46, the hypo-echoic region L1 indicated an intra-prostatic mass; the large hypo-echoic region L2 indicated a mass ventral and caudal to the prostate that could have connection with L1; the NT on the right lobe denoted the needle trajectory for introducing the TVT cells with longitudinal hypo-echoic regions including L3 seen along the NT. On the 5th week NIR image of the right lobe the hyper-absorptive regions corresponded longitudinally to L1, L2, and L3. The 5th week NIR image of the middle line displayed less and smaller hyper-absorptive masses indicative of L1, L2, and L3. Trans-rectal NIR/US images performed at the left lobe were shown with no abnormal features on US and no hyper-absorptive regions on NIR. At the 2nd week NIR absorption images, hyper-absorptive regions were found intra-prostatically in the right lobe only (L1) and dorsal to the pelvic bone in the right (L2) with potential extension to the middle line. The longitudinal locations of these hyper-absorptive regions correlated very well with those of the hypo-echoic and hyper-absorptive regions found in the 5th week. It should be noted that the NIR array surface is 3mm ventral to the TRUS surface, therefore the nodules were shown slightly dorsal on NIR than on US. The progression of the dimensions and contrasts of the hyper-absorptive regions from the 2nd week to the 5th week implied tumor growing in right lobe and extending toward the middle-line. It is observed that the growth of the tumor was indicated earlier by the NIR absorption images than by the TRUS, and combining the information of NIR and TRUS led to earlier and more accurate findings of the tumor growth than did with TRUS alone.

The hyper-absorptive masses in Fig. 46(a) were shown in Fig. 46(b) with different patterns of the reduced scattering contrast. On (b) the L3 had much higher contrast than did the other masses corresponding to L1 and L2. The growth of the tumors L1 and L2 at the 2nd week on (b) are not as evident as on (a).

The progressions of the peak NIR absorption and reduced scattering contrasts within the rectangular region corresponding to L1 as outlined in Fig. 46, with respect to the background values for normal peri-rectal parenchyma, are given in Fig. 47. The clear trend of contrast increase is believed as the demonstration of imaging the tumor growth since NIR tomography is a non-linear process in which the enlargement of target may be reconstructed as enhanced contrast in addition to volume changes when reconstructing without the target spatial *prior*.

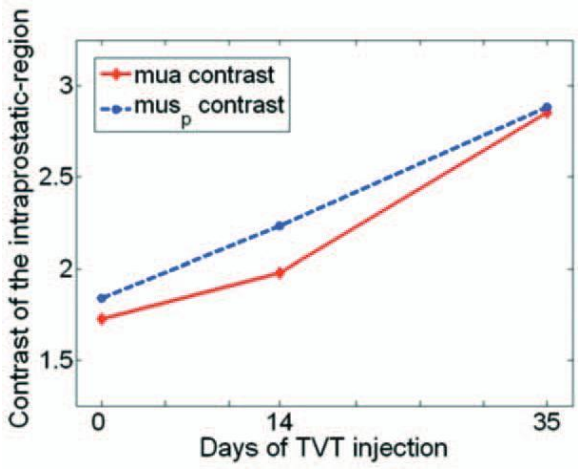

Figure 47 Estimated contrast increase in 5 weeks

Figure 48 displays the sagittal NIR/US images obtained by displacing the probe at 3 longitudinal locations along the middle plane of the right lobe from the cranial side to caudal side. At location 1, the L1, L2 and L3 (referred to Fig. 46) were all within the US field of view, while at location 2 the L3 was moved out of the US view. At location 3

only L1 was shown on US. The overall information of hyper-contrast masses on trans-rectal NIR images correlated well with the US hypo-echoic regions.

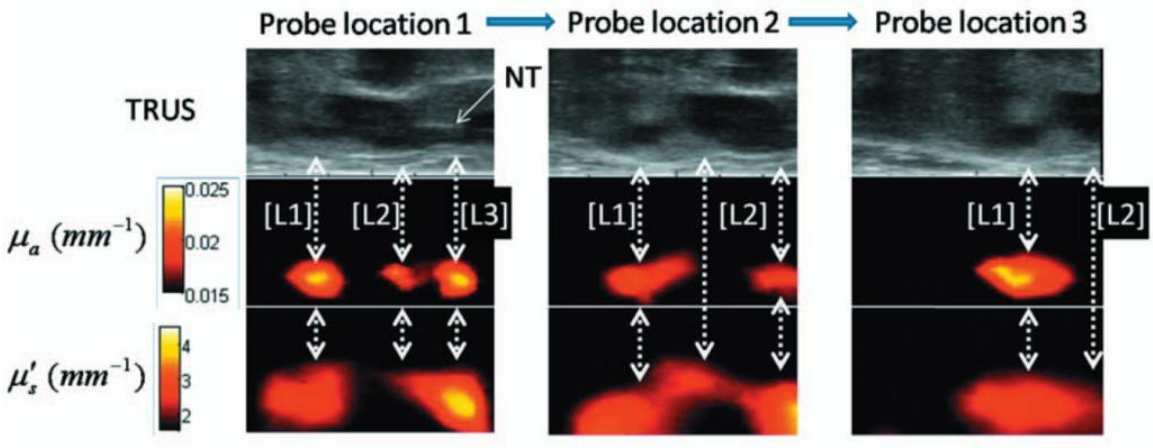

Figure 48 The fifth week imaging of prostate at right lobe

Figure 49 gave a retrospective view of the reduced optical scattering monitored in 6 weeks from the baseline taken right before the TVT injection. For the optical absorption images, at the second week, the hyper-absorption regions were found intraprostatically in the right lobe and dorsal to the pelvic bone. The contrast became significant when 5 weeks passed indicating a malignant tumor growth. The contrast of reduced scattering image during the first two weeks was not as high as absorption contrast, an increased contrast in scattering could still be concluded along the TVT tumor growth in the 5 weeks.

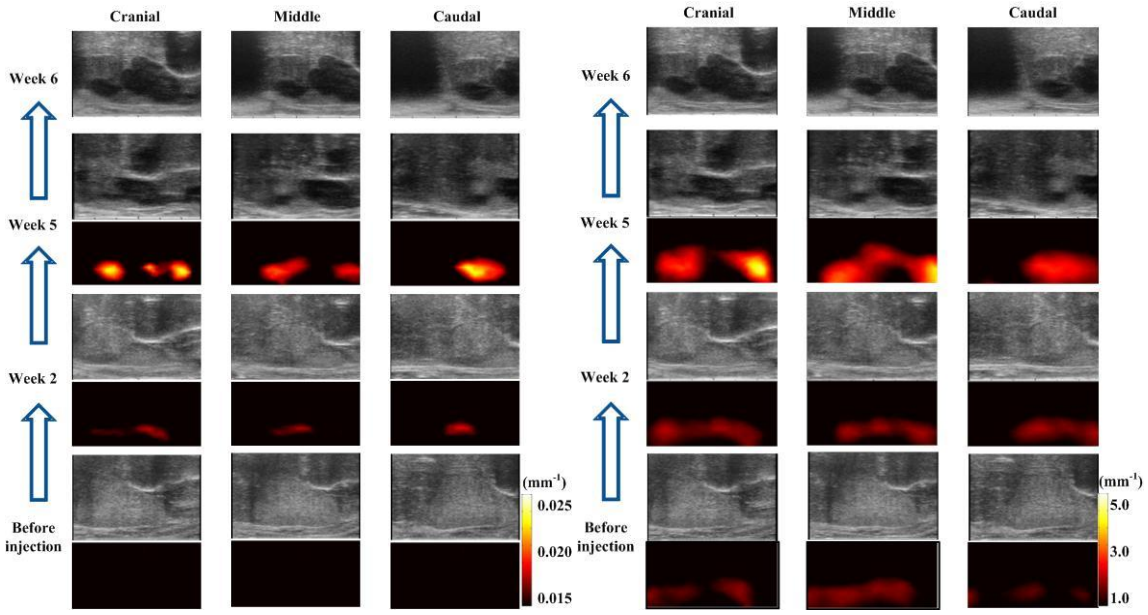

(a) absorption image (b) reduced scattering image

Figure 49 Retrospective view of right lobe monitoring in 6 weeks

NIR optical tomography reconstruction used a 3-D mesh; Fig. 50 displays the three sagittal TRUS images taken at the mid-line of the prostate, the middle portion of the right lobe of the prostate, and the right lateral edge of the prostate. As shown in Fig. 46, the small hypo-echoic region L1 indicates an abnormal intra-prostatic mass. The large hypo-echoic region L2 indicates an abnormal mass anterior and caudal to the prostate that may have connection with L1. The NT on the right lobe US image denotes the needle trajectory for introducing the TVT cells. Longitudinal hypo-echoic regions including L3 are seen along the NT. The three sagittal NIR images correspond to the US taken at the middle portion of the right lobe, 10mm medial to it and 10mm lateral to it, respectively. Hyper-absorptive regions on sagittal NIR images correspond to L1, L2, and L3 on sagittal US images. The 10mm-medial NIR image shows reduced contrast for the absorptive masses, and the 10mm-lateral NIR reveals connected strong absorptive

masses. The bladder is seen as slightly hypo-echoic at the 2 more medial sagittal US images; however, no hyper-absorptive mass is presented at the left-most region of the sagittal NIR images.

The three axial TRUS images were taken at the cranial edge of the prostate crossing L1, the caudal edge of the prostate crossing L2, and the peri-rectal region crossing L3. The axial US images show a small hypo-echoic intra-prostatic mass at cranial side of the prostate, the bulging of the right lobe and extending of the L2 over the prostate mid-line that correlates with the findings on mid-line sagittal US, and large peri-rectal hypo-echoic mass cranial to the perineum. Of the five axial NIR images, the longitudinal positions are 10mm apart from cranial to caudal. The axial NIR image A2 should contain L1, and the axial NIR image A5 should contain L3.

The coronal NIR images correspond to 5mm, 10mm, and 15mm anterior to the anterior edge of the rectal lumen. The hyper-absorptive mass indicative of L1 is seen medial to the hyper-absorptive masses indicative of L2 and L3. The anatomies of the hyper-absorptive masses on the NIR images in 3-views agree with the hypo-echoic regions on the US images in 2-views.

The US and NIR imaging were also performed at the middle-line of the left lobe where no abnormal features were found on the US, and globally homogenous and low absorption was seen in the NIR images.

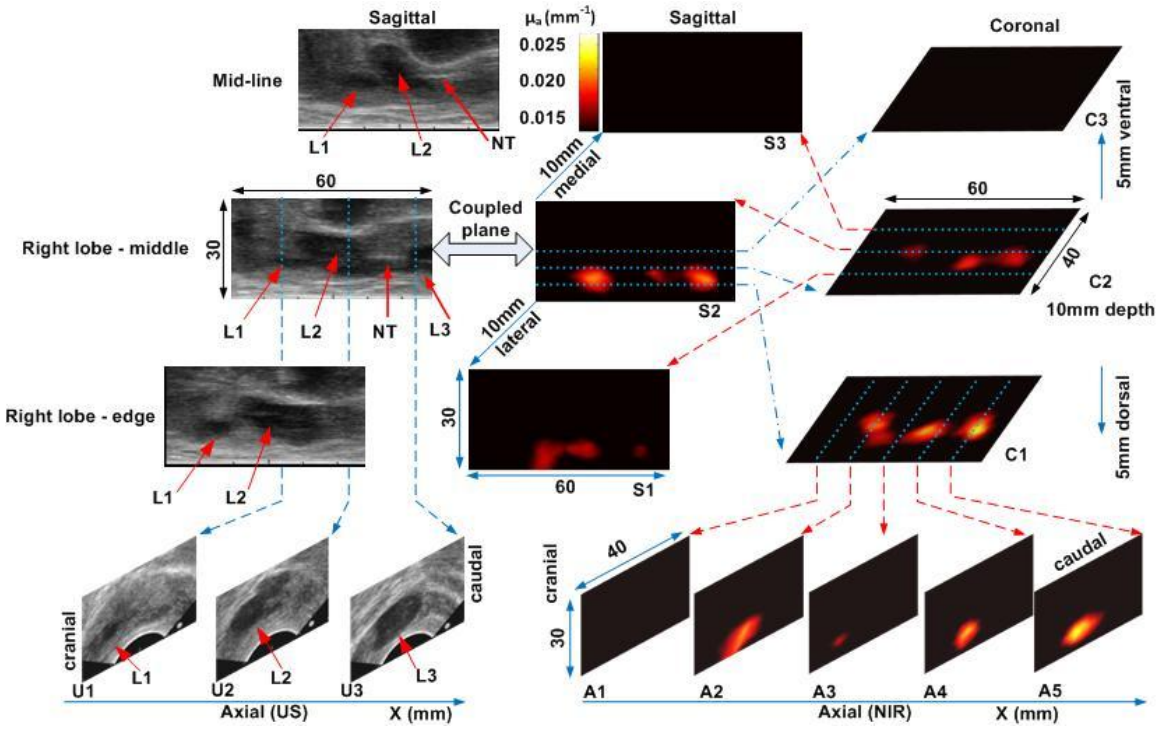

Figure 50 3-D absorption images of prostate at 5th week

With the same data set, the reconstructed reduced scattering optical image was displayed in axial, sagittal and coronal plane accordingly to Fig. 50. The indications of masses corresponding to L1, L2 and L3 are not as profound as in absorption images, although L3 seems much higher contrast than L1 and L2 masses. The scattering contrast looks more heterogeneous compared with the absorption image at a given color scales.

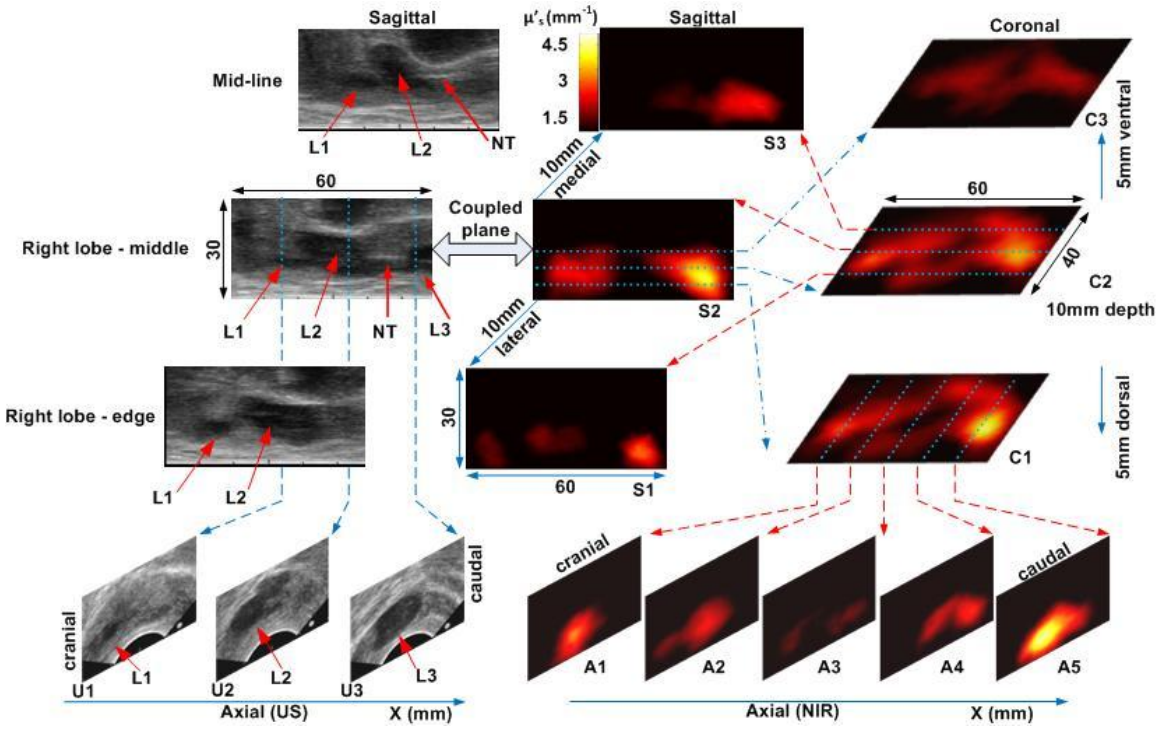

Figure 51 3-D reduced scattering images of prostate at 5th week

The gross and histological findings (obtained 8-week post-injection) illustrated in Fig. 52 confirmed intra- and peri-prostatic neoplastic infiltrates with masses also located along the urethra and peri-rectal tissue; the latter related to dissemination along the needle track during TVT inoculation. All masses consist of diffuse sheets of a monomorphic population of neoplastic round cells dissecting through pre-existing fibrovascular stroma. The neoplastic cells have large hyperchromatic nuclei, single conspicuous nucleoli and moderate amounts of featureless cytoplasm. The cytological features are consistent with canine transmissible venereal tumor (TVT).

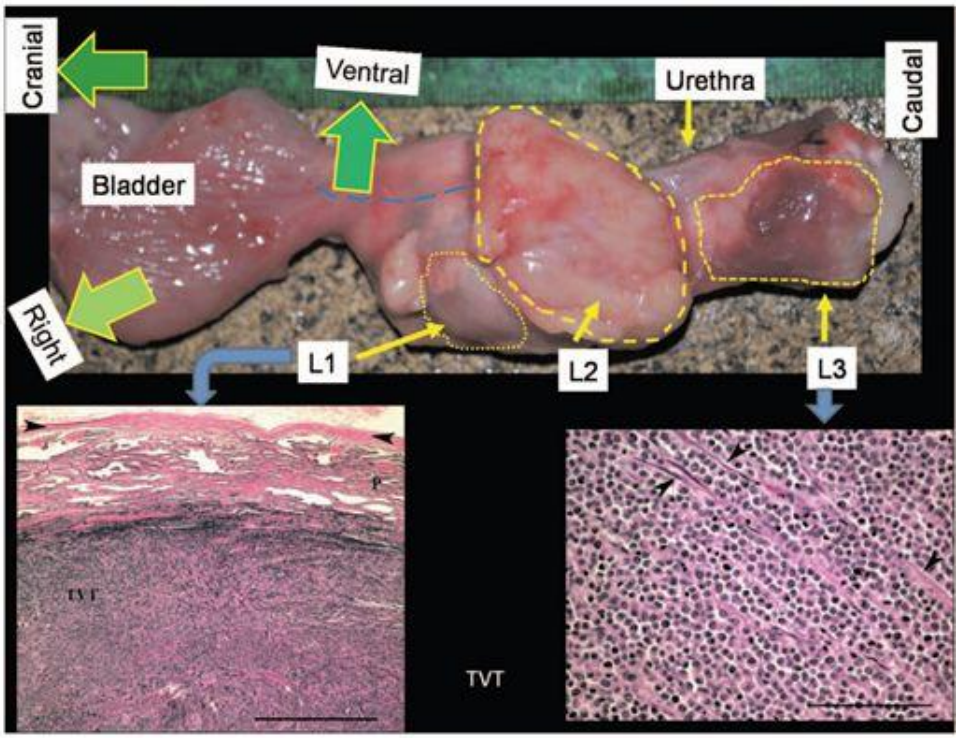

Figure 52 Pathology finding of prostate TVT

The single wavelength NIR optical tomography of prostate imaging results indicated that the combining the information of the optical and ultrasound images could get the chance to find the prostate tumor at its early stage. However it must be noted that the optical reconstruction without *a priori* suffers from the detection sensitivity as discussed in section 4.2. The suspicious regions at around 15mm away to the probe will be reconstructed more accurately than other deep regions or the regions far away from the middle sagittal plane. To apply the anatomic *a priori* information in the optical reconstruction, 3D TRUS system will be helpful in future studies.

CHAPTER VI

Dual band Trans-rectal US/NIR imaging system

In near-infrared (NIR) band the light interacts with tissue at microscopic level, largely by two mechanisms: one is the strong scattering by subcellualr organelles, the other is the dominant absorption by chromophores such as hemoglobin molecules. The utility of non-invasive imaging of the tissue oxygenation by multi-band near-infrared (NIR) light has been recognized for decades. The distinctly different spectra of hemoglobin absorption (Fig. 53) of the NIR light when being oxygenated and deoxygenated have enabled finding lesions of angiogenesis or altered oxygenation indicating malignant changes. It has been well recognized in breast imaging that the increased level of hemoglobin concentration in the micro-vasculature of breast cancer causes an elevation of NIR absorption and alteration of NIR scattering. For a sonographically-suspicious lesion in breast, including the information of total hemoglobin concentration [HbT] in the lesion measured by NIR optical tomography is shown to improve the specificity of breast cancer detection [35][108].

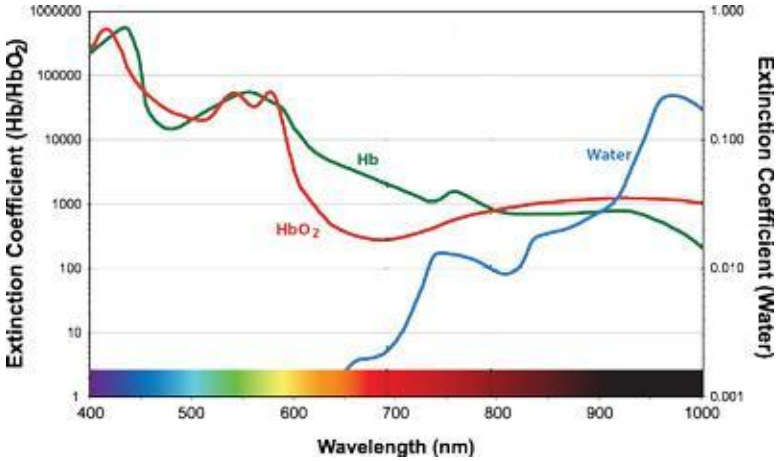

Figure 53 Extinction coefficient of Hb, HbO and water

These findings suggest that augmenting TRUS with NIR measurement of [HbT] in prostate likely will improve the accuracy of detecting prostate cancer. Strong pathological evidences have suggested that the vascular supply to malignant prostate tissue differs from the vascular anatomy of normal prostate tissue. Other studies on prostate cancer have found a correlation between the cancer and increased micro-vessel density. All those studies have demonstrated a clear association of increased microvessel density with the presence of cancer. Several studies on Doppler Ultrasound prostate imaging found it is able to detect signal from small vessels such as those feeding vessels to the microveascular bed, but due to its sensitivity dependence upon motion, it does not detect signals from the microcirculation itself [109]~[113].

Changes of the local oxygen saturation were also observed during the prostate photodynamic therapy under interstitial NIR measurement. Tissue oxygenation status is also an important prognostic indicator for androgen-deprivation therapy of newly diagnosed metastatic prostate cancer. These increasing evidences indicate that the ability

of quantifying the hemoglobin concentration and oxygen saturation in prostate is important for the diagnosis, prognosis, and treatment monitoring [114]~[117].

From previous chapter V, it has been demonstrated that combining trans-rectal NIR absorption measurement of the prostatic tissue at 840nm and the ultrasonography detected the development of a transmissible venereal tumor (TVT) in canine prostate at least a week earlier than by using TRUS alone. The much denser cellular morphology of TVT was related partially to the NIR absorption change seen in that study, but the association of [HbT] with that change was not quantified due to the use of single-band NIR measurement. In previous single wavelength system, the NIR imager superluminescent diode light source with ~14nm bandwidth @ 840nm is used to excite all source channels. The bandwidth would certainly introduce wavelength-dependent attenuation among source channels for those tissue chromophores. The reconstructed absorption coefficient is therefore a value averaged over the band coupled into the source channels. Luckily the absorption of the tissue chromorphores like hemoglobin is less wavelength-dependent in the close vicinity of 840nm. If the source coupling method is performed at an additional wavelength, such as 780nm, to quantify the oxygen saturation, it may be necessary to compensate the wavelength-dependent absorptions among source channels in image reconstruction.

Encouraged by the applications of multi-band NIR light in breast cancer imaging, researchers recently start to develop NIR tomography techniques for trans-rectal imaging of the prostate. In this chapter, the trans-rectal NIR absorption measurement is performed spectrally at 785nm and 830nm that is necessary to extracting the [HbT] of prostatic tissue. This study demonstrates that combining trans-rectal NIR measurement of the

prostatic [HbT] and the ultrasonography likely will detect the lateral involvement and predict the longitudinal development of TVT in canine prostate earlier and collectively more accurate than by using TRUS alone [63].

Initially, before applying two-wavelength light on the trans-rectal NIR tomography system combined with TRUS. It was first applied to a 20mm (Diameter) axial imaging probe at 785nm and 850nm for testing.

6.1 Dual-band trans-rectal axial imaging applicator

Figure 54 illustrates the configuration of the 20mm axial-imaging endo-rectal NIR probe. There are 8 source and 8 detector optical channels spaced circularly. Each optical channel was constructed with a 1.0mm core diameter fiber and aligned to a 45º rod lens of 2mm diameter to deflect the beam transversely for side-firing. A 2mm drum lens was attached for illumination and beam focusing. The length of the probe is 7" which was comparable to a standard TRUS probe [118].

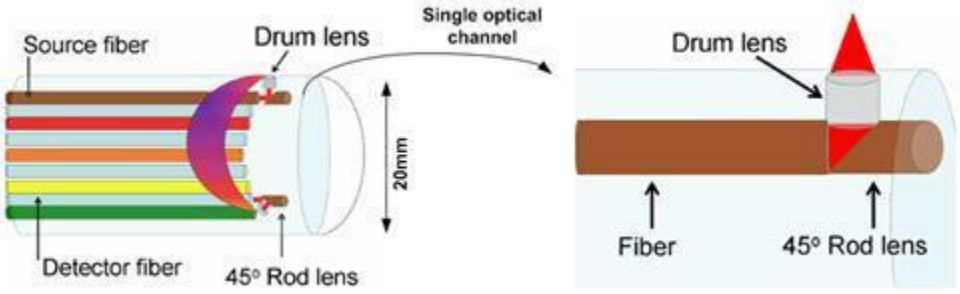

Figure 54. Diagram of 20mm endoscope NIR tomography axial imaging probe

This 20mm diameter probe was connected to a time-multiplexing light delivery setup for dual-band NIR tomography as shown in Fig. 55. The ~100mW outputs from two laser diodes (LDs) at 785nm and 850nm were coupled by a bifurcated fiber to a fiber

switch that was home-made using a linear motorized translation stage (Zaber Technologies) which was basically the same as the single wavelength source switching set up described in section 3.3. The switching of the light upon 8 source channels was synchronized with the CCD acquisition of all those corresponding 8 source signals having been received by all detectors.

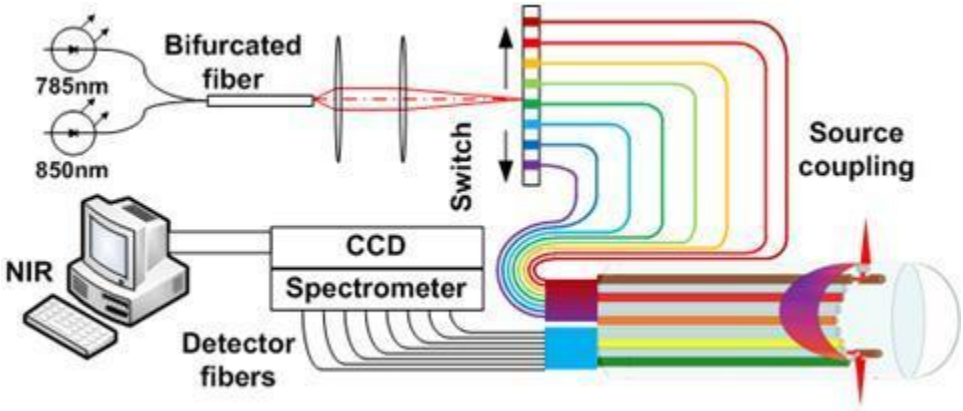

Figure 55 Dual wavelength NIR tomography system for 20mm-probe

Each complete set of the data consists of 8 frames corresponding to each source channel being turned on by the fiber switch. Fig. 56 is the one frame data when the source 3 is switched on. Because of the longer distance between the source and detector, the total 64 data sets follow a better linear fitting curve than the data sets for previous studies on a 13mm probe. The use of fiber switching also minimized the cross-talk among the adjacent source channels. However, the weakest signal may submerge in the background noise owing to the limited dynamic range of the CCD.

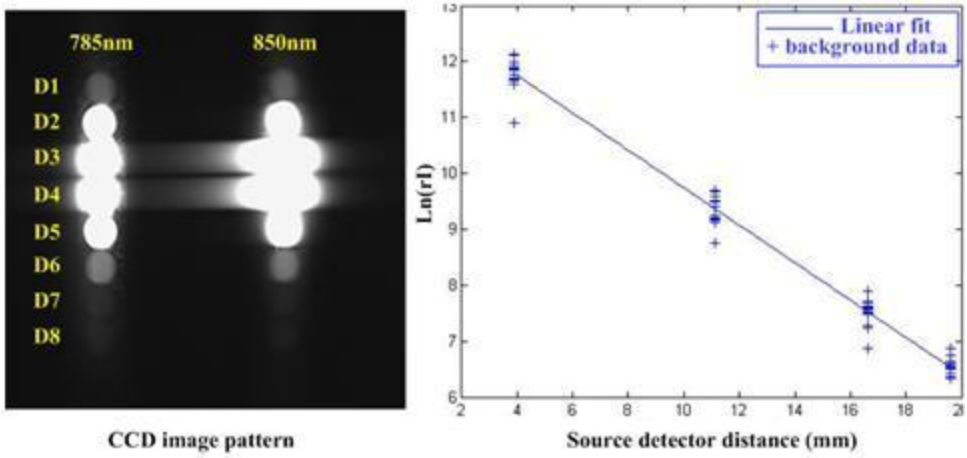

Figure 56 CCD image and raw data of 20mm probe

In the previous measurement by use of the 13mm probe, the 2.5mm separation of the target from the probe surface was too small to be differentiated by the NIR tomography. This is not only related to the relatively low resolution of the NIR tomography, but also to the non-uniform sensitivity of the axial imaging probe along the radial depth as well as the use of continuous-wave measurement that does not give reliable information of the photon path-length. Further test on the 20mm axial-imaging probe confirmed that the depth of a target is severely compromised at this axial-imaging geometry, as indicated in Fig. 57. A solid cylinder shape phantom (10mm in diameter and 16mm in length) was put into a homogeneous background of 1% solution intralipid. The phantom was put 10mm away (center) from the 20mm probe surface. The solid phantom has the optical coefficients of μ_a = 0.0064mm^{-1}, μ_s' = 0.91mm^{-1}. The high absorption regions reconstructed at two wavelengths are consistent, but at a position close to the probe surface. Improving the depth localization of the axial-imaging NIR tomography may be rendered by incorporating spatial information of the target. Yet, the curvature of the axial-imaging geometry may limit the depth of target being detected.

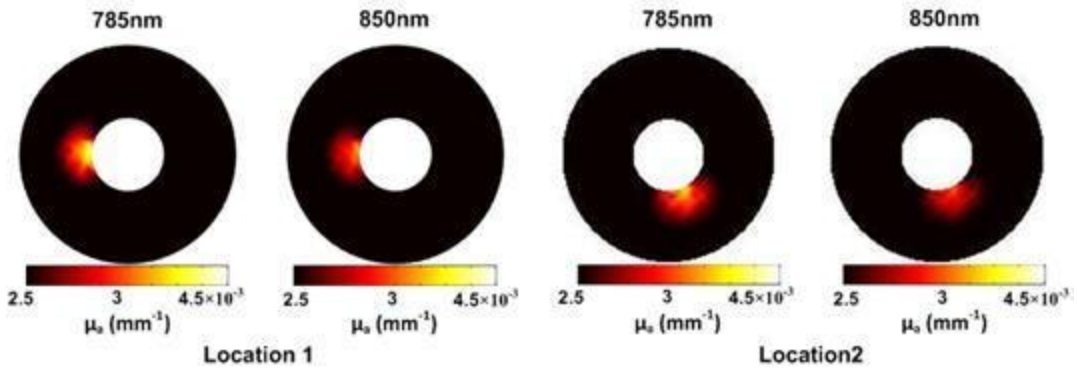

Figure 57 Stand-alone optical reconstruction of transverse images

After the initial validation of the dual-band system on the axial imaging probe, the system was applied on the trans-rectal sagittal imaging probe.

6.2 Dual-band trans-rectal sagittal imaging system

The upgraded TRUS/NIR system for dual-band trans-rectal mode imaging is shown schematically in Fig. 58 and photographed in Fig. 59. Two-wavelength light at 830nm and 785nm were coupled in the source channel by a bifurcated fiber delivered to the switching source coupling system. The 7 NIR detector channels are coupled to a spectrograph of 300mm focal-length and 300 lines/mm grating, which separated the 7-channel dual-band light onto an intensified CCD camera with 12mm×12mm chip size and 16-bit resolution which is the same as previous described CCD in section 3.2.

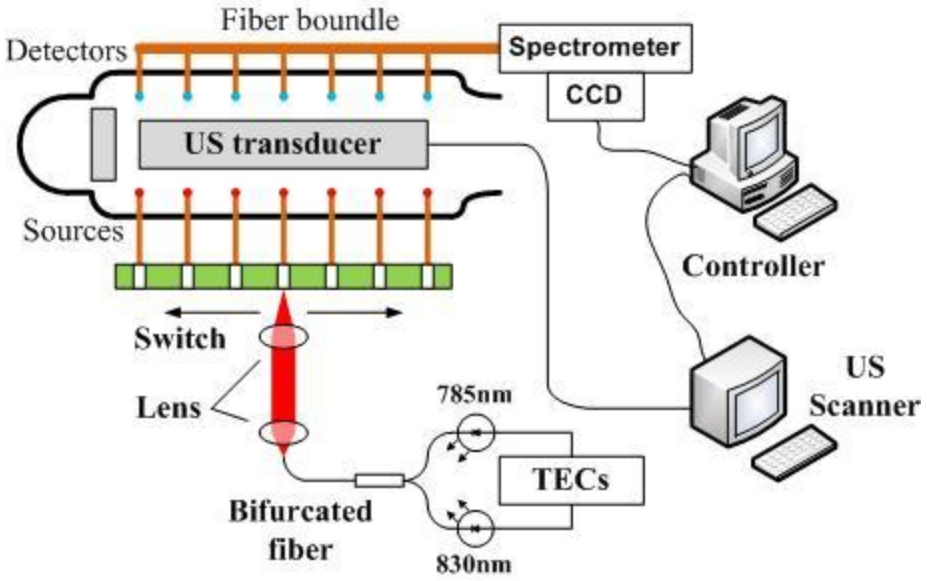

Figure 58 Dual-band optical imaging system

The Laser diodes were mounted in the temperature controlled laser diode mounts (TCLDM) from Thorlabs, both of which were connected to two laser diode controller (LDC-3722B ILX Light wave Inc.). The TCLDM9 uses two thermo-electric coolers (TEC) to precisely regulate the operating temperature of a laser diode. Each TEC element is capable of up 10W of cooling at a maximum operating current of 5 Amps. The two TECs are connected in series so that a single connection provides up to 20W of cooling. Temperature sensing is done by one of two ways. An AD592 Temperature Transducer provides a linear temperature monitor proportional to the laser temperature in degrees Celsius. A 10kΩ NTC thermistor is also provided for controllers that only work with thermistor feedback. It also has a 50Ω RF input using a bias-tee allows the laser to be directly modulated up to 500MHz.

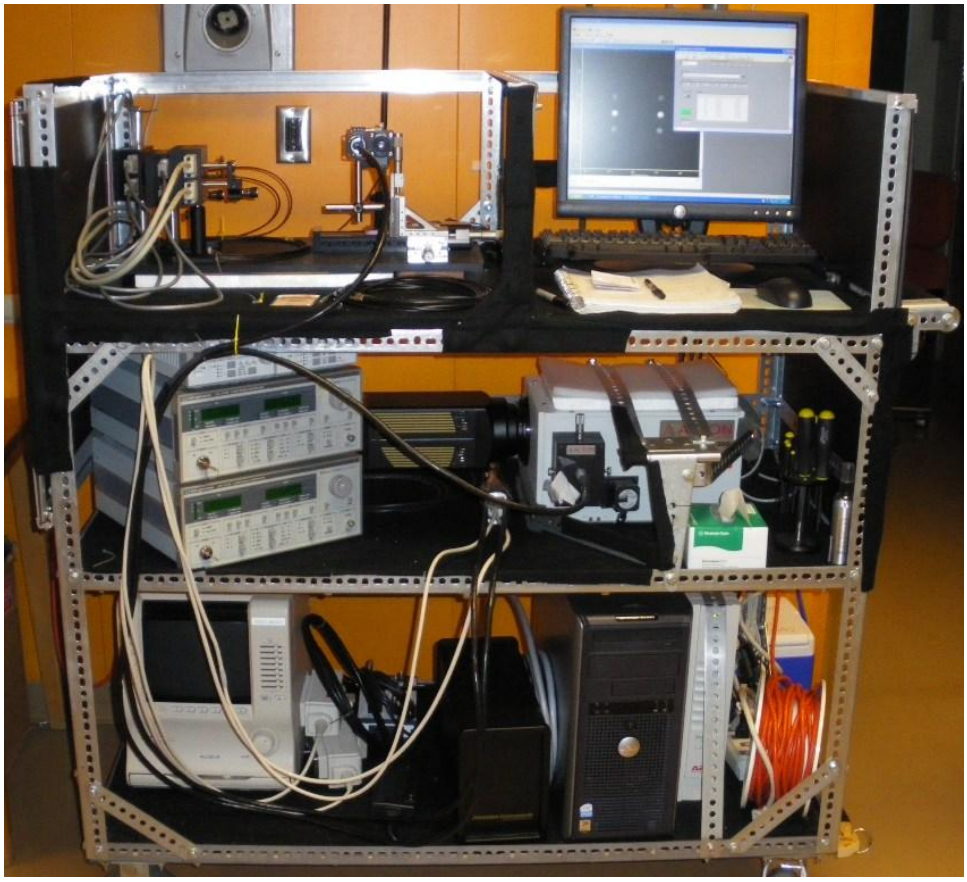

Figure 59 Photography of multi-band optical imaging system

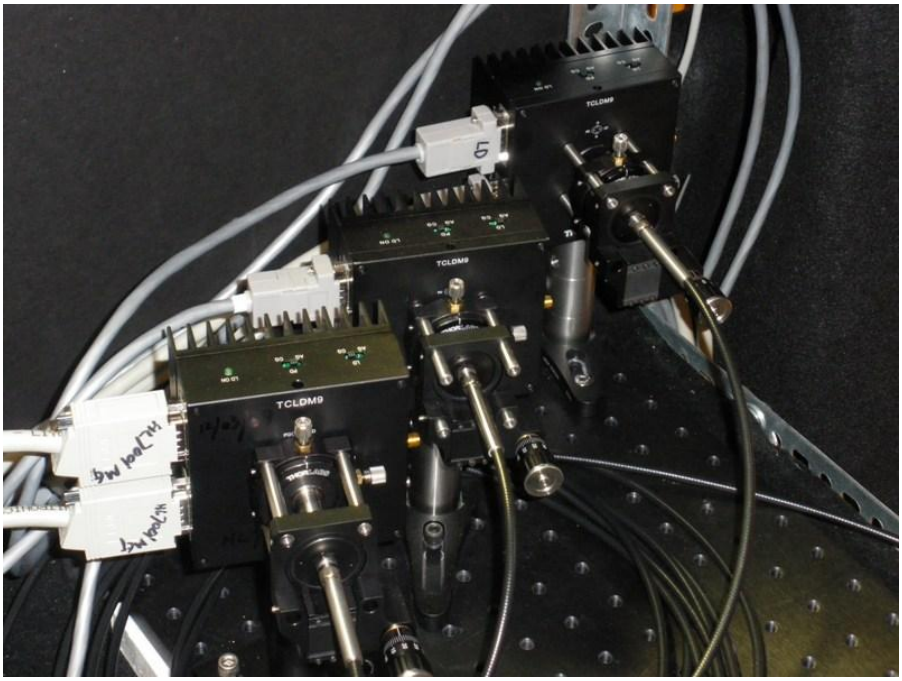

Figure 60 Temperature controlled laser diode mount

Two cables of the laser diode driver and temperature controller have to be home-made because that the pin-definitions of LDC-3722B are different from TCLDM9. The connection of LDC-3722B and TCLDM9 was shown in Appedices2.

Figure 61 Front panel of laser diode controller

One set image in the test of those two wavelength separated by spectrometer is given in Fig. 62. Both of the acquired two wavelength data sets were calibrated by the linear model based on the semi-infinite boundary condition described in section 4.1.

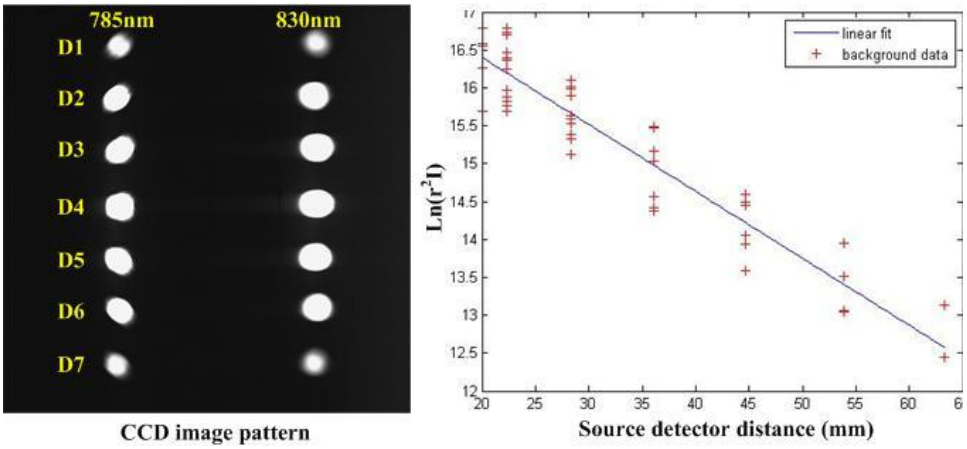

Figure 62 CCD image of dual-band optical measurement

The dual-band measurements of absorption on sagittal-plane are reconstructed by optical stand-alone reconstruction in Fig. 63.

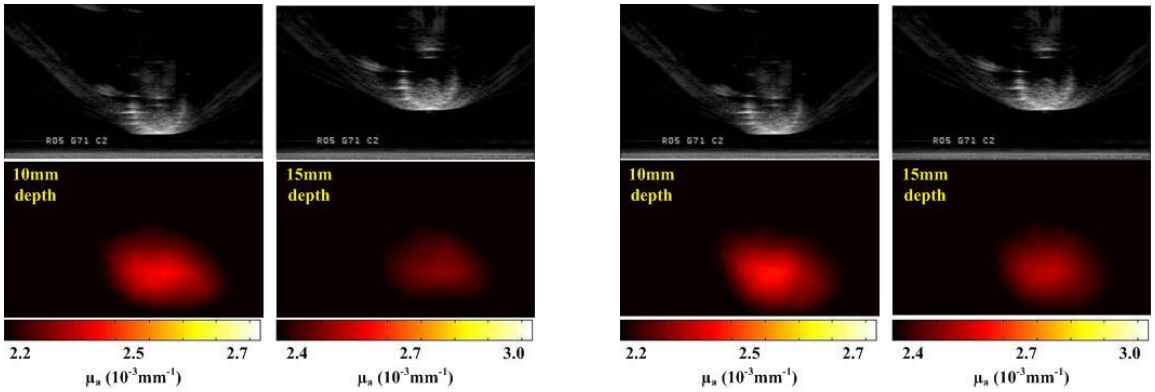

(a) 785nm (b) 830nm

Figure 63 Stand-alone optical imaging of dual-band system

In Fig. 63, a solid phantom target (μ_a =0.0056mm^{-1}, μ_s' =1.03mm^{-1}) was put in the middle-sagittal plane of the probe at a depth of 10mm and 15mm, respectively, in a homogeneous background (1% solution intralipid). Both targets appear approximately at the same depth of 10mm by NIR optical stand-alone reconstruction corresponding to the depth sensitivity of the probe discussed in previous section 4.3. Again, the absorption value of the target is underestimated because of the stand-alone optical reconstruction. Fig. 64 gives the dual-band reconstruction after incorporating the spatial information of the target available from the TRUS. The target spatial information is used to develop a mesh representing a target at the correct location and the background. The *prior*-guided NIR reconstruction at both wavelengths gives more accurate recovery of the absorption coefficient of the target [118].

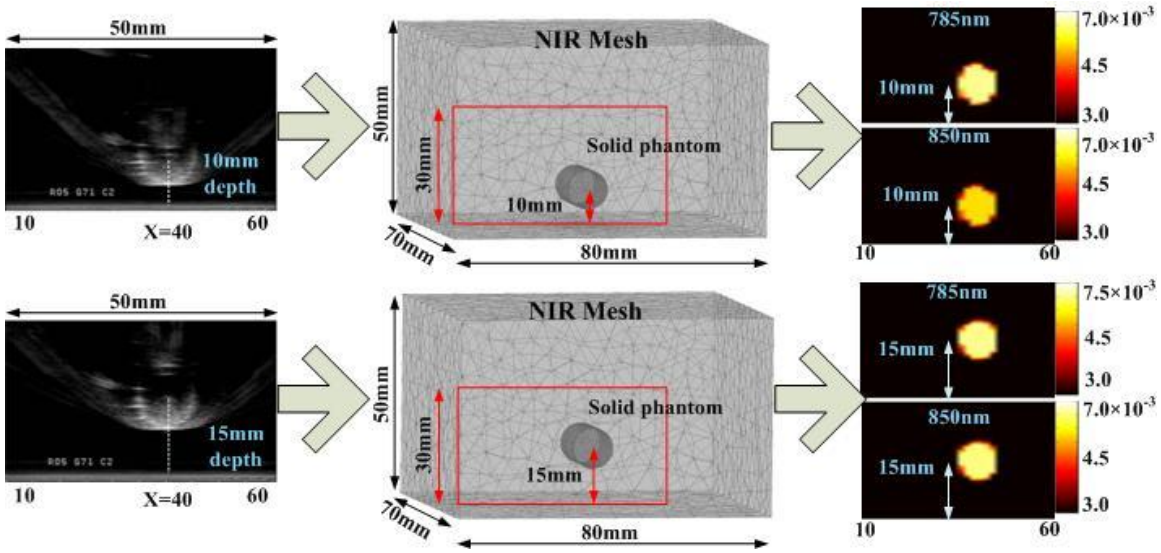

Figure 64 *prior*-guided reconstruction incorporated in dual-band imaging system

6.3 Calibration of dual-band optical system

From the discussion in section 2.1, different chromphores concentration can be calculated from the optical absorption value. In this dual-band optical system, the absorption coefficients at 785nm ($\mu_a^{\lambda_1}$) and 830nm ($\mu_a^{\lambda_2}$) are reconstructed first, then concentrations of the oxygenated and deoxygenated hemoglobin are calculated by the following equations:

$$[HbO]=\frac{\mu_a^{\lambda_1}\cdot e_{Hb}^{\lambda_2}-\mu_a^{\lambda_2}e_{Hb}^{\lambda_1}}{e_{HbO}^{\lambda_1}\cdot e_{Hb}^{\lambda_2}-e_{HbO}^{\lambda_2}\cdot e_{Hb}^{\lambda_1}} \qquad \text{Equation 42}$$

$$[Hb]=\frac{\mu_a^{\lambda_1}\cdot e_{HbO}^{\lambda_2}-\mu_a^{\lambda_1}\cdot e_{HbO}^{\lambda_2}}{e_{Hb}^{\lambda_1}\cdot e_{HbO}^{\lambda_2}-e_{Hb}^{\lambda_2}\cdot e_{HbO}^{\lambda_1}} \qquad \text{Equation 43}$$

where e^{λ} denotes the molar absorption coefficient as shown in section2.1. Summation of these two concentration values leads to the total hemoglobin:

$$[HbT]=[HbO]+[Hb] \qquad \text{Equation 44}$$

And the oxygen saturation is defined as the ratio of the oxygenized hemoglobin to the total hemoglobin as Equ. 45

$$StO_2 = \frac{[HbO]}{[HbT]} \qquad \text{Equation 45}$$

The initial system calibration test set up was built as described in Fig. 65. A similar blood circulation system was built for a 13mm axial imaging probe test. It was demonstrated that the blood oxygen changes can be obtained by a dual-band endo-rectal optical measurement. In Fig. 65, Oxygen and Nitrogen gas tanks were introduced to the fresh bovine blood (300mL) in a tank to administer the level of blood oxygen saturation (StO2) which was monitored by an oxi-meter. A pump delivered the blood from the tank to a cylindrical container (40mm in length with 20mm in diameter) placed 15mm away from the endo-rectal NIR probe (center to the probe surface). The cylindrical container for imaging was made by the solid phantom material used in the system calibration to reduce the photon reflection on the interface of the container and the intralipid. The wall of the container is fabricated as thin as possible (<0.5mm) to minimize the attenuation effect. Test started from the lowest StO2 level in the blood and stopped when it became saturated [119][120].

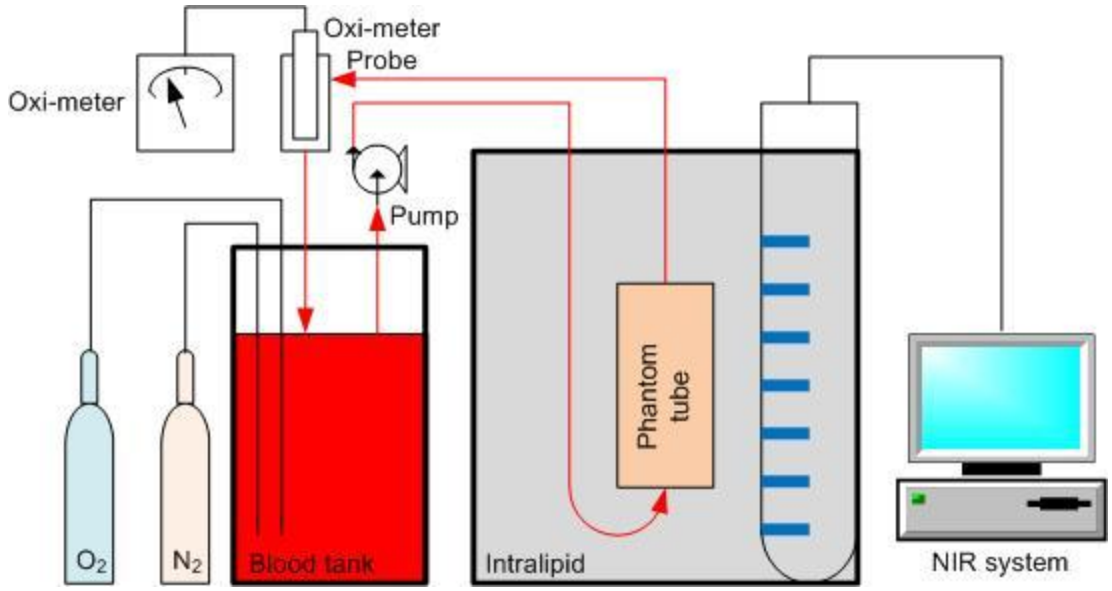

Figure 65 Set up of blood oxygen test

In order to quantify the system performance of the dual-wavelength system, the absorptions in dual-wavelength were reconstructed with *a priori* information from US image. Then by using the Equ. 42~45. the StO2 in the blood can be calculated. Fig. 66 gives the reconstructed blood oxygen concentration with respect to the measurements from the Oxi-meter. The increased oxygen saturation was recovered.

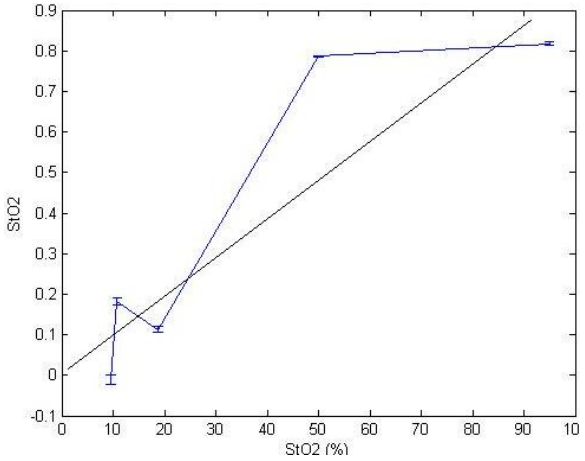

Figure 66 Experimental results of increased StO2

The [HbT] measurement was calibrated using different concentrations of fresh bovine blood, whose optical absorption spectra in 780-840nm are considerably close to that of human blood. The bovine blood was held in a cylindrical container fabricated out of a tissue-mimicking material, which was placed in bulk 1% intralipid solution with optical properties similar to typical soft tissue.

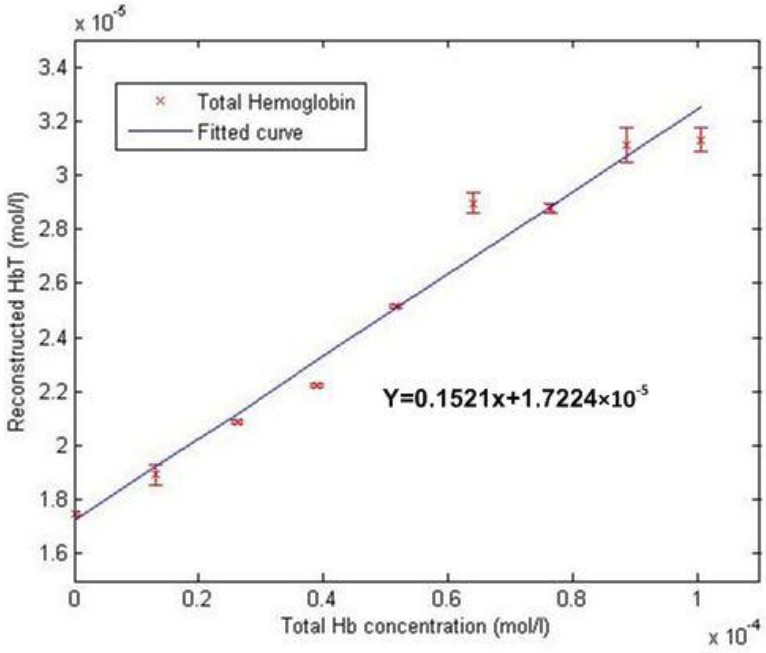

Figure 67 [HbT] calibration with bovine blood in 1% Intralipid

The [HbT] measurements were performed at different locations and distances of the blood-container with respect to the NIR applicator. On average a linear relationship was established between the measured and set values of [HbT], above a residual point as is shown in Fig. 67. Another calibration of StO2 was performed with a sodium dithionite ($Na_2O_4S_2$). Dithionite induces dissociation of dioxygen by the reduction of the external dioxygen and not by diffusion into the cell. So the structure and function of the cell membrane remains relatively unchanged. In the experiments, the blood was divided into

several 10g samples. Sodium dithionite was added by 5mg, 10mg, 15mg and 20mg accordingly. Since sodium dithionite did not change [HbT], Fig. 68(a) gave a pretty stable line for both reconstructions with or without *a priori*. The reconstructed [HbT] with *a priori* is obviously more close to true [HbT] values of the blood samples [121][122].

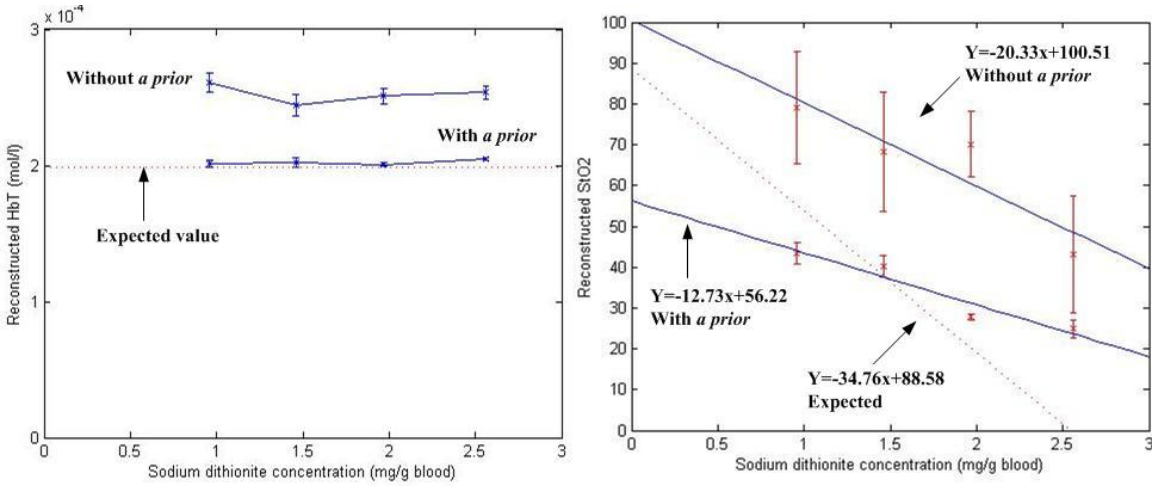

(a) [HbT] (b) StO2

Figure 68 Calibration with bovine blood added by sodium dithionite

The reconstructed StO2 was shown in Figure 6.15 (b). The decreasing trend of the StO2 was recovered but the accuracy of the StO2 for both reconstruction with or without *a priori* were still quite different from the expected value. Each error-bar calculated in the figure has five data sets, the *a priori* reconstruction gives a better consistent results than the stand-alone optical reconstruction. Some previous studies addressed that the combination of 785nm and 830nm was good for [HbT] reconstruction, but for StO2, the reconstructed images were not reliable and consistent.

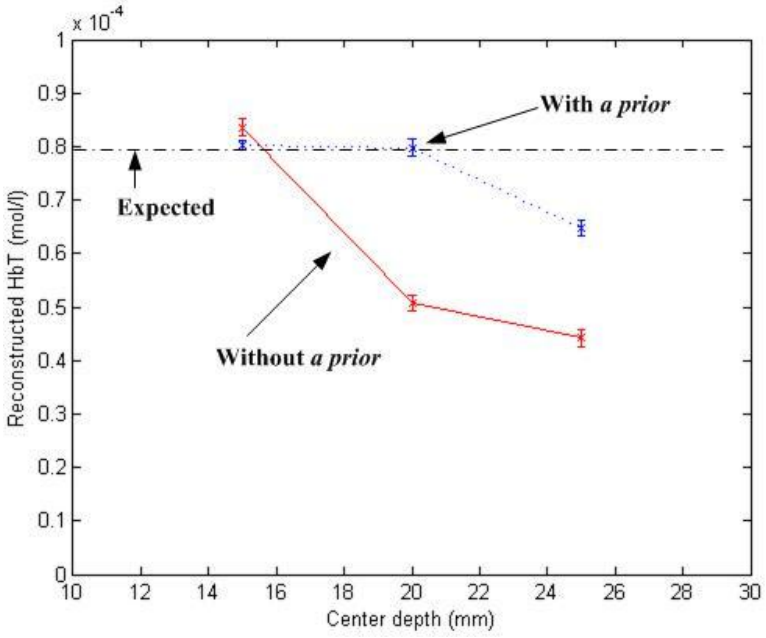

Figure 69 Comparison of [HbT] reconstruction with and without *prior*

As previous discussion in section 3.2, the depth sensitivity problem still exists in the dual-band optical reconstruction. Fig. 69 gives a comparison of reconstructions at different depth with and without *prior*. The target in the experiment was a cylinder shape as described in section 3.1 and was put at the middle of the probe with different depth from 15mm to 25mm. The background is a 0.2% intralipid added with ink that had absorption of 0.0125mm^{-1} and a reduced scattering around 0.2mm^{-1}. The blood sample was diluted by saline water to a 10% solution. Both of the reconstructed absorption values are close to the true value. However, with the depth increased the reconstructed value without *a priori* decreases dramatically when the target depth is more than 15mm away to the probe. For reconstruction with *a prior*, it starts to decrease when the imaging depth is over than 25mm.

6.4 *In-vivo* dual-band TRUS/NIR imaging of canine prostate with TVT

The dual-band *in-vivo* canine prostate study was approved by the Institutional Animal Care and Use Committee of Oklahoma State University. The canine protocol was also inspected on-site by the U.S. Army Medical Research and Material Command. As described at the beginning of chapter 5. The third dog "Buck" was an adult 20-kg, intact male, foxhound estimated to be six years of age was used. Three week baseline images before the TVT cell injection were taken as comparison to the post-injection images. Under general anesthesia, ~3 cc of TVT cells were aseptically injected transperineally into the right lobe of the prostate using a 6-in. 16-gauge hypodermic needle, via US visualization using an Aloka UST-9132I convex array multi-frequency (3.75-10 MHz) finger-grip transducer. The TVT cells were confined within the right prostatic lobe during the injection in two locations, one near the cranial aspect, and the second slightly caudal to the mid-point of the right lobe as the needle was withdrawn. The dog then underwent monitoring, including digitally palpated trans-rectal examination, trans-rectal US and trans-rectal optical tomography, at 7, 14, 21, 31, 38, and 45 days post-injection. Doppler US evaluations were performed after 38 days post-injection at several positions.

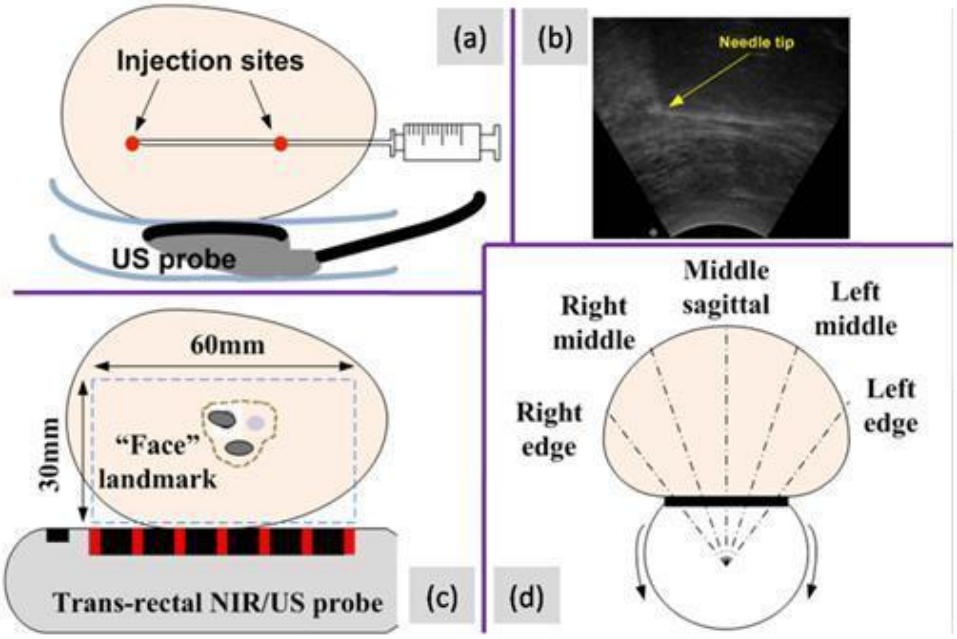

Figure 70 Injection of the TVT cells for Buck, the 3rd canine subject

The base-line US indicated that the prostate measured 6cm from cranial to caudal. It also revealed a cluster of prostatic cysts resembling a "face" in the right aspect of the gland. This "face" landmark, the location of which is shown in Fig. 70(c), facilitated multiple images taken in the same relative areas in that location over time throughout the course of the imaging study. Transrectal optical tomography was performed on five quasi-sagittal planes across the prostate, including the middle-sagittal plane, half-way to the right lateral edge, the right lateral edge, half-way to the left lateral edge, and the left lateral edge, of the prostate gland as shown in Fig. 70(d). On each of the five quasi-sagittal planes, the imaging was performed at three different longitudinal positions of the prostate with respect to the applicator for cross-validation.

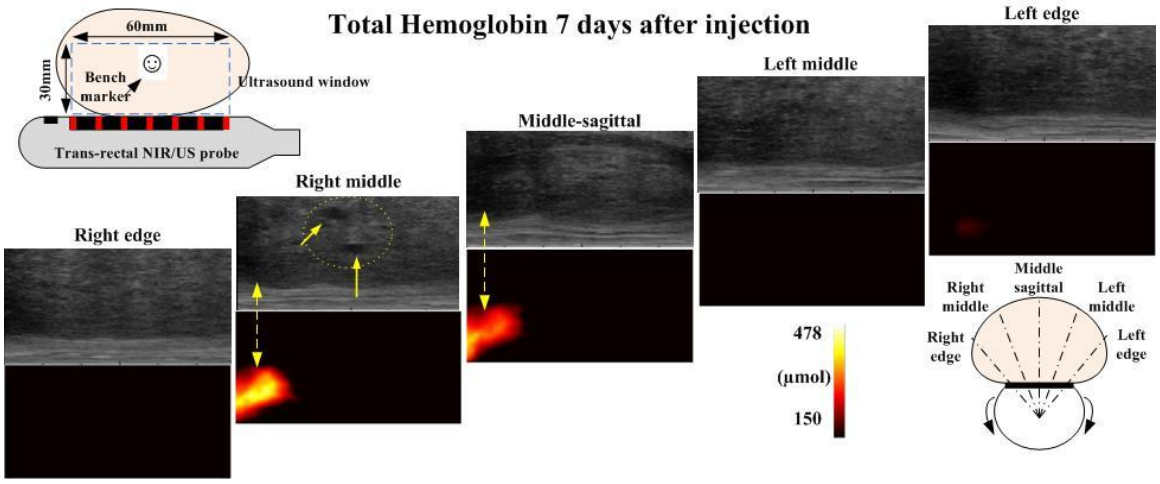

Figure 71 TRUS/NIR images of 5 sagittal planes at 7 days after injection

Among the US/NIR images, only the representative sets corresponding to 7-days and 31-days post-injection were presented in Fig. 71 and Fig. 72. Each group of images for the 7-days and 31-days were taken at two positions, as indicated by the ~25mm shift of the "face" landmark. On US, the "face" landmark was clearly visible by 7-days but distorted significantly by 31-days. The 7-days image revealed a region with higher [HbT] in NIR images and hypo-echoic, near the cranial injection site in the right lobe. That region-of-interest disappeared in images taken 14-days and after, therefore it were thought likely due to hemorrhaging and inflammation at the injection site.

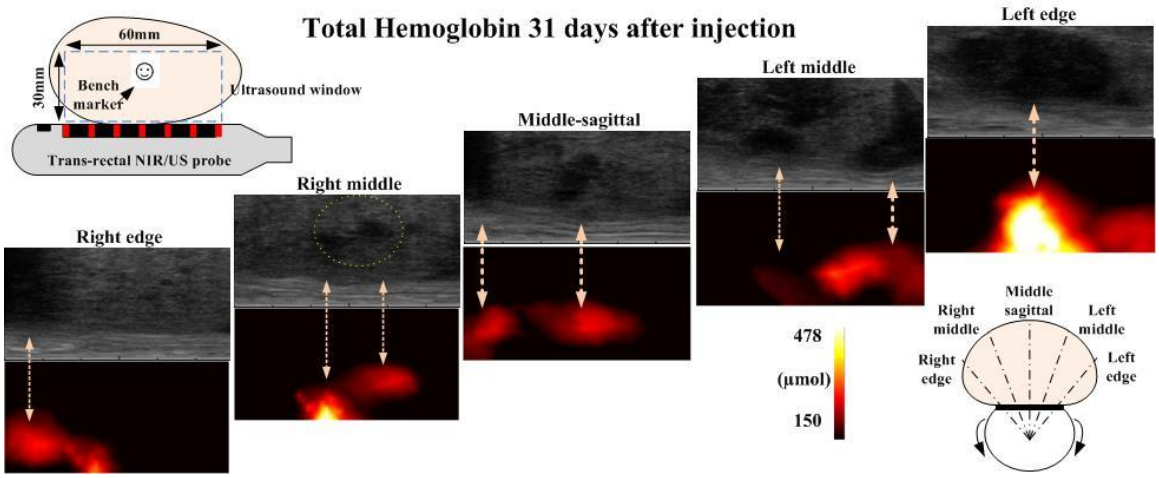

Figure 72 TRUS/NIR images of 5 sagittal planes at 31 days after injection

The US images at 31-days post injection revealed a cluster of hypoechoic masses with irregular-boundaries in the caudal aspect of both right and left lobes and overall greater volume of the hypoechoic masses in the left lobe than in the right lobe. The spatial content of the NIR hyper-[HbT] regions generally agree with that of the US hypo-echoic regions in the caudal-to-middle-left aspect of the gland, but presented a different pattern in the cranial-to-right aspect of the gland. The US presented a large hetero-echoic mass dorsal-cranial to the pelvic bone and extending predominantly to the left lobe but also having right-lobe involvement. Near that location the corresponding NIR image revealed a cluster of hyper-[HbT] region, but the center of which seemed displaced slightly cranially with respect to that of US hypo-echoic mass. Retrospectively in the 7-days NIR images a smaller but stronger hyper-[HbT] region was found near that location. Also in the 7-days US images a substantially smaller hypoechoic region was weakly distinguishable near that location. The location of the hyper-[HbT] region also displaced slightly cranially with respect to that of the marked US hypoechoic mass in 7-days images as well. This hypoechoic mass, developing much more rapidly than other masses,

presented marked enhancement of periphery blood flow when imaged by Doppler US at 38-days post-injection.

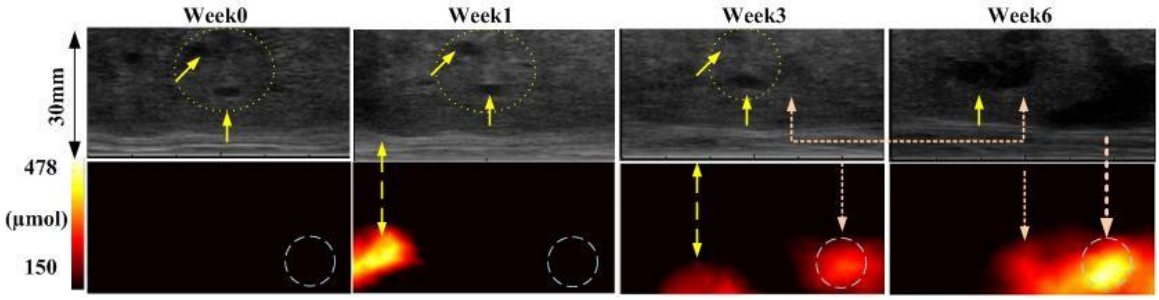

Figure 73 TRUS/NIR images over 4 weeks in right lobe

Figure 73 illustrates the changes of [HbT] of the prostate right lobe middle-sagittal plane from baseline to 45-days post-injection. In a marked 10mm-diameter region, which correlated to the US hypo-echoic mass grown caudal to the prostate. The average [HbT] in that region changed from 120 μM to 375 μM, nearly 300% change over the 45-days of development (shown in Fig. 74). The [HbT] values obtained in this study agree with the range indicated by other works by time-resolved measurement as shown in previous Table1 and previous optical measurement of canine blood [122].

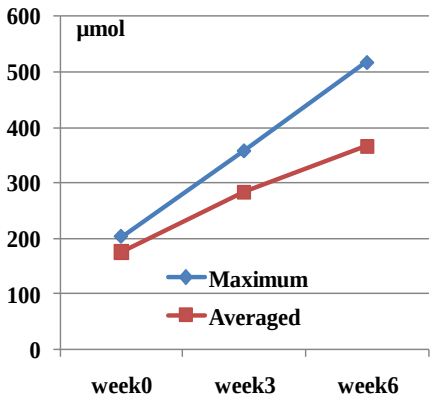

Figure 74 Estimated [HbT] changes during 6 weeks after injection

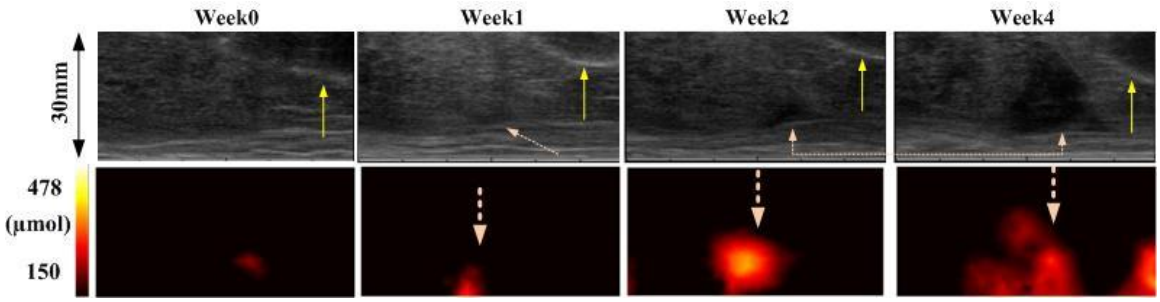

Figure 75 TRUS/NIR images over 4 weeks in left lobe

Another sets of TRUS/NIR images of left lobe prostate from week 0 to week4 are shown in Fig. 75. Since the injection was at the right lobe, at week1, there was no similar high contrast pattern as right lobe in Fig. 76. However, the leaked TVT cells started to grow in the left lobe in early weeks which was observed at week 1 and week2. In week 4, the tumor mass became big volume at caudal to prostate.

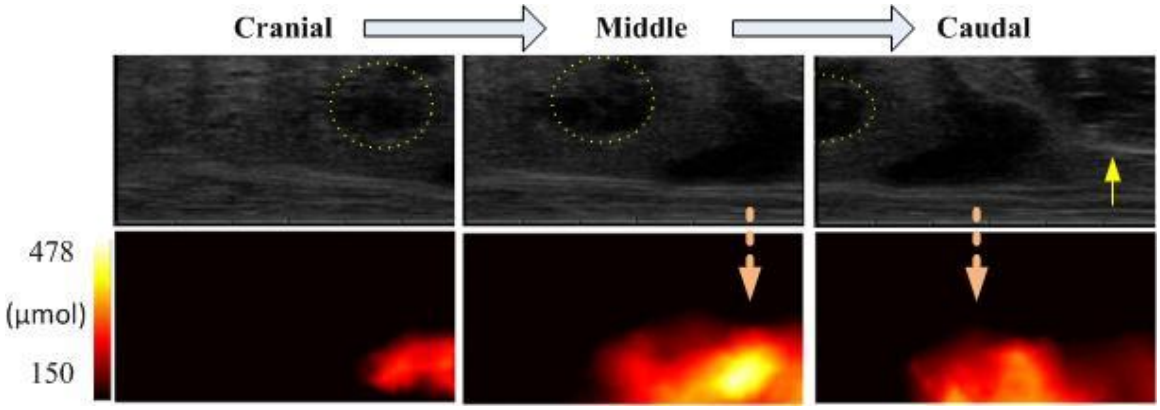

Figure 76 Dog3 week6 at right lobe

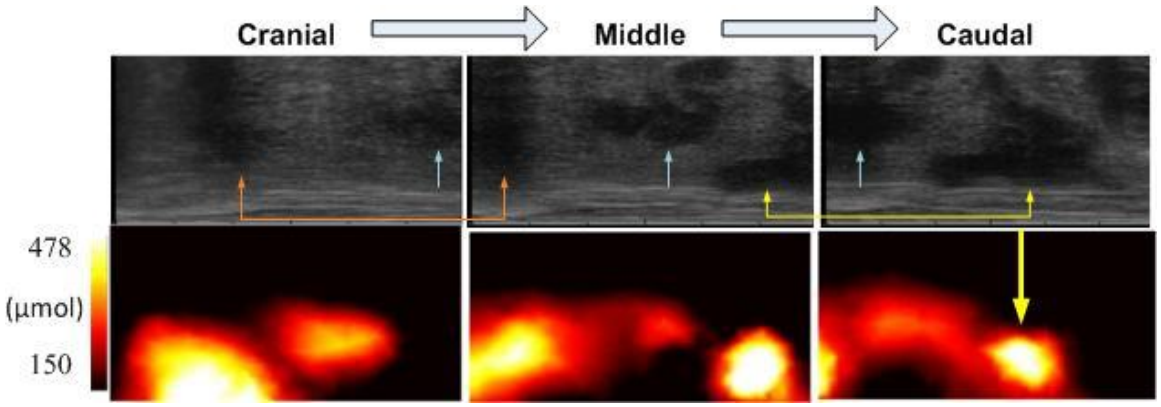

Figure 77 Dog3 week7 at right lobe

Figure 76 and 77 showed the right lobe prostate TRUS/NIR images at the middle-sagittal plane after 6 weeks and 7 weeks post-injection. The images were acquired at those three different longitudinal locations from the cranial to prostate, middle of the prostate to the caudal of the prostate. The hyper-contrast region of [HbT] correlated with the hypo-echoic region in TRUS images indicating the tumor mass.

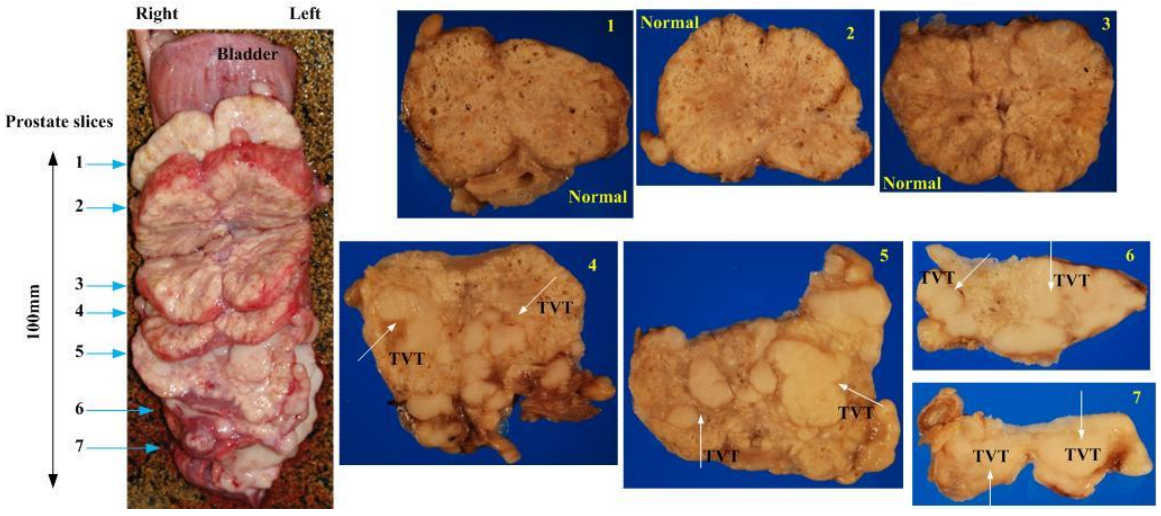

Figure 78 The 7 slices of the prostate gland were sectioned from cranial to caudal, at an interval of approximately 15mm.

The excised prostate (Fig 78) was approximately 10cm×5cm×5cm in size. The prostate was step-sectioned into approximately 1.5cm slices. The gross examination confirmed multiple coalescing foci of TVT in the caudal aspect of the gland, and significant infiltration of the tumor from the right to the left lobe.

The dog was humanely euthanized using a barbiturate overdose at 55-days post-inoculation followed by thorough gross inspection and excision of the prostate gland and urinary bladder. The prostate was serially sectioned by freehand technique in transverse planes. These planes were thought orthogonal to the quasi-sagittal planes used for transrectal US-coupled optical tomography. Routine histology with hematoxylin and eosin stain for light microscopy was performed on specimens selectively sampled from the sectioned prostate, each of which contained tissues that were grossly expected to be normal, cystic or neoplastic.

Retrospectively in this study, the lateral development of TVT was indicated earlier on NIR than on grey-scale US. The marked vascularity enhancement of the TVT seen on Doppler is primarily in the periphery of the hypo-echoic TVT foci, but the elevation of [HbT] on NIR was found almost always distributed in the entire indicated TVT region. This is an indication that the attenuation of NIR light is directly associated with [HbT]. The NIR imaging may therefore detect the onset of neo-vasculature before the size of the vessels be detectable on other noninvasive imaging techniques such as Doppler, providing earlier prediction of lateral and longitudinal changes.

CHAPTER VII

CONCLUSION

In summary, the TRUS coupled trans-rectal NIR sagittal imaging probe was fabricated. The CW optical measurement demonstrated the quantitative estimation of the optical absorption coefficient is feasible when incorporating the TRUS *a priori* information. The use of a condom is found to have minimum effects on NIR tomography measurement. Absorptive targets can also be recognized by optical stand-alone reconstruction which demonstrates the potential of finding targets ambiguous to US imaging.

In-vivo imaging of normal canine prostate and TVT tumors in the canine pelvic canal was performed by trans-rectal NIR tomography coupled with TRUS. The TVT tumor nodules were presented as hyper-absorption and hyper-scattering with respect to the normal prostatic and other pelvic tissues. Correlation of the TVT locations is found between trans-rectal NIR and TRUS images.

Dual-band *in-vivo* imaging of canine prostate with TVT tumors demonstrated a non-invasive optical measurement of [HbT] changes associated with tumor development. Using trans-rectal US-coupled spectral optical tomography the development and lateral involvement of the prostate cancer was detected earlier than using TRUS alone.

7.1 Contributions of this work

The most important contribution of this work is to demonstrate the *in-vivo* optical imaging of prostate by 3-stages of NIR/US development. It is the bridge to connect the NIR tomography with the non-invasive optical measurement of the prostate. The finding of the condom effect on light attenuation helps this imaging modality move on to future clinical study. The system calibration tests and *in-vivo* canine prostate measurements have demonstrated the potential to increase the specificity of prostate imaging by combining NIR optical and US measurement.

This work focuses on the instrumentation and experimental demonstration. It involves hardware part fabrication, optical alignment, system integration, data calibration and imaging reconstruction. The instrumentation part includes the micro-optics related tools designing and assembling, source coupling setup, programming of the system control by Labview and developing the codes for data calibration and imaging reconstruction with respect to the specific test. The experimental demonstration covers all the tests designed to quantify the system performance and validate the potential on the clinical application.

This work, to our knowledge, built the first combined endo-rectal NIR/US imaging applicator for prostate imaging. This integrated NIR/US prostate imaging platform which can be applied with those advanced techniques demonstrated on breast NIR imaging study such as frequency domain measurement or multiple-wavelength light to get further inclusions of the prostate optical properties. The dual-wavelength optical system is open to multiple wavelength measurement with minimum system changes. Future work is ongoing to validate the three-wavelength NIR imaging of mapping the

tissue oxygenation and perform *in-vivo* testing with TVT models developed in canine prostate.

7.2 Challenges in future studies

This work is an initial attempt to use the trans-rectal optical tomography in the prostate imaging field. A significant amount of work remains in order to apply this method in clinic such as required for the guidance in performing a biopsy.

First of all, an accurate prostate cancer model is required for furthering this research on the human prostate cancer study. On US all of the TVT tumor nodules developed in this subject were shown to be strongly hypo-echoic that correlated with the strongly hyper-absorptive and moderately hyper-scattering findings on NIR imaging. The feature of TVT as strongly absorptive on NIR tomography is likely due to the hyper-chromatic nuclei unique to TVT. The relatively higher scattering of the TVT may be due to the high density and larger nuclei of the neoplastic cells. As the neoplastic cells are arranged into microlobules by the pre-existing fibrovascular stroma, the TVT may also present certain polarization-sensitivity. Overall, the characteristic features of TVT on NIR tomography are comparable to those of angiogenesis that may be seen by NIR. Studies of microvessel density within the human prostate demonstrated a clear correlation of increased microvessel density with the presence of cancer. It is thereby a feasible expectation that the human prostate cancer may have notable contrast on trans-rectal NIR tomography. Most prostate cancers are presented as multi-focal. It must be noted that the intraprostatic TVT tumors were initiated in a non-immunosuppressed canine model in which the TVT nodules developed at multiple sites intra-prostatically and peri-prostatically. Although not all TVT tumors were confined to the prostate, successful

imaging of multiple TVT nodules by trans-rectal NIR tomography implies the utility of detecting multiple intra-prostatic tumors.

Secondly, there are several techniques demonstrated with great improvements that could be applied on this system to increase the reconstruction accuracy. As the discussion in section 4.3 states, incorporating the *a priori* spatial information can recover an accurate optical absorption and scattering value, while it needs the 3-D information from the US scanner in the clinical experiments. Other than that, a frequency-domain system can provide the phase information which helps to reconstruct the scattering values. It also can reduce the coupling issue of the reconstruction value between the absorption and scattering.

For measuring the [HbT], a multiple wavelength or broadband measurement could be applied to the system. For multiple wavelengths, the solution of the [HbO] and [Hb] becomes a multiple linear regression problem. As describe in Equ. 2, the absorption is a wavelength dependant function of different chromphores,

$$\begin{aligned}
\mu_a(\lambda_1) &= \varepsilon_1(\lambda_1)\cdot C_1 + \varepsilon_2(\lambda_1)\cdot C_2 + \cdots + \varepsilon_n(\lambda_n)\cdot C_n \\
\mu_a(\lambda_2) &= \varepsilon_1(\lambda_2)\cdot C_1 + \varepsilon_2(\lambda_2)\cdot C_2 + \cdots + \varepsilon_n(\lambda_2)\cdot C_n \\
&\vdots \\
\mu_a(\lambda_m) &= \varepsilon_1(\lambda_m)\cdot C_1 + \varepsilon_2(\lambda_m)\cdot C_2 + \cdots + \varepsilon_n(\lambda_m)\cdot C_n
\end{aligned} \qquad \text{Equation 46}$$

Equation 45 could be symbolized as:

$$[\mu_a] = [\varepsilon]\cdot[C] \qquad \text{Equation 47}$$

Where $[\mu_a]=\begin{bmatrix}\mu_a(\lambda_1)\\ \mu_a(\lambda_2)\\ \vdots\\ \mu_a(\lambda_m)\end{bmatrix}$ is m×1 vector which is obtained from m-wavelength measurement. And $[\varepsilon]=\begin{matrix}\varepsilon_1(\lambda_1) & \varepsilon_2(\lambda_1) & \cdots & \varepsilon_n(\lambda_1)\\ \varepsilon_1(\lambda_2) & \varepsilon_2(\lambda_2) & \cdots & \varepsilon_n(\lambda_2)\\ \vdots & \vdots & \ddots & \vdots\\ \varepsilon_1(\lambda_m) & \varepsilon_2(\lambda_m) & \cdots & \varepsilon_n(\lambda_m)\end{matrix}$ is m×n matrix corresponding to the molar absorption coefficients of n chromophores at m-wavelength measurements. $[C]=\begin{bmatrix}C_1\\ C_2\\ \vdots\\ C_n\end{bmatrix}$ is the molar concentration of n chromophores.

The solution of Equ. 46 can be obtained by ordinary least squares (OLS) which is commonly used to analyze the experimental or observational data.

$$[C]=\left([\varepsilon]'[\varepsilon]\right)^{-1}[\varepsilon]'[\mu_a] \qquad \text{Equation 48}$$

One more advantage to use multiple wavelength and broadband measurement is that the incorporation of the spectral *prior* reconstruction provide by NIRFAST. In spectral *prior* reconstruction, the elements in Jacobian matrix are derived by Equ. 28. In the iteration, the chromophore concentration, scattering power and amplitude are updated instead of previous absorption and scattering value in Equ. 28

$$\begin{bmatrix}\partial\Phi(\lambda_1)\\ \partial\Phi(\lambda_2)\\ \vdots\\ \partial\Phi(\lambda_m)\end{bmatrix}=\begin{bmatrix}J_{C1}(\lambda_1) & J_{C2}(\lambda_1) & J_{C3}(\lambda_1) & J_a(\lambda_1) & J_b(\lambda_1)\\ J_{C1}(\lambda_2) & J_{C2}(\lambda_2) & J_{C3}(\lambda_2) & J_a(\lambda_2) & J_b(\lambda_2)\\ & & & & \\ J_{C1}(\lambda_m) & J_{C2}(\lambda_m) & J_{C3}(\lambda_m) & J_a(\lambda_m) & J_b(\lambda_m)\end{bmatrix}\begin{bmatrix}\partial C_1\\ \partial C_2\\ \partial C_3\\ \partial a\\ \partial b\end{bmatrix} \qquad \text{Equation 49}$$

Where $J_C(\lambda) = J_{\mu_a} \otimes \left(\varepsilon_\lambda^{C_1,C_2,C_3}\right)$, $J_a(\lambda) = \left.\frac{\partial \Phi}{\partial a}\right|_\lambda = J_\kappa\left(-3\kappa^2\right)\lambda^{-b}$, and $J_b(\lambda) = \left.\frac{\partial \Phi}{\partial b}\right|_\lambda = J_\kappa\left(-3\kappa^2\right)\mu_s'(-\ln\lambda)$. J_{μ_a} and J_κ are the original Jacobian matrix elements described in Equ.28 $J_{\mu_a} = \frac{\partial \Phi}{\partial \mu_a}$ and $J_\kappa = \frac{\partial \Phi}{\partial \kappa}$.

Studies have shown the spectral *prior* reconstruction give more accurate reconstructed results and stable reconstruction than the stand-alone optical reconstruction.

Thirdly, the diffusion model based forward computation and iterative non-linear optimization of the image reconstruction of DOT is inevitably computationally expensive. Current image reconstruction of one wavelength data took about 10 minutes on a computer (Pentium 4, 3GHz, 2.5G RAM). Real-time optical image reconstruction is expected to apply this imaging modality to clinical exams. Recent work on the FEM solution to photon diffusion in biological tissue by implementing FPGA provides a potential to significant improve the reconstruction speed compared with current computer based image reconstruction.

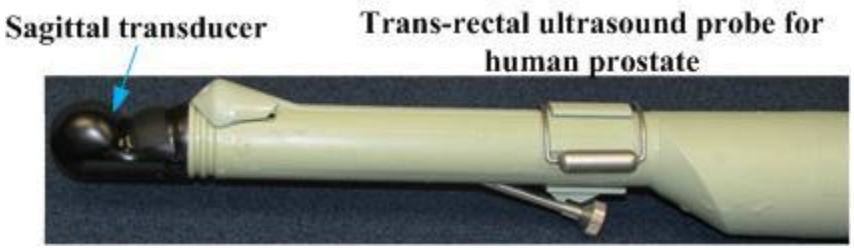

Figure 79 TRUS probe for human prostate imaging

Last but not least, human prostate imaging is more challenging than canine prostate imaging. The ultrasound probe (Fig. 79) for human prostate imaging has different shape to the canine prostate imaging probe which is difficult to concurrent with

optical imaging plane. The dimension of the combined human prostate imaging applicator is more restricted than canine prostate imaging. And with more optical channels incorporated in human prostate imaging, the dramatically increased dynamic range of the received signals will be difficult to detect. When all those techniques can be applied to this trans-rectal US/NIR optical imaging system, the overall system performance will be significantly improved.

REFERENCES

[1] Jemal A, Siegel R, Ward E, Hao YP, Xu JQ, Murray T, Thun MJ, "Cancer Statistics, 2008", CA Cancer J Clin 2008; 58: 71-96.

[2] American Cancer Society: Cancer Facts and Figures 2009. Link: http://www.cancer.org/downloads/STT/500809web.pdf.

[3] McNeal JE, Redwine EA, Freiha FS, Stamey TA, "Zonal distribution of prostatic adenocarcinoma. Correlaton with histologic pattern and direction of spread", Am J Surg Pathol 1988; 12: 897-906;

[4] Andreas Erbersdobler, Herbert Augustin, Thorsten Schlomm and Rolf-peter Henke, "Prostate cancers in the transition zone: Part1; pathological aspects", BJU, International, 94, 1221-1225, 2004.

[5] Herbert Augustin, Andereas Erbersdobler, Peter G. Hammerer, Markus Graefen and Hartwig Huland, "Prostate cancers in the transition zone: Part2; clinical aspects", BJU International, 94, 1226-1229, 2004.

[6] Ronald J. Cohen, Beverley A. Shannon, Michael Phillips, Rachael E. Moorin, Thomas M. Wheeler and Kerryn L. Garrett, "Central Zone Carcinoma of the prostate Gland: A Distinct Tumor Type With Poor Prognostic Features", The Journal of Urology, Vol. 179, 1762-1767, May 2008.

[7] Donald F. Gleason, George T. Mellinger and The veterans administration cooperative urological research group, "Prediction of prognosis for prostatic adenocarcinoma by combined histological grading and clinical staging", J Urol 111: 58-64, 1974.

[8] Gleason DF. Histologic grading and clinical staging of prostatic carcinoma. In: Tannenbaurn M, ed. Urologic Pathology: The prostate, Philadelphia: Lea & Febiger, 1977; 171.

[9] G. D. Grossfeld and P. R. Carroll, "Prostate cancer early detection: a clinical perspective," Epidemiol. Rev. 23, 173-80 (2001).

[10] Kisbor Mistry and Greg Cable, "Meta-Analysis of Porstate-Specific Antigen and Digital Rectal Examination as Screening Tests for Prostate Carcinoma", JABFP, Vol. 16, No.2, 2003.

[11] Ian M. Thompson, Donna Pauler Ankerst, Chen Chi, M. Scott Lucia, Phyllis J. Goodman, John J. Crowley, Howard L. Parnes, Charles A. Coltman, "Operating Characteristics of Prostate-Specific Antigen in Men with an Initial PSA Level of 3.0ng/ml or Lower", JAMA., 294: 66-70, 2005.

[12] Ian M. Thompson, Donna K. Pauler, Phyllis J. Goodman, Catherine M. Tangen, M. Scott Lucia, Howard L. Parnes, Lori M. Minasian, Leslie G. Ford, Scott M Lippman, E. David Crawford, John J. Crowley and Charles A. Coltman, "Prevalence of Prostate Cancer among Men with a Prostae-Specific Antigen level ≤ 4.0 ng per Milliliter", The New England Journal of Medicine, 350:22, 39-46, 2004.

[13] Aaron Caplan and Alexander Kratz, "Prsotate-Specific Antigen and Early Diagnosis of Prostate Cancer", Am J. Clin. Pathol. (Suppl. 1: S104-S108), 2002.

[14] C. R. Porter, "Does the number of prostate biopsies performed affect the nature of the cancer identified?", Nat. Clin. Pract. Urol. 4, 132-133 (2007).

[15] V. Scattoni, A. Zlotta, R. Montironi, C. Schulman, P. Rigatti, and F. Montorsi, "Extended and saturation prostatic biopsy in the diagnosis and characterisation of prostate cancer: a critical analysis of the literature," Eur. Urol. 52,1309-1322 (2007).

[16] Baris Turkbey, Peter A. Pinto and Peter L. Choyke, "Imaging techniques for prostate cancer: implications for focal therapy", Nature review, Urology, Vol. 6, 191-203, 2009.

[17] A. C. Loch, A. Bannowsky, L. Baeurle, B. Grabski, B. König, G. Flier, O. Schmitz-Krause, U. Paul, and T. Loch, "Technical and anatomical essentials for transrectal ultrasound of the prostate," World J. Urol.25, 361-366 (2007).

[18] Peter R. Carroll, Fergus V. Coakley and John Kurhanewicz, "Magnetic Resonance Imaging and Spectroscopy of Prostate Cancer", Rev Urol. 8(Suppl. 1: S4-S10), 2006.

[19] Elizabeth Henderson, Michael F Milosevic, Masoom A Haider and Ivan W T Yeung, "Functional CT imaging of prostate cancer", Phys. Med. Biol. 48 (3085-3100), 2003.

[20] Nobuyuki Oyama, Hironobu Akino, Hiroshi Kanamaru, Yuji Suzuki, Satoshi Muramoto, Yoshiharu Yonekura, Norihiro Sadato, Kazutaka Yamamoto and Kenichiro Okada, "^{11}C-Acetate PET Imaging of Prostate Cancer", J Nucl Med 2002, 43:181-186.

[21] Hodge KK, McNeal JE, Stamey TA, "Ultrasound guided transrectal core biopsies of the palpably abnormal prostate," J Urol.;142(1):66-70 (1989).

[22] Garber SJ, Goldenberg SL, Cooperberg PL, Wong AD, Bilby JH, Mathieson JR, "Systematic transrectal ultrasound-guided biopsy of the prostate," Can Assoc Radiol J.; 45(5):387-90 (1994).

[23] K. Shinohara, T. M. Wheeler, and P. T. Scardino, "The appearance of prostate cancer on trans-rectal ultrasonography: correlation of imaging and pathological examinations," J. Urol. 142, 76-82 (1989).

[24] Ellis WJ, Brawer MK, "The significance of isoechoic prostate carcinoma," J. Urol,; 152: 2304-2307 (1994).

[25] B. Spajic, H. Eupic, D. Tomas, G. Stimac, B. Kruslin, and O. Kraus, "The incidence of hyperechoic prostate cancer in trans-rectal ultrasound-guided biopsy specimens," Urology 70, 734-737 (2007).

[26] Downs TM, Grossfield GD, Shinohara K, Carroll PR, "Transrectal ultrasound-guided prostate biopsy," in Image-Guided Diagnosis and Treatment of Cancer, edited by D'Amico AV, Loefler JS, Harris JR,Human Press, 2003.

[27] Newman JS, Bree RL, Rubin JM, "Prostate cancer: diagnosis with color Doppler sonography with histologic correlation of each biopsy site," Radiology; 195(1):86-90 (1995).

[28] Edmund Louvar, Peter J. Littrup, Albert Goldstein, Lelia Yu, Wael Sakr and David Grignon, "Correlation of Color Doppler Flow in the Prostate with Tissue Microvascularity", Cancer, Vol. 83, No.1, July 1, 1998.

[29] Wise AM, Stamey TA, McNeal JE, and Clayton JL, "Morphologic and clinical significance of multifocal prostate cancers in radical prostatectomy specimens," Urology 60, 264-9 (2002).

[30] Mouraviev V, Mayes JM, Madden JF, Sun L, Polascik TJ, "Analysis of laterality and percentage of tumor involvement in 1386 prostatectomized specimens for selection of unilateral focal cryotherapy," Technol Cancer Res Treat, 2007.

[31] M. A. Franceschini, K. T. Moesta, S. Fantini, G. Gaida, E. Gratton, H. Jess, W. W. Mantulin, M. Seeber, P. M. Schlag, and M. Kaschke, "Frequency-domain techniques enhance optical mammography: initial clinical results," Proc. Nat. Acad. Sci. USA 94, 6468-6473 (1997).

[32] B. Tromberg, J. Coquoz, O. Fishkin, J. B. Pham, T. Anderson, E. R. Butler, J. Cahn, M. Gross, J. D.Venugopalan, and D. Pham, "Non-invasive measurements of breast tissue optical properties using frequency-domain photon migration," Phil. Trans. R. Soc. Lond. B 352, 661-668 (1997).

[33] B. W. Pogue, S. P. Poplack, T. O. McBride, W. A. Wells, K. S. Osterman, U. L. Osterberg, and K. D.Paulsen," Quantitative hemoglobin tomography with diffuse near-infrared spectroscopy: pilot results in the breast," Radiology 218, 261-266 (2001).

[34] V. Ntziachristos and B. Chance, "Probing physiology and molecular function using optical imaging: applications to breast cancer," Breast Cancer Res. 3, 41-46 (2001).

[35] Q. Zhu, E. B. Cronin, A. A. Currier, H. S. Vine, M. Huang, N. Chen, and C. Xu, "Benign versus malignant breast masses: optical differentiation with US-guided optical imaging reconstruction," Radiology 237, 57-66 (2005).

[36] B. J. Tromberg, B. W. Pogue, K. D. Paulsen, A. G. Yodh, D. A. Boas, and A. E. Cerussi, "Assessing the future of diffuse optical imaging technologies for breast cancer management," Med Phys. 35, 2443-51 (2008).

[37] Piao D, Jiang Z, Xu, G, Musgrove CH, Bunting CF, "Approach on trans-rectal optical tomography probing for the imaging of prostate with trans-rectal ultrasound correlation", International Symposium on Biomedical Optics, San Jose, CA, Jan. 19-24, 2008. Proceedings of SPIE, Vol. 6850, Paper #68500E (pages: 1-14)

[38] Douglas E. Johnson, Douglas M. Cromeens and Roger E. Price, "Interstitial laser prostatectomy", SPIE Vol. 2129, lasers in Urology 1994/67.

[39] C. Li, R. Liengsawangwong, H. Choi, and R. Cheung , "Using *a priori* structural information from magnetic resonance imaging to investigate the feasibility of prostate diffuse optical tomography and spectroscopy: a simulation study," Med. Phys. 34, 266-274 (2007).

[40] M. Cutler, "Transillumination as an aid in the diagnosis of breast lesions," Surg. Gyn. Obst. 48, 721-729 (1929).

[41] F. F. Jobsis, "Non-invasive, infra-red monitoring of cerebral and myochardial oxygen sufficiency and circulatory parameters," Science 198, 1264-1267 (1977).

[42] Troy O. McBride, "Spectroscopic Reconstructed Near Infrared Tomographic Imaging for Breast Cancer Diagnosis", Thesis, 2001.

[43] S. Fantini, S. A. Walker, M. A. Franceschini, M. Kaschke, P. M. Schlag, and K. T.Moesta, "Assessment of the size, position, and optical properties of breast tumors *in-vivo* by noninvasive optical methods," Appl. Opt. 37, 1982-89 (1998).

[44] T. O. McBride, B. W. Pogue, E. Gerety, S. Poplack, U. L. Osterberg, and K. D. Paulsen, "Spectroscopic diffuse optical tomography for quantitatively assessing hemoglobin concentration and oxygenation in tissue," Appl. Opt. 38, 5480-90 (1999).

[45] David A. Boas, Dana H. Brooks, Eric L. Miller, Charles A. DiMarzio, Misha Kilmer, Richard J. Gaudette and Quan Zhang, "Imaging the body with Diffuse Optical Tomography", IEEE Signal Processing Magazine, 1053-5888/01, Nov. 2001.

[46] Veronica S. Hollis, "Non-Invasive Monitoring of Brain Tissue Temperature by Near-Infrared Spectroscopy", Thesis, Department of Medical Physics and Bioengineering, University College London, 2002.

[47] Iyad S. Saidi, Steven L. Jacques, and Frank K. Tittel, "Mie and Rayleigh modeling of visible-light scattering in neonatal skin", Applied optics, Vol. 34, No. 31, November 1995.

[48] Michael Solonenko, Rex Cheung, Theresa M Busch, Alex Kachur, Gregory M Griffin, Theodore Vulcan, Timothy C Zhu, Hsing-Wen Wang, Stephen M Hahn and A G Yodh, "In vivo reflectance measurement of optical properties, blood oxygenation and motexafin lutetium uptake in canine large bowels, kidneys and prostates", Phys. Med. Biol. 47 (2002) 857-873.

[49] Srinivasan, S., Pogue, B.W., Carpenter C., Jiang, S., Wells, W.A., Poplack, S.P., Kaufman P.A. and Paulsen, K.D., "Developments in Quantitative Oxygen-Saturation Imaging of Breast Tissue *In-vivo* Using Multispectral Near-Infrared Tomography", Antioxidants & Redox Signaling, 9(8): 1143-56 (2007).

[50] T. Svensson, E. Alerstam,M. Einarsd´ott´ır,K. Svanberg, and S. Andersson-Engels, "Towards accurate *in-vivo* spectroscopy of the human prostate," J. Biophoton., vol. 1, pp. 200–203, 2008.

[51] L. V. Wang and Hi.-I Wu, "Biomedical Optics: Principles and Imaging", Wiley, 2007.

[52] D. T. Delpy, M. Cope, P. van der Zee, S. Arridge, Susan Wray and J. Wyatt, "Estimation of optical pahtlength through tissue form direct time of flight measurement", Phys. Med. Biol. Vol.33, No. 12, 1433-1442, 1988.

[53] S R Arridge, "Topical review: Optical tomography in medical imaging", Inverse Problems 15, R41-R93, 1999.

[54] A. P. Gibson, J. C. Hebden and S. R. Arridge, "Recent advances in diffuse optical imaging", Topical review, Phys Med. Biol. 50, R1-R43, 2005.

[55] H. Dehghani, M. E. Eames, P. K. Yalavarthy, S.C. Davis, S.Srinivasan, C. M. Carpenter, B.W. Pogue and K. D. Paulsen, "Near infrared optical tomography using NIRFAST: Algorithm for numerical model and image reconstruction", Commun. Numer. Meth. Engng (2008).

[56] Heng Xu, “MRI-coupled Broadband Near-infrared tomography for Small Animal Brain Studies”, Thesis, Thayer School of Engineering, Dartmouth College, 2005.

[57] M. S. Patterson, Chance B., Wilson, B. C., "Time resolved reflectance and transmittances for the non-invasive measurement of tissue optical properties," Appl. Opt. 28, 2331-2336 (1989).

[58] B. Chance, Nioka, S., Kent, J., McCully, K., Fountain, M., Greenfield, R., Holtom, G., "Time-resolved spectroscopy of hemoglobin and myoglobin in resting and ischemic muscle," Analy. Biochem. 174, 698-707 (1988).

[59] M. S. Patterson, Moulton, J. D., Wilson, B. C., Berndt, K. W., Lakowicz, J. R., "Frequency-domain reflectance for the determination of the scattering and absorption properties of tissue," Appl. Opt. 30, 4474-4476 (1991).

[60] J. Fishkin, Gratton, E., van de Ven, M. J., Mantulin, W. W., "Diffusion of intensity modulated near infrared light in turbid media," Proc. SPIE 1431, 122-135 (1991).

[61] X. Zhou and T. C. Zhu, "Image reconstruction of continuous wave diffuse optical tomography (DOT) of human prostate," in Proc. the COMSOL Users Conference (2006) .

[62] D. Piao, H. Xie. W. Zhang, J. S. Kransinski, G. Zhang, H. Dehghani, and B. W. Pogue, “Endoscopic, rapid near-infrared optical tomography,” Opt. Lett. 31, 2876-2878 (2006).

[63] N. Iftimia and H. Jiang, “Quantitative optical image reconstruction of turbid media by use of direct-current measurements,” Appl. Opt. 39, 5256-5261 (2000).

[64] Z. Yuan, Q. Zhang, E. Sobel, and H. Jiang, “Three-dimensional diffuse optical tomography of osteoarthritis: initial results in the finger joints,” J. Biomed. Opt. 12, 034001 (2007).

[65] Y. Xu, X.Gu, T. Khan and H. Jiang, “Absorption and scattering images of heterogeneous scattering media can be simultaneously reconstructed by use of dc data”, Applied Optics, Vol.41, No.25, Sep. 1, 2002.

[66] Xu G, Piao D, Musgrove CH, Bunting CF, Dehghani H, “Trans-rectal ultrasound-coupled near-infrared optical tomography of the prostate Part I: Simulation,” Optics Express, Vol. 16, Iss. 22, pp. 17484–17504 (2008).

[67] Zhang A, Piao D, Bunting CF, Pogue BW, “Photon diffusion in a homogeneous medium bounded externally or internally by an infinitely long circular cylindrical applicator ---- Part I: steady-state theory,” Journal of Optical Society of America, A, Vol. 27, No. 3, pp. 648-662 (2010).

[68] McPhee MS, Thorndyke CW, Thomas G, et al.: Interstitial applications of laser irradiation in hematoporphyrin derivative-photosensitized Dunning R3327 prostate cancers. Lasers Surg Med 1984, 4:93–98.

[69] Camps JL Jr, Powers SK, Beckman WC Jr, et al.: Photodynamictherapy of prostate cancer: an in vitro study. J Urol 1985, 134:1222–1226.

[70] S. L. Jacques and M. Motamedi, "Tomographic needles and catheters for optical imaging of prostatic cancer," Proc. SPIE 2395, 111-118 (1995).

[71] T. Svensson, S. Andersson-Engels, M. Einarsdóttír, and K. Svanberg, "*In-vivo* optical characterization of human prostate tissue using near-infrared time-resolved spectroscopy," J. Biomed. Opt. 12, 014022 (2007).

[72] Piao D, Bartels KE, Jiang Z, Holyoak GR, Ritchey JW, Xu G, Bunting CF, Slobodov G, "Alternative trans-rectal prostate imaging: A diffuse optical tomography method," IEEE Journal of Selected Topics in Quantum Electronics, "Biophotonics 2" Special Issue.

[73] L. K. Lee, C. Whitehurst,M. L. Pantelides, and J.V. Moore, "An interstitial light assembly for photodynamic therapy in prostatic carcinoma," BJU. Int., vol. 84, no. 7, pp. 821–826, 1999.

[74] M. L. Pantelides, C.Whitehurst, J. V. Moore, T. A. King, and N. J. Blacklock, "Photodynamic therapy for localized prostatic cancer—Light penetration in the human prostate gland," J. Urol. (Baltimore), vol. 143, no. 2, pp. 398–401, 1990.

[75] C. Whitehurst, M. L. Pantelides, J. V. Moore, P. J. C. Brooman, and N. J. Blacklock, "*In-vivo* laser-light distribution in human prostaticcarcinoma," J. Urol. (Baltimore), vol. 151, no. 5, pp. 1411–1415, 1994.

[76] L. K. Lee, C. Whitehurst, M. L. Pantelides, and J. V. Moore, "In situ comparison of 665 nm and 633 nm wavelength light penetration in the human prostate gland," Photochem. Photobiol., vol. 62, no. 5, pp. 882–886, 1995.

[77] Wei, H., Xing D., He, B., Wu, R., Gu. H., Wu G., Chen, X., "Absorption and Scattering Characteristics of Human Benign Prostatic Hyperplasia Tissue with Ti: Sapphire Laser Irradiation in Vitro", Spectroscopy and Spectral analysis (China), Vol. 29, No.1, pp10-13, 2008.

[78] T. C. Zhu, A. Dimofte, J. C. Finlay, D. Stripp, T. Busch, J. Miles, R.Whittington, S. B. Malkowicz, Z. Tochner, E. Glatstein, and S. M. Hahn, "Optical properties of human prostate at 732 nm measured in mediated photodynamic therapy," Photochem. Photobiol., vol. 81, no. 1, pp. 96–105, 2005.

[79] T. C. Zhu, J. C. Finlay, and S. M. Hahn, "Determination of the distribution of light, optical properties, drug concentration, and tissue oxygenation *in-vivo* in human prostate during motexafin lutetiummediated photodynamic therapy," J. Photochem. Photobiol. B, vol. 79, no. 3, pp. 231–241, 2005.

[80] J. Li and T. C. Zhu, "Determination of *in-vivo* light fluence distribution in a heterogeneous prostate during photodynamic therapy," Phys. Med. Biol., vol. 53, no. 8, pp. 2103–2114, Apr. 2008.

[81] K. K. Wang and T. C. Zhu, "Reconstruction of *in-vivo* optical properties for human prostate using interstitial diffuse optical tomography," Opt. Exp., vol. 17, no. 14, pp. 11665–11672, 2009.

[82] R. A. Weersink, A. Bogaards, M. Gertner, S. R. H. Davidson, K. Zhang, G. Netchev, J. Trachtenberg, and B. C. Wilson, "Techniques for delivery and monitoring of TOOKAD _WST09_-mediated photodynamic therapy of the prostate: Clinical experience and practicalities," J. Photochem. Photobiol. B, vol. 79, no. 3, pp. 211–222, 2005.

[83] M. Essenpreis, "Thermally induced changes in optical properties of biological tissues," Ph.D. thesis, Univ. College London, London, 1992.

[84] A. Roggan, K. D¨orschel, O. Minet, D.Wolff, and G.M¨uller, "The optical properties of biological tissue in the near infrared wavelength range—review and measurements," in Laser-induced Interstitial Thermotherapy Thermotherapy, G. M¨uller and A. Roggan, Eds.:Washington: SPIE Optical Engineering Press, 1995, pp. 10–44.

[85] Dheerendra Kashyap, Disha Peswani, Jeffrey Cadeddu and Hanli Liu, "Steady-state reflectance spectroscopy used to quantify hemodynamic and optical properties of tissue: Demonstration of heterogeneities of human prostrates", BIOMED, BSuE80, 2008.

[86] Franceschini, M. A., Joseph, D. K., Huppert, T. J., Diamond, S. G. and Boas, D. A. (2006). "Diffuse optical imaging of the whole head." Journal Biomed Optics 11(5): 054007.

[87] Gultekin Gulsen, Bin Xiong, Ozlem Birgul and Orhan Nalcioglu, "Design and implementation of a multifrequency near-infrared diffuse optical tomography system", Journal of Biomedical Optics, Vol. 11(1), 2006.

[88] T. O. Mcbride, B. W. Pogue, S. Jiang, U. L. Osterberg, K. D. Paulsen, "A parallel-detection frequency-domain near-infrared tomography system for hemoglobin imaging of the breast *in-vivo*", Rev. Sci. Instrum., volume 72, 2001.

[89] Chen, NG, Huang, MM, Xia, HJ, Piao, DQ, Cronin, E, Zhu, Q., "Potable near infrared diffusive light imager for breast cancer detection," Journal of Biomedical Optics, MAY/JUNE ISSUE, 504-510, 2004.

[90] Jiang Z, Xu G, Elgawadi A, Piao D, "Development of a trans-rectal optical tomography probe for concurrent sagittal imaging with trans-rectal ultrasound", OSA Biomedical Topical Meetings, St. Petersburg, FL. March 16-19, 2008.

[91] Jiang Z, Piao D, Xu G, Ritchey JW, Holyoak GR, Bartels KE, Bunting CF, Slobodov G, Krasinski JS, "Trans-rectal ultrasound-coupled near-infrared optical tomography of the prostate Part II: Experimental demonstration," Optics Express, Vol. 16, Iss. 22, pp. 17505–17520 (2008).

[92] Piao D, Xie H. Zhang W, Kransinski JS, Zhang G, Dehghani H, and Pogue BW, "Endoscopic, rapid near-infrared optical tomography", Optics Letters, Vol. 31, No. 19, Oct. 2006, pp. 2876-2878.

[93] Piao D, Dehghani H, Jiang S, Srinivasan S, and Pogue BW, "Instrumentation for video-rate near-infrared diffuse optical tomography", Review of Scientific Instruments, Vol. 76, No. 12, Dec. 2005, pp. 124301-124301-13.

[94] Piao D, Jiang S, Srinivasan S, Dehghani H, and Pogue BW, "Video-rate near-infrared optical tomography using spectrally-encoded parallel light delivery", Optics Letters, Vol. 30, No. 19, Oct. 2005, pp. 2593-2595.

[95] M. J. Holboke, B. J. Tromberg, X. Li, N. Shah, J. Fishkin, D. Kidney, J. Butler, B. Chance, and A. G.Yodh, "Three-dimensional diffuse optical mammography with ultrasound localization in a human subject," J. Biomed Opt. 5, 237-247 (2000).

[96] M. Guven, B. Yazici, X. Intes, and B. Chance, "Diffuse optical tomography with *a priori* anatomical information," Phys. Med. Biol. 50, 2837-58 (2005).

[97] H. Dehghani, C. M. Carpenter, P. K. Yalavarthy, B. W. Pogue, and J. P. Culver, "Structural *a priori* information in near-infrared optical tomography," Proc. SPIE 6431, 64310B1-7 (2007).

[98] Musgrove, C., Bunting, C.F., Dehghani, H., Pogue, B.W. and Piao, D., "Computational Aspects of Endoscopic (Trans-rectal) Near-infrared Optical Tomography: Initial Investigations", Proc. SPIE, 6434, 643409 (2007).

[99] Hao Xie, "Dual-spectral endoscopic near-infrared optical tomography for assessment of Hemoglobin concentration and oxygen saturation", Thesis, Oklahoma State University, 2008.

[100] S. Arridge, M. Cope, and D. Delpy, "The theoretical basis for the determination of optical path-length in tissue: temporal and frequency analysis," Phys. Med. Biol. Vol. 37, No 7, 1531-1560 (1992).

[101] R. C. Haskell, L. O. Svaasand, T. T. Tsay, T. C. Feng, M. S. McAdams, B. J. Tromberg, "Boundary conditions for the diffusion equation in radiative transfer," J. Opt. Soc. Am. A. 11, 2727-41 (1994).

[102] R. Aronson, "Boundary conditions for diffusion of light," J. Opt. Soc. Am. A. 12, 2532-9 (1995).

[103] A. H. Hielscher, R. E. Alcouffe, and R. L. Barbour, "Comparison of finite-difference transport and diffusion calculations for photon migration in homogeneous and heterogeneous tissues," Phys. Med. Biol. 43, 1285-302 (1998).

[104] Wai-Fung Cheong, Scott A. Prahl and Ashley J. Welch, "A review of the Optical Properties of Biological Tissues", IEEE Journal of Quantum Electronics, Vol. 26, No.12, Dec. 1990.

[105] B. Rivera, K. Ahrar, M.M. Kangasniemi, J.D. Hazle and R.E. Price, "Canine Transmissible Venereal Tumor: A Large-Animal Transplantable Tumor Model", Comparative Medicine, Vol. 55, No. 4, Aug 2005.

[106] Piao D, Jiang Z, Bartels KE, Holyoak GR, Ritchey JW, Xu G, Bunting CF, Slobodov G, "*In-vivo* trans-rectal ultrasound-coupled near-infrared optical tomography of intact normal canine prostate," Journal of Innovative Optical Health Sciences, Vol. 2, No. 3, pp. 215-225 (2009).

[107] Jiang Z, Holyoak GR, Bartels KE, Ritchey JW, Xu G, Bunting CF, Slobodov G, Piao D, "*In-vivo* trans-rectal ultrasound coupled near-infrared optical tomography of a transmissible venereal tumor model in the canine pelvic canal," Journal of Biomedical Optics Letters, Vol. 14, No. 3, pp. 030506, May/June, 2009.

[108] R. Choe, A. Corlu, K. Lee, T. Durduran, S. D. Konecky, M. Grosicka-Koptyra, S. R. Arridge, B. J. Czerniecki, D. L. Fraker, A. DeMichele, B. Chance, M. A. Rosen, and A. G. Yodh, "Diffuse optical tomography of breast cancer during neoadjuvant chemotherapy: a case study with comparison to MRI," Med. Phys. 32, 1128-1139 (2005).

[109] Jiang Z, Ritchey JW, Holyoak GR, Bartels KE, Xu G, Bunting CF, Slobodov G, Krasinski JS, Piao D, "*In-vivo* trans-rectal ultrasound coupled trans-rectal near-infrared optical tomography of canine prostate bearing transmissible venereal tumor," International Symposium on Biomedical Optics, San Jose, CA, Jan. 24-29, 2009. Proceedings of SPIE, Vol. 7174, Paper #71741U.

[110] Newman JS, Bree RL, Rubin JM, "Prostate cancer: diagnosis with color Doppler sonography with histologic correlation of each biopsy site," Radiology; 195(1):86-90 (1995).

[111] Bigler SA, Deering RE, Brawer MK, "Comparison of microscopic vascularity in benign and malignant prostate tissue," Hum Pathol. 1993 Feb;24(2):220-6.

[112] Cosgrove D, "Angiogenesis imaging—ultrasound," Br J Radiol. 2003;76 Spec No 1:S43-9. Review.

[113] Halpern JE, "Color and power Doppler evaluation of prostate cancer," in Imaging of the Prostate, edited by Halpern RJ, Cochlin DL, Goldberg BB, Martin Dunitz, 2002.

[114] Chance B., Nika S., Zhang J., Conant E.F., Hwang E., Briest S., Orel S.G., Schnall M.D., and Czerniecki B.J., "Breast cancer detection based on incremental biochemical and physiological properties of breast cancers: a six-year, two-site study", Acad Radiol., 12: 925-933 (2005).

[115] Vollmer, R.T., Kantoff, P.W., Dawson, N.A. and Vogelzang, N.J., "Importance of Serum Hemoglobin in Hormone Refractory Prostate Cancer", Clinical Cancer Research, 8: 1049-1053 (2002).

[116] Yu, G., Durduran, T., Zhou, C., Zhu, T.C., Finlay, J.C., Busch, T.M., Malkowicz, S.B., Hahn, S.M. and Yodh, A.G., "Real-time In situ Monitoring of Human Prostate Photodynamic Therapy with Diffuse Light", Photochemistry and Photobiology, 82: 1279-1284 (2006).

[117] Beer, T.M., Tangen, C.M., Bland, L.B., Hussain, M., Goldman, B.H., DeLoughery, T.G. and Crawford, E.D., "The prognostic value of Hemoglobin change after initiating Androgen-Deprivation therapy for newly diagnosed metastatic prostate cancer", Cancer, 107(3):489-96 (2006).

[118] Jiang Z, Piao D, Krasinski JS, "Development of a continuous-wave dual-band trans-rectal optical tomography system for concurrent sagittal imaging with trans-rectal ultrasound," International Symposium on Biomedical Optics, San Jose, CA, Jan. 24-29, 2009. Proceedings of SPIE, Vol. 7171, Paper #71710G.

[119] McCay CM, "The hemoglobin and total phosphorus in the blood of cows and bulls," J. Dairy Sei., 14 (4): 373-378 (1931).

[120] Hayes MD, Vanzant ES, Stombaugh TS, Gates RS, "Comparison of bovine blood absorption coefficients to human curves," Livestock Environment VIII, Proceedings, 981-985 (2008).

[121] Karen B. and Atle B., "Accurate de-oxygenation of *ex vivo* whole blood using sodium dithionite", Proc. Intl. Soc. Mag. Reson. Med. 8 (2000).

[122] Justin Rajesh Rajian, Paul L. Carson and Xueding Wang, "Quantitative photo-acoustic measurement of tissue optical absorption spectrum aided by an optical contrast agent", Optical Express 2009, March 16; 17(6): 4879-4889.

APPPENDICES

A.1 Measured absorption value of intralipid with different ink concentration

For 1% and 0.2% intralipid, each solution was prepared 0.1% (ink/intralipid) solution (Pelikan Schwarz – black) and measured by spectrophotometer. That is:

$$0.1\%\,(\text{ink/intralipid})\,\text{solution} = \frac{0.5ml\ (\text{pure ink})}{499.5\text{intralipid}\,(1\%\,\text{or}\,0.2\%) + 0.5\text{ml}\,(\text{pure ink})}$$

After that, prepared 150ml 1% intralipid and 150ml 0.2% intralipid, added with the 0.1% ink/intralipid solution to increase the absorption.

Table 10 Absorption value of 1% intralipid (cm^{-1}) 150ml

0.1%ink	650nm	705nm	750nm	785nm	808nm
0	-0.001	0	0	-0.001	-0.001
1ml	0.077	0.067	0.058	0.053	0.051
2ml	0.172	0.152	0.135	0.125	0.12
3ml	0.224	0.195	0.172	0.158	0.151
4ml	0.292	0.256	0.226	0.209	0.199
5ml	0.348	0.306	0.27	0.249	0.238
6ml	0.406	0.358	0.316	0.292	0.279

Table 11 Absorption value of 0.2% intralipid (cm^{-1}) 150ml

0.1%ink	650nm	705nm	750nm	785nm	808nm
0	-0.001	0.001	0.003	0.002	0.002
1ml	0.027	0.025	0.024	0.023	0.022
2ml	0.055	0.050	0.046	0.043	0.041
3ml	0.084	0.075	0.068	0.063	0.060
4ml	0.11	0.097	0.088	0.082	0.078
5ml	0.135	0.12	0.108	0.099	0.094
6ml	0.16	0.141	0.126	0.115	0.110

A.2 Pin definition of TCLDM9 and LDR

Table 12 Pin definition of TCLDM9 Laser diode driver

Pin	Signal	Description
1	Interlock and Status Pin (LDC Specific)	This pin is the input to the LD Status Indicator and Interlock Circuits. When using Thorlabs LDCs no external circuitry is required. To use these features with third-party controllers please refer to the Status and Interlock section of this manual.
5	Interlock and Status Return	This pin is the return side of the Status and Interlock circuitry.
7	Laser Diode Cathode	This pin is connected to the 3 o'clock pin on the laser socket when the LD Polarity Switch is set to AG (Anode Grounded). Otherwise it is floating.
8	Laser Diode Anode	This pin is connected to the 3 o'clock pin on the laser socket when the LD Polarity Switch is set to CG (Cathode Grounded). Otherwise it is floating.
3	Laser Ground (Case)	This pin is connected to the 12 o'clock and 6 o'clock pins on the laser socket and corresponds to the settings of the LD and PD polarity switches. i.e. If the LD and PD switches are set to AG then this pin grounds the Anodes of the laser and photo diodes.
2	Photodiode Cathode	This pin is connected to the 9 o'clock pin on the laser socket when the PD Polarity Switch is set to AG (Anode Grounded). It is attached to ground and the 12 o'clock and 6 o'clock pins on the laser socket when the PD Polarity Switch is set to CG (Cathode Grounded).
4	Photodiode Anode	This pin is connected to the 9 o'clock pin on the laser socket when the PD Polarity Switch is set to CG (Cathode Grounded). It is attached to ground and the 12 o'clock and 6 o'clock pins on the laser socket when the PD Polarity Switch is set to AG (Anode Grounded).
6	Laser Diode Voltage (Cathode)	This pin is connected to LD Interface Pin 7, thru a 499 Ohm resistor, when the LD Polarity Switch is set to AG (Anode Grounded). It is attached directly to LD Interface Pin 3 when the LD Polarity Switch is set to CG (Cathode Grounded).
9	Laser Diode Voltage (Anode)	This pin is connected to LD Interface Pin 8, thru a 499 Ohm resistor, when the LD Polarity Switch is set to CG (Cathode Grounded). It is attached directly to LD Interface Pin 3 when the LD Polarity Switch is set to AG (Anode Grounded).

Table 13 Pin definition of TCLDM9 Laser temperature controller

Pin	Signal	Description
4	+TEC	This pin is connected to the positive terminal of the TEC element.
5	-TEC and TEC Lockout (-)	This pin is connected to the negative terminal of the TEC element, and also is common to the cathode of the photo-relay of the TEC Lockout circuit - refer to the Status and Interlock section of this manual.
1	TEC Lockout (+)	This pin is connected to the anode of the photo-relay side of the TEC Lockout circuit. When using Thorlabs TEDs no external circuitry is required. To use these features with third-party controllers please refer to the Status and Interlock section of this manual.
2	+Thermistor	The 10KΩ @ 25°C NTC thermistor (provided for temperature feedback).
3	-Thermistor	The thermistor return pin.
7	AD592(-)	The negative terminal of the AD592 temperature transducer. When using Thorlabs TEDs no external circuitry is required. To use this device with third party controllers it must be properly biased. Refer to Analog Devices AD592 Data for application information.
9	AD592(+)	The positive terminal of the AD592
6	n.c.	
8	n.c.	

The rear panel connectors of LD driver and TEC are shown in Fig. 79. The LD driver connector pins are regularly defined. In order for the laser output to be enabled, a short must exist between the Inter lock pins (1, 2) of the connector. The short can be a direct short across the pins or a switch to prevent laser operation until the switch is closed. Otherwise, the Interlock LED illuminates on the front panel and the laser output is disabled. For TEC connector, Pins 1 and 2, 3 and 4 are connected together in pairs internally to allow high current flow to the TEC module. Pins 7 and 8 are connected to the sensor. Pins 9 through 15 (Right side pins), which are designed for use with an external TE Booster, are normally not used.

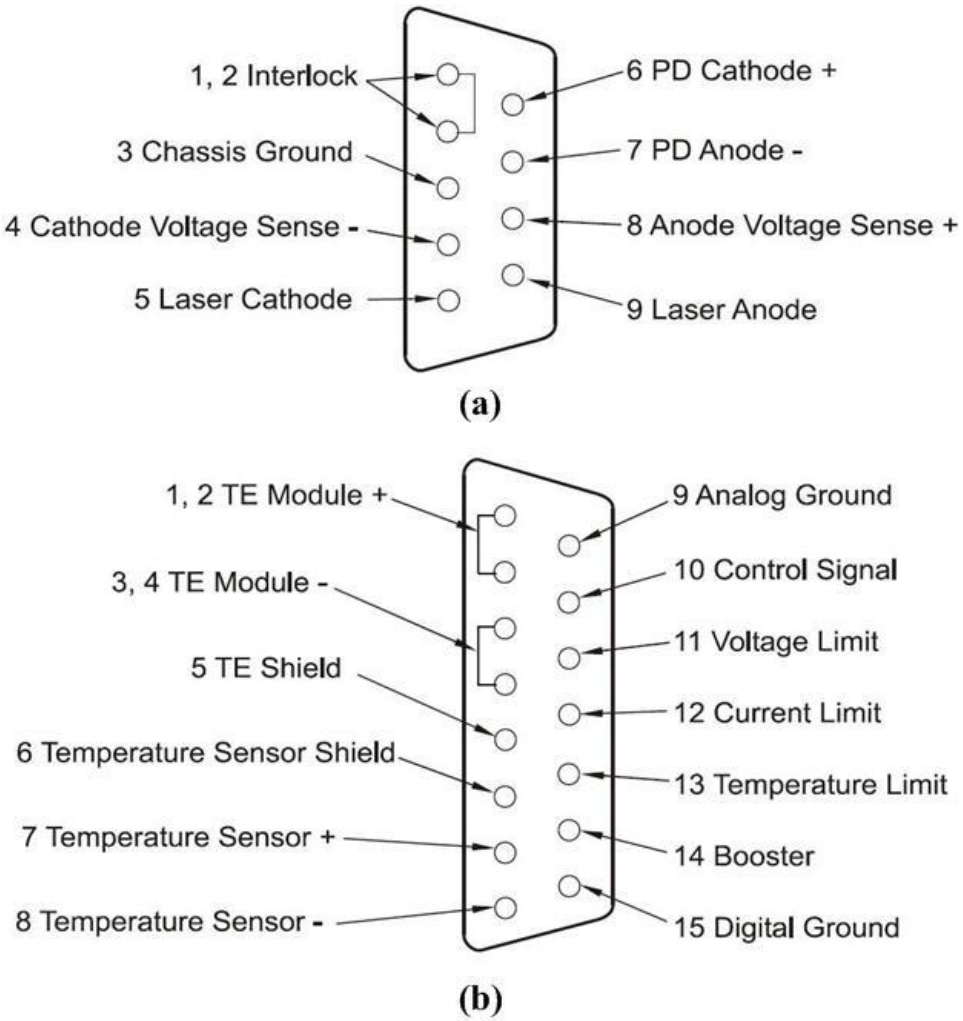

Figure 80 Rear panel connector of LDC-3722B

The connections between the LD drivers and TEC drivers are shown in Fig. 80 and Fig. 81.

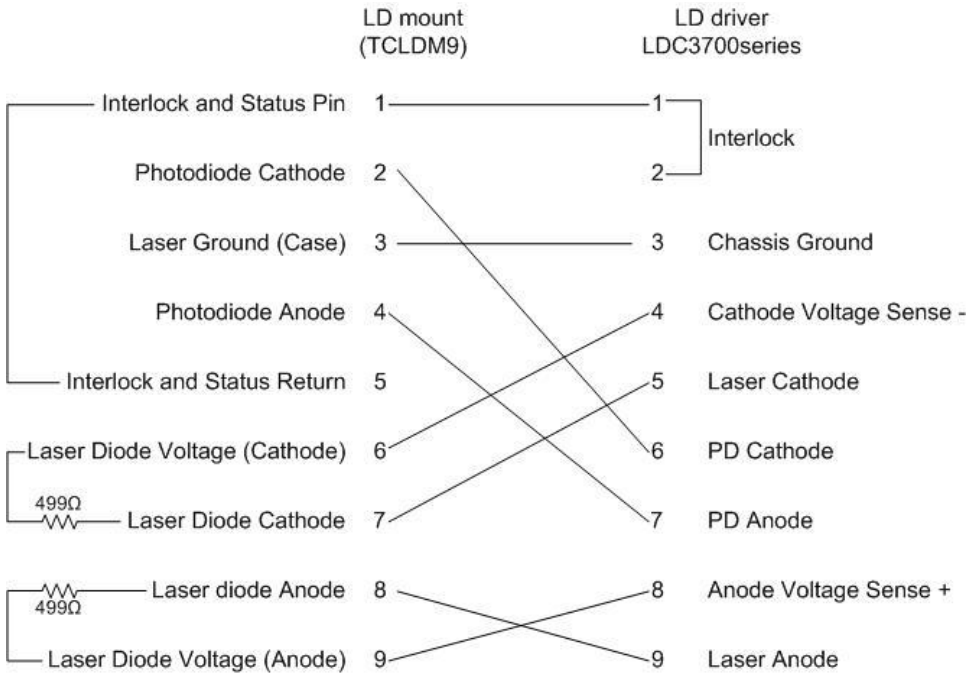

Figure 81 Connection between the LD drivers

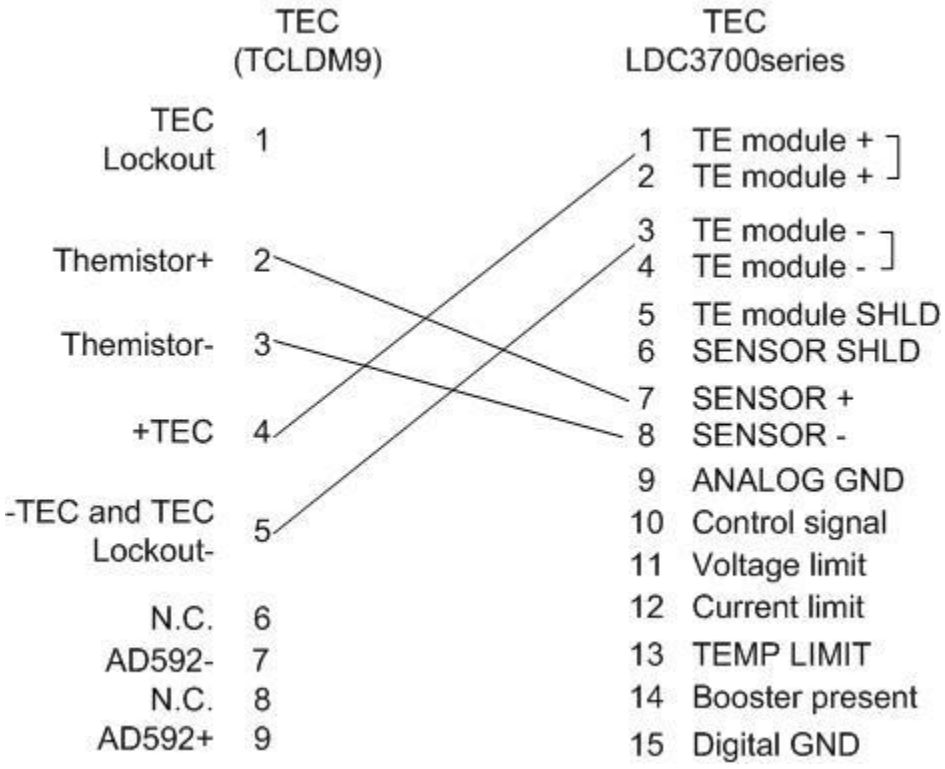

Figure 82 Connection between the TEC drivers

A.3 Matlab codes

Spectral-encoded system CCD image data calibration	Cal_hb.m
Optical reconstruction without *a priori*	recon_no_prior_bat.m
Build matlab mesh from comsol file with homogeneous absorption and scattering	Make_comsol_mesh.m
Time-multiplex system CCD data acquisition (three wavelengths) from 7 frames	getdata_mimages_3wv.m
Time-multiplex system CCD data acquisition (three wavelengths) from 1 frames	get_3wv_data.m
Time-multiplex system CCD acquired data calibration	Datafit_switch.m
Data fit to the reconstruction mesh	Cal_switch_nobak.m
Plot [HbT] and StO2 images (2 wavelengths)	show_2wv.m
Plot [HbT] and StO2 images (3 wavelengths)	show_3wv.m

```
function [data_reshape_b roi]=Cal_hb(b1,b2,er,nb)
% b1 is the first measurement, b2 is the last measurement;
G_b=30; %Gaussian fit bandwidth/2;
%% First calibrate background;
hb_t=zeros(512,512);
for i=b1:b2
   b_fn=strcat('b',num2str(i),'_1.txt');
   b1_1=load(b_fn);
   hb_t=hb_t+b1_1(:,2:513);
   clear b1_1 b_fn;
end;
hb1=hb_t/(b2-b1+1); %homogeneous background;
hb=hb1-nb; %nb is noise level;
clear hb_t hb1 min_hb bs be;

% pick up the 49 region of interest;
% Find detector first;
bd=30; %half of bandwidth of detecter to seperate
d_mean=mean(hb,2); %mean value along the detector;
d_center=zeros(1,7);
dm=zeros(1,7);
for i=1:7
   dm(i)=max(d_mean);
   d_center(i)=find(d_mean==max(d_mean));
   d_mean((d_center(i)-bd):(d_center(i)+bd))=0;
end;
d_mean=mean(hb,2);
d_center1=sort(d_center);
roi.dc=zeros(1,7); % center of detector;
roi.dw=zeros(1,7); % half of FWHM of Gaussian pulse;
for i=1:7
   x=(d_center1(i)-G_b):(d_center1(i)+G_b);
   x=x';
   y=d_mean(x);
   [g_a g_b g_c]=Gaussian_fit(x,y);
   roi.dc(i)=round(g_b);
   roi.dw(i)=round(sqrt(g_c*log(2)));
   clear x y;
end;
clear dm bd d_center d_center1 dm g_a g_b g_c;

% Second find source;
s_center=zeros(1,7);
s_mean=mean(hb,1); %mean value along the source;
bs=37; %half bandwidth of source to seperate;
sm=zeros(1,7);
```

```
for i=1:7
   sm(i)=max(s_mean);
   s_center(i)=find(s_mean==sm(i));
   if (s_center(i)-bs)<1
      x_min=1;
   else x_min=s_center(i)-bs;
   end;
   if (s_center(i)+bs)>512
      x_max=512;
   else x_max=s_center(i)+bs;
   end;
   s_mean(x_min:x_max)=0;
end;
s_mean=mean(hb,1);
s_center1=sort(s_center);
roi.sc=zeros(7,7); % center of detector;
roi.sw=zeros(1,7); % half of FWHM of Gaussian pulse;
for i=1:7
   x=(s_center1(i)-G_b):(s_center1(i)+G_b);
   y=s_mean(x);
   [g_a g_b g_c]=Gaussian_fit(x,y);
   roi.sc(:,i)=round(g_b);
   roi.sw(i)=round(sqrt(g_c*log(2)));
   clear x y;
end;
clear g_a g_b g_c;

data_aver=zeros(7,7);
for d=1:7;
   for s=1:7;
      data_aver(d,s)=sum_ellipse(hb,roi.sc(d,s),...
         roi.dc(d),roi.sw(s),roi.dw(d),er);
   end;
end;
data_reshape_b=fliplr(circshift(data_aver,[0,-3]))';
clear G_b bs d d_mean data_aver hb i j jj rj s s_center s_center1 s_center_offset s_mean
s_temp s_temp_mean sm;


function [a b c]=Gaussian_fit(x,y)


p=polyfit(x,log(y),2);
c=-1/p(1);
b=p(2)*c/2;
a=exp(p(3)+b^2/c);
```

recon_no_prior_bat.m

```
clear; clc; close all;

% Read out the calibration file.
load('roi.mat');

% Read out the test data files.
data_fold='C:\Documents and
Settings\OILmember\MyDocuments\MATLAB\2010_03_16\Op\';

% mi is the measured data sets at each locations
for c_i=1:18
   switch c_i
      case {1}
         content='Left_caudal_';
         mi=4;
      case {2}
         content='Left_cranial_';
         mi=6;
      case {3}
         content='Left_edge_caudal_';
         mi=4;
      case {4}
         content='Left_edge_cranial_';
         mi=5;
      case {5}
         content='Left_edge_mid_';
         mi=4;
      case {6}
         content='Left_mid_';
         mi=4;
      case {7}
         content='Left_muscle_';
         mi=3;
      case {8}
         content='Midline_caudal_';
         mi=5;
      case {9}
         content='Midline_cranial_';
         mi=4;
      case {10}
         content='Midline_mid_';
         mi=5;
      case {11}
         content='Right_edge_caudal_';
```

```
        mi=4;
    case {12}
        content='Right_edge_cranial_';
        mi=4;
    case {13}
        content='Right_edge_mid_';
        mi=4;
    case {14}
        content='Right_mid_caudal_';
        mi=4;
    case {15}
        content='Right_mid_cranial2_';
        mi=4;
    case {16}
        content='Right_mid_cranial_';
        mi=4;
    case {17}
        content='Right_mid_mid_';
        mi=6;
    case {18}
        content='Right_muscle_';
        mi=4;
end;
for meas_i=1 :mi
    fn_t=strcat(data_fold,content,num2str(meas_i));
    [t1 t2 t3]=getdata_mimages_3wv(fn_t,roi);
    data_1=(t1-roi.w1.noise).*roi.w1.cal;
    data_2=(t2-roi.w2.noise).*roi.w2.cal;
    data_3=(t3-roi.w3.noise).*roi.w3.cal;

%% Fitting background
    mesh_recon_fn='mesh_r';
    mesh_fd_fn='mesh_f';
    delete *mesh_f_mesh* *mesh_r_mesh*;
    Make_comsol_mesh(mesh_fd_fn,0.007,1.0); % 1% intralipid with solution ink).
    mesh=load_mesh('mesh_f_mesh');
    [mua_b_1 mus_b_1]=fit_slope(data_1,mesh,0);
    if mua_b_1<0.0025
        mua_b_1=0.0025;
    end;
    clear mesh;

    mesh=load_mesh('mesh_f_mesh');
    [mua_b_2 mus_b_2]=fit_slope(data_2,mesh,0);
    if mua_b_2<0.0025
        mua_b_2=0.0025;
```

```
        end;
        clear mesh;

        mesh=load_mesh('mesh_f_mesh');
        [mua_b_3 mus_b_3]=fit_slope(data_3,mesh,0);
        if mua_b_3<0.0025
           mua_b_3=0.0025;
        end;
        clear mesh;

%% Reconstruction for 1st wavelength;
        delete *mesh_r_mesh* *mesh_f_mesh*;
        Make_comsol_mesh(mesh_fd_fn,mua_b_1,mus_b_1);
        Make_comsol_mesh(mesh_recon_fn,mua_b_1,mus_b_1);
        delete *w1.paa*;
        mesh=load_mesh('mesh_f_mesh');
        Cal_switch_nobak(mesh, data_1, 0, 'w1.paa'); close;
        clear mesh data_1;

        out_fn_1=strcat(content,num2str(meas_i),'_1_out');
        regular=1;
        [mesh,pj_error,it] =
reconstruct_stnd_0('mesh_f_mesh','mesh_r_mesh',0,'w1.paa',10,regular,out_fn_1,0);
        clear mesh pj_error;
        while it<5
           regular=2*regular;
           [mesh,pj_error,it] =
reconstruct_stnd_0('mesh_f_mesh','mesh_r_mesh',0,'w1.paa',10,regular,out_fn_1,0);
        clear mesh pj_error
        end;

%% Reconstruction for 2nd wavelength;
        delete *mesh_r_mesh* *mesh_f_mesh*;
        Make_comsol_mesh(mesh_fd_fn,mua_b_2,mus_b_2);
        Make_comsol_mesh(mesh_recon_fn,mua_b_2,mus_b_2);
        delete *w2.paa*;
        mesh=load_mesh('mesh_f_mesh');
        Cal_switch_nobak(mesh, data_2, 0, 'w2.paa'); close;
        clear mesh data_2;

        out_fn_2=strcat(content,num2str(meas_i),'_2_out');
        regular=1;
        [mesh,pj_error,it] =
reconstruct_stnd_0('mesh_f_mesh','mesh_r_mesh',0,'w2.paa',10,regular,out_fn_2,0);
        clear mesh pj_error;
        while it<5
```

```
            regular=2*regular;
            [mesh,pj_error,it] =
reconstruct_stnd_0('mesh_f_mesh','mesh_r_mesh',0,'w2.paa',10,regular,out_fn_2,0);
        clear mesh pj_error;
        end;

%% Reconstruction for 3rd wavelength;
        delete *mesh_r_mesh* *mesh_f_mesh*;
        Make_comsol_mesh(mesh_fd_fn,mua_b_3,mus_b_3);
        Make_comsol_mesh(mesh_recon_fn,mua_b_3,mus_b_3);
        delete *w3.paa*;
        mesh=load_mesh('mesh_f_mesh');
        Cal_switch_nobak(mesh, data_3, 0, 'w3.paa'); close;
        clear mesh;

        out_fn_3=strcat(content,num2str(meas_i),'_3_out');
        regular=1;
        [mesh,pj_error,it] =
reconstruct_stnd_0('mesh_f_mesh','mesh_r_mesh',0,'w3.paa',10,regular,out_fn_3,0);
        clear mesh pj_error;
        while it<5
            regular=2*regular;
            [mesh,pj_error,it] =
reconstruct_stnd_0('mesh_f_mesh','mesh_r_mesh',0,'w3.paa',10,regular,out_fn_3,0);
        clear mesh pj_error;
        end;
    end;
end;
```

```
function Make_comsol_mesh(fn,mua,mus)

filename=strcat(fn,'.mphtxt');

%____Get number____%
[bd1 bd2 bd3 en] = Get_consol_numbers(filename);
data=comsol_node_read(filename);
domain=comsol_domain_read(filename,en);
elements=comsol_element_read(filename,en);%,577
bndtx=comsol_bnd_read(filename,bd1,bd2,bd3);

region_tmp=ones(length(data),1);

for j=1:length(elements)
   if (domain(j)==1 || domain(j)==2 || domain(j)==3)
      for i=1:4
         region_tmp(elements(j,i)+1)=1;
      end
   end
end

for j=1:length(elements)
   if (domain(j)==2 || domain(j)==3)
      for i=1:4
         region_tmp(elements(j,i)+1)=2;%prostate+blob
      end
   end
end

for j=1:length(elements)
   if (domain(j)==3)
      for i=1:4
         region_tmp(elements(j,i)+1)=3;%bg
      end
   end
end

%-------------------------------------------------------------------------%
mesh.name=strcat(fn,'_mesh');
mesh.dimension=3;
mesh.type='stnd';
%-------------------------------------------------------------------------%
elements(:)=elements(:)+1;
mesh.elements=elements;
mesh.nodes=data;
```

```
% %-------------------------------------------------------------------
mesh.region=region_tmp;

%----------------------set boundary-----------------------------------%

mesh.bndvtx=zeros(size(region_tmp));
mesh.bndvtx(bndtx+1)=1;

%----------------------set optical property---------------------------%
a=ones(size(mesh.nodes,1),1);
mesh.ri=1.33.*a;%reflect index

mesh.c=a;
mesh.mua=a.*mua;
mesh.mus=a.*mus;
mesh.kappa=1./(3.*(mesh.mua+mesh.mus));
%-------------------------------------------------------------------%
%----------------------sources and detectors--------------------------%
mesh.source.fixed=1;
mesh.meas.fixed=1;

mesh.source.coord(1,:)=[10 25 0];
mesh.source.coord(2,:)=[20 25 0];
mesh.source.coord(3,:)=[30 25 0];
mesh.source.coord(4,:)=[40 25 0];
mesh.source.coord(5,:)=[50 25 0];
mesh.source.coord(6,:)=[60 25 0];
mesh.source.coord(7,:)=[70 25 0];


mesh.meas.coord(1,:)=[10 45 0];
mesh.meas.coord(2,:)=[20 45 0];
mesh.meas.coord(3,:)=[30 45 0];
mesh.meas.coord(4,:)=[40 45 0];
mesh.meas.coord(5,:)=[50 45 0];
mesh.meas.coord(6,:)=[60 45 0];
mesh.meas.coord(7,:)=[70 45 0];

 for i=1:7
   mesh.link(i,:)=1:7;
end;
clear a data elements bndtx region_tmp domain bd1 bd2 bd3 en filename fn i j mua mus;
save_mesh(mesh,mesh.name);
```

```
 From imaging top to bottom is detector 1 2 3 4 5 6 7; detector 1 is on
% the top of the probe, detector 7 is closest to the handle.
% The sequence of the switch is Source 4 5 6 7 1 2 3 according to the
% position 1 2 3 4 5 6 7 (start - end) equal to source 4 5 6 7 1 2 3;
% Get each measurement for 7 images;
% fn_t is the measurement data converted from the *.spe to *.txt;
% roi is the location of the data spot on one image;

function [data1, data2, data3]=getdata_mimages_3wv(fn_t, roi)
n=length(roi.w1.dx);
data1_t=zeros(n,n); data2_t=zeros(n,n); data3_t=zeros(n,n);
for i=1:n
   t_fn=strcat(fn_t,'_',num2str(i),'.txt');
   [data1_t(i,:), data2_t(i,:), data3_t(i,:)]=get_3wv_data(t_fn, roi);
end;

data_reshape_1=circshift(data1_t,[-4,0]);
data_reshape_2=circshift(data2_t,[-4,0]);
data_reshape_3=circshift(data3_t,[-4,0]);

data1=zeros(n*n,1); data2=zeros(n*n,1); data3=zeros(n*n,1);
for i=1:n
   for j=1:n
      data1((i-1)*n+j)=data_reshape_1(i,j);
      data2((i-1)*n+j)=data_reshape_2(i,j);
      data3((i-1)*n+j)=data_reshape_3(i,j);
   end;
end;
```

```
% Get 3 wave data from single measurement;
% From imaging top to bottom is detector 1 2 3 4 5 6 7; detector 1 is on
% the top of the probe, detector 7 is closest to the handle.
% fn_t is the measurement data matrix
% roi is the location of the spot center and radius on one image;
% noise will be removed after function. Counted as 2 times mini-number.

function [data1 data2 data3]=get_3wv_data(meas_fn, roi)
meas1=load(meas_fn);
meas=meas1(:,2:513);
clear meas1;
% meas=meas-min(min(meas));

n=length(roi.w1.dx);
clear noise1 noise2;
signal_base=(roi.w1.noise+roi.w2.noise+roi.w3.noise)/3*2;

xcenter1=round(mean(roi.w1.dx));
xcenter2=round(mean(roi.w2.dx));
xcenter3=round(mean(roi.w3.dx));

rx1_sep=round(2*mean(roi.w1.rx));
rx2_sep=round(2*mean(roi.w2.rx));
rx3_sep=round(2*mean(roi.w3.rx));

image_1=meas(:,xcenter1-rx1_sep:xcenter1+rx1_sep);
image_2=meas(:,xcenter2-rx2_sep:xcenter2+rx2_sep);
image_3=meas(:,xcenter3-rx3_sep:xcenter3+rx3_sep);

%find the seperate point between each roi;
signal_power1=zeros(1,n);
signal_power2=zeros(1,n);
signal_power3=zeros(1,n);

for i=1:n
   %Check if the signal is too weak for wavelength1;

[s,pixel]=sum_ellipse_noise(meas,roi.w1.dx(i),roi.w1.dy(i),roi.w1.rx(i),roi.w1.ry(i),1,0);
   if s>=(pixel*signal_base)
      signal_power1(i)=1;
   end;


[s,pixel]=sum_ellipse_noise(meas,roi.w2.dx(i),roi.w2.dy(i),roi.w2.rx(i),roi.w2.ry(i),1,0);
   if s>=(pixel*signal_base)
```

```
        signal_power2(i)=1;
    end;


[s,pixel]=sum_ellipse_noise(meas,roi.w3.dx(i),roi.w3.dy(i),roi.w3.rx(i),roi.w3.ry(i),1,0);
    if s>=(pixel*signal_base)
        signal_power3(i)=1;
    end;
end;

roi_new.w1.dx=zeros(1,n);
roi_new.w2.dx=zeros(1,n);
roi_new.w3.dx=zeros(1,n);
roi_new.w1.dy=zeros(1,n);
roi_new.w2.dy=zeros(1,n);
roi_new.w3.dy=zeros(1,n);
roi_new.w1.sp=signal_power1;
roi_new.w2.sp=signal_power2;
roi_new.w3.sp=signal_power3;
% Locate the y coordinate for each image;
for i=1:n
    if ~roi_new.w1.sp(i)
        roi_new.w1.dy(i)=roi.w1.dy(i);
        roi_new.w1.ry(i)=roi.w1.ry(i);
        roi_new.w1.dx(i)=roi.w1.dx(i);
        roi_new.w1.rx(i)=roi.w1.rx(i);
    else
        temp_band=25;
        temp_x=roi.w1.dy(i)-temp_band:roi.w1.dy(i)+temp_band;
        temp_x=temp_x';
%         temp_data=ave_1(temp_x);
%         [g_a g_b g_c]=Gaussian_fit(temp_x,temp_data);
%         roi_new.w1.dy(i)=round(g_b);
        roi_new.w1.dy(i)=roi.w1.dy(i);
        roi_new.w1.ry(i)=roi.w1.ry(i);

        temp_image=image_1(temp_x,:);
        temp_data=mean(temp_image);
        temp_x=1:length(temp_data);
        [g_a g_b g_c]=Gaussian_fit(temp_x,temp_data);
        roi_new.w1.dx(i)=round(g_b)+xcenter1-rx1_sep-1;
        roi_new.w1.rx(i)=roi.w1.rx(i);
    end;

    if ~roi_new.w2.sp(i)
        roi_new.w2.dy(i)=roi.w2.dy(i);
```

```
        roi_new.w2.ry(i)=roi.w2.ry(i);
        roi_new.w2.dx(i)=roi.w2.dx(i);
        roi_new.w2.rx(i)=roi.w2.rx(i);
    else
        temp_band=25;
        temp_x=roi.w2.dy(i)-temp_band:roi.w2.dy(i)+temp_band;
        temp_x=temp_x';
%       temp_data=ave_2(temp_x);
%       [g_a g_b g_c]=Gaussian_fit(temp_x,temp_data);
%       roi_new.w2.dy(i)=round(g_b);
        roi_new.w2.dy(i)=roi.w2.dy(i);
        roi_new.w2.ry(i)=roi.w2.ry(i);

        temp_image=image_2(temp_x,:);
        temp_data=mean(temp_image);
        temp_x=1:length(temp_data);
        [g_a g_b g_c]=Gaussian_fit(temp_x,temp_data);
        roi_new.w2.dx(i)=round(g_b)+xcenter2-rx2_sep-1;
        roi_new.w2.rx(i)=roi.w2.rx(i);
    end;

    if ~roi_new.w3.sp(i)
        roi_new.w3.dy(i)=roi.w3.dy(i);
        roi_new.w3.ry(i)=roi.w3.ry(i);
        roi_new.w3.dx(i)=roi.w3.dx(i);
        roi_new.w3.rx(i)=roi.w3.rx(i);
    else
        temp_band=25;
        temp_x=roi.w3.dy(i)-temp_band:roi.w3.dy(i)+temp_band;
        temp_x=temp_x';
%       temp_data=ave_2(temp_x);
%       [g_a g_b g_c]=Gaussian_fit(temp_x,temp_data);
%       roi_new.w2.dy(i)=round(g_b);
        roi_new.w3.dy(i)=roi.w3.dy(i);
        roi_new.w3.ry(i)=roi.w3.ry(i);

        temp_image=image_3(temp_x,:);
        temp_data=mean(temp_image);
        temp_x=1:length(temp_data);
        [g_a g_b g_c]=Gaussian_fit(temp_x,temp_data);
        roi_new.w3.dx(i)=round(g_b)+xcenter3-rx3_sep-1;
        roi_new.w3.rx(i)=roi.w3.rx(i);
    end;
end;
clear g_a g_b g_c temp_image temp_x temp_data;
```

```
dx_offset=0; offset_count=0;
for i=1:n
   if roi_new.w1.sp(i)
      dx_offset=dx_offset+roi_new.w1.dx(i)-roi.w1.dx(i);
      offset_count=offset_count+1;
   end;
end;
if offset_count>=1
   dx_offset=round(dx_offset/offset_count);
   for i=1:n
      if ~roi_new.w1.sp(i)
         roi_new.w1.dx(i)=roi_new.w1.dx(i)+dx_offset;
      end;
   end;
end;

dx_offset=0; offset_count=0;
for i=1:n
   if roi_new.w2.sp(i)
      dx_offset=dx_offset+roi_new.w2.dx(i)-roi.w2.dx(i);
      offset_count=offset_count+1;
   end;
end;
if offset_count>=1
   dx_offset=round(dx_offset/offset_count);
   for i=1:n
      if ~roi_new.w2.sp(i)
         roi_new.w2.dx(i)=roi_new.w2.dx(i)+dx_offset;
      end;
   end;
end;

dx_offset=0; offset_count=0;
for i=1:n
   if roi_new.w3.sp(i)
      dx_offset=dx_offset+roi_new.w3.dx(i)-roi.w3.dx(i);
      offset_count=offset_count+1;
   end;
end;
if offset_count>=1
   dx_offset=round(dx_offset/offset_count);
   for i=1:n
      if ~roi_new.w3.sp(i)
         roi_new.w3.dx(i)=roi_new.w3.dx(i)+dx_offset;
      end;
   end;
```

```
end;

% roi_new.w1.theta=zeros(1,n); roi_new.w2.theta=zeros(1,n);
clear dx_offset image_1 image_2 offset_count rx1_sep rx2_sep rx_limit ry_limit s
signal_power1 signal_power2;
clear pixel temp_band xcenter1 xcenter2;

data1=zeros(1,n); data2=zeros(1,n); data3=zeros(1,n);
for i=1:n

data1(i)=sum_ellipse(meas,roi_new.w1.dx(i),roi_new.w1.dy(i),roi_new.w1.rx(i),roi_new
.w1.ry(i),1);

data2(i)=sum_ellipse(meas,roi_new.w2.dx(i),roi_new.w2.dy(i),roi_new.w2.rx(i),roi_new
.w2.ry(i),1);

data3(i)=sum_ellipse(meas,roi_new.w3.dx(i),roi_new.w3.dy(i),roi_new.w3.rx(i),roi_new
.w3.ry(i),1);
end;
clear pixel;
```

Function [roi]=getroi_three(fn_b)

```
hb_t=zeros(512,512);
for j=1:7
   b_fn=strcat(fn_b,'_',num2str(j),'.txt');
   b1_1=load(b_fn);
   hb_t=hb_t+b1_1(:,2:513);
   clear b1_1 b_fn;
end;
hb=hb_t/7; %Average of the 7 images;
clear hb_t hb1;

s_bd=30;
temp=mean(hb);
temp_max=max(temp);
temp_i=find(temp==temp_max);
temp(temp_i-s_bd:temp_i+s_bd)=0;
temp_max2=max(temp);
temp_i2=find(temp==temp_max2);
temp(temp_i2-s_bd:temp_i2+s_bd)=0;
temp_max3=max(temp);
temp_i3=find(temp==temp_max3);
temp_i_sort=sort([temp_i temp_i2 temp_i3]); %Three peak value of the three
wavelength;
sp=[round((temp_i_sort(1)+temp_i_sort(2))/2);
round((temp_i_sort(2)+temp_i_sort(3))/2)]; %Separate point of three bands;

clear temp_max temp_max2 temp_max3;

 imag_1=hb(1:512,1:sp(1)-1);
imag_2=hb(1:512,sp(1):sp(2)-1);
imag_3=hb(1:512,sp(2):512);

roi_1=findroi_center_new(imag_1,7);
roi_2=findroi_center_new(imag_2,7);
roi_3=findroi_center_new(imag_3,7);

roi_2.dx=roi_2.dx+sp(1);
roi_3.dx=roi_3.dx+sp(2);
roi.w1=roi_1; % 705nm;
roi.w2=roi_2; % 785nm;
roi.w3=roi_3; % 808nm;

%% Get the roi coodinate from one array;
```

```
function [roi]=findroi_center_new(hb,dn)


% hb is the given imaging array; n is the detector number;
% Modified for different rx and ry;

%% Find detector center in y dimension first;
bd=30; %half of bandwidth of detecter to seperate;
d_mean=mean(hb,2); %mean value along the detector;
d_center=zeros(1,dn);
dm=zeros(1,dn);
for i=1:dn
   dm(i)=max(d_mean);
   d_center(i)=find(d_mean==max(d_mean));
   if (d_center(i)-bd)<1
      d_min=1;
   else d_min=d_center(i)-bd;
   end;
   if (d_center(i)+bd)>length(d_mean)
      d_max=length(d_mean);
   else d_max=d_center(i)+bd;
   end;
   d_mean(d_min:d_max)=0;
   clear d_min d_max;
end;
d_mean=mean(hb,2);
d_center1=sort(d_center);

roi.dy=zeros(1,dn); % center of detector;
roi.ry=zeros(1,dn); % half of FWHM of Gaussian pulse;
G_b=20;
for i=1:dn
   x=(d_center1(i)-G_b):(d_center1(i)+G_b);
   x=x';
   y=d_mean(x);
   [g_a g_b g_c]=Gaussian_fit(x,y);
   roi.dy(i)=round(g_b);
   roi.ry(i)=round(sqrt(g_c*log(2)));
   clear x y;
end;
clear dm bd d_center d_center1 dm g_a g_b g_c i;

%Seperate the 7 detectors;
d1=zeros(dn-1,1);
for i=1:dn-1
```

```
    d1(i)=round((roi.dy(i)+roi.dy(i+1))/2);
end;

%% Find detector center in x dimension;
roi.dx=zeros(1,dn); roi.rx=zeros(1,dn);
x_b=30; %half bandwidth of source seperation;
for i=1:dn
    if i==1
        dx_begin=1; dx_end=d1(i);
    elseif i==dn
        dx_begin=d1(i-1); dx_end=512;
    else dx_begin=d1(i-1); dx_end=d1(i);
    end;
    dx_temp=hb(dx_begin:dx_end,:);
    dx_mean=mean(dx_temp);%mean value along the source;
    roi.dx(i)=find(dx_mean==max(dx_mean));
    if (roi.dx(i)-x_b)<1
        x_min=1;
    else x_min=roi.dx(i)-x_b;
    end;
    if (roi.dx(i)+x_b)>length(dx_mean)
        x_max=length(dx_mean);
    else x_max=roi.dx(i)+x_b;
    end;
    x=x_min:x_max;
    y=dx_mean(x);
    clear x_min x_max;
    [g_a g_b g_c]=Gaussian_fit(x,y);
    roi.dx(i)=round(g_b);
    roi.rx(i)=round(sqrt(g_c*log(2)));
%     plot(s_mean); hold on;
%     plot(x,g_a*exp(-(x-g_b).^2/g_c));
clear g_a g_b g_c x y;
end;
```

function [cal]=Datafit_switch(data)

```
% Calculate the source-detector distance (7 by 7);
cal=zeros(49,1);
mp=2; a=20; b=10;
dist=zeros(49,1);
for i=1:7
   for j=1:7
      dist((i-1)*7+j)=sqrt(a^2+(i-j)^2*b^2);
   end;
end;

mind=min(dist);
maxd=max(dist);
x=linspace(mind,maxd,100);
lnr2I=log(dist.^mp.*data);
[p q]=polyfit(dist,lnr2I,1); clear q;
y=p(1)*x+p(2);
plot(x,y); hold on;
plot(dist,lnr2I,'r+');
legend('linear fit','background data');
title(strcat('k=',num2str(-p(1))));
xlabel('Distance between source and detector (mm)');
ylabel('Ln(r^2I)');
for i=1:49
   cal(i)=exp(p(1)*dist(i)+p(2))/dist(i)^2/data(i);
end;

% Output [Cal] is a calibrated data array to be multiplied for the measured data.
```

```
%% Calibrate the measurement if we can measure a homo-background first;
% From imaging top to bottom is detector 1 2 3 4 5 6 7; detector 1 is on
% the top of the probe, detector 7 is closest to the handle.
% The sequence of the switch is Source 4 5 6 7 1 2 3 according to the
% position 1 2 3 4 5 6 7 (start - end);
function Cal_switch_nobak(mesh, meas, f, calfile)
% homodata is (49,1), averaged background measurement;
% mesh is the slope fitted mesh;
% meas is (49,1) measurement with the target;
% calfile is the calibrated data file of the target measurement;
% 'data_cal.paa';
data_fd=femdata(mesh,f);
data_am=data_fd.amplitude;
mp=2; a=20; b=10;
dist=zeros(49,1);
for i=1:7
   for j=1:7
      dist((i-1)*7+j)=sqrt(a^2+(i-j)^2*b^2);
   end;
end;
lnr2I=log(dist.^mp.*data_am);
[p q]=polyfit(dist,lnr2I,1); clear q;

data_cal=zeros(49,1); max_temp=zeros(49,1);
for i=1:49
   max_temp(i)=(exp(p(1)*dist(i)+p(2)))/dist(i)^2;
%     data_cal(i,1)=meas(i)/max_temp(i)/data_am(i);
end;
% dc_offset=max(data_fd.amplitude)/max(data_cal);
dc_offset=max(max_temp(i))/max(meas(:,1));
for i=1:49
   data_cal(i)=meas(i,1)/(max_temp(i)/data_am(i));
end;
data_fd.amplitude=data_cal*dc_offset;
data_fd.paa(:,1)=data_cal*dc_offset;
plot(data_am); hold on;
plot(data_fd.amplitude,'r-');
legend('Mesh background','Calibrated Data');
% dc_offset=mean(data_fd.amplitude)/mean(meas(:,1));
% data_fd.amplitude=meas(:,1)*dc_offset;
% data_fd.paa(:,1)=meas(:,1)*dc_offset;
save_data(data_fd,calfile);
```

Plot the total Hb image (Codes for two wavelength)

```
% Calculate the HbO and Hb
clear; clc; close all;
data_meas_fn='left_edge3_6';
out_fn_1=strcat(data_meas_fn,'_1_out');
out_fn_2=strcat(data_meas_fn,'_2_out');
mesh_1 = read_solution('mesh_f_mesh',out_fn_1); %785nm
close;
rasterize_mua(mesh_1,'y',35);
% % % %
mesh_2 = read_solution('mesh_f_mesh',out_fn_2); %830nm
close;
% figure(2);
rasterize_mua(mesh_2,'y',35);
%
% rasterize_mus(mesh_1,'y',35);
% rasterize_mus(mesh_2,'y',35);
% %
mua_1=mesh_1.mua; mua_2=mesh_2.mua;

e_1_hbo=(73.08+74)/2*log(10);
e_1_hb=(99.672+95.736)/2*log(10);
e_2_hbo=105.8*log(10);
e_2_hb=69.132*log(10);

hbo=(mua_1.*e_2_hb-mua_2.*e_1_hb)./(e_1_hbo*e_2_hb-e_2_hbo*e_1_hb);
hb=(mua_1.*e_2_hbo-mua_2.*e_1_hbo)./(e_1_hb*e_2_hbo-e_2_hb*e_1_hbo);
HbT=hbo+hb;
StO2=hbo./HbT*100;
%
%
mesh=load_mesh('mesh_f_mesh');
mesh.mua=HbT;
% figure(3);
% rasterize_mua(mesh,'y',35);
rasterize_mua(mesh,'x',30);

mesh.mua=StO2;
figure(2);
% rasterize_mua(mesh,'y',35);
rasterize_mua(mesh,'x',30);
```

Plot the total Hb image (Codes for two wavelength)

```
clear; clc; close all;

data_meas_fn='Right_muscle_3';
out_fn_1=strcat(data_meas_fn,'_1_out');
out_fn_2=strcat(data_meas_fn,'_2_out');
out_fn_3=strcat(data_meas_fn,'_3_out');

mesh_1 = read_solution('mesh_f_mesh',out_fn_1); %705nm
close;
rasterize_mua(mesh_1,'y',35);
% % % %
mesh_2 = read_solution('mesh_f_mesh',out_fn_2); %785nm
close;
rasterize_mua(mesh_2,'y',35);

mesh_3 = read_solution('mesh_f_mesh',out_fn_2); %808nm
close;
rasterize_mua(mesh_3,'y',35);

mua_1=mesh_1.mua; mua_2=mesh_2.mua; mua_3=mesh_3.mua;

e_1_hbo_human=298/10*log(10);
e_1_hb_human=1687.76/10*log(10);
e_2_hbo_human=730.8/10*log(10);
e_2_hb_human=996.72/10*log(10);
e_3_hbo_human=844/10*log(10);
e_3_hb_human=730.28/10*log(10);

e_1_hbo=e_1_hbo_human;
e_1_hb=e_1_hb_human;
e_2_hbo=e_2_hbo_human;
e_2_hb=e_2_hb_human;
e_3_hbo=e_3_hbo_human;
e_3_hb=e_3_hb_human;

extc_3=[e_1_hbo e_1_hb; e_2_hbo e_2_hb; e_3_hbo e_3_hb];

clear e_1_* e_2_* e_3_*;



F=[mua_1'; mua_2'; mua_3'];
Hb_both=(extc_3'*extc_3)\extc_3'*F;
```

```
hbo=Hb_both(1,:)';
hb=Hb_both(2,:)';

HbT=hbo+hb;
StO2=hbo./HbT*100;

mesh=load_mesh('mesh_f_mesh');
mesh.mua=HbT;
rasterize_mua(mesh,'y',35);
% errorbar(HbT_i,y_HbT,E_HbT,'xr'); hold on;

figure(2);
mesh.mua=StO2;
rasterize_mua(mesh,'y',35);
```

A.4 Current *in-vivo* canine imaging procedure:

The entire procedure of *in-vivo* canine prostate imaging is described in Fig. 83.

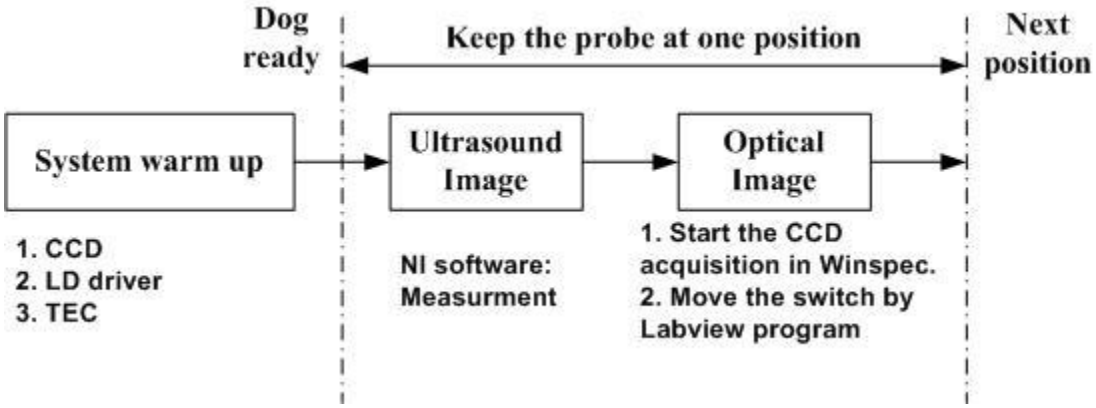

Figure 83 *in-vivo* canine prostate imaging procedure

A.4.1. System warm up

This step includes the warm up of CCD, LD driver and TEC module which may take 20 ~ 30 minutes to ensure a stable system response.

The motor stage also needs to be initialized after power on as Fig. 84.

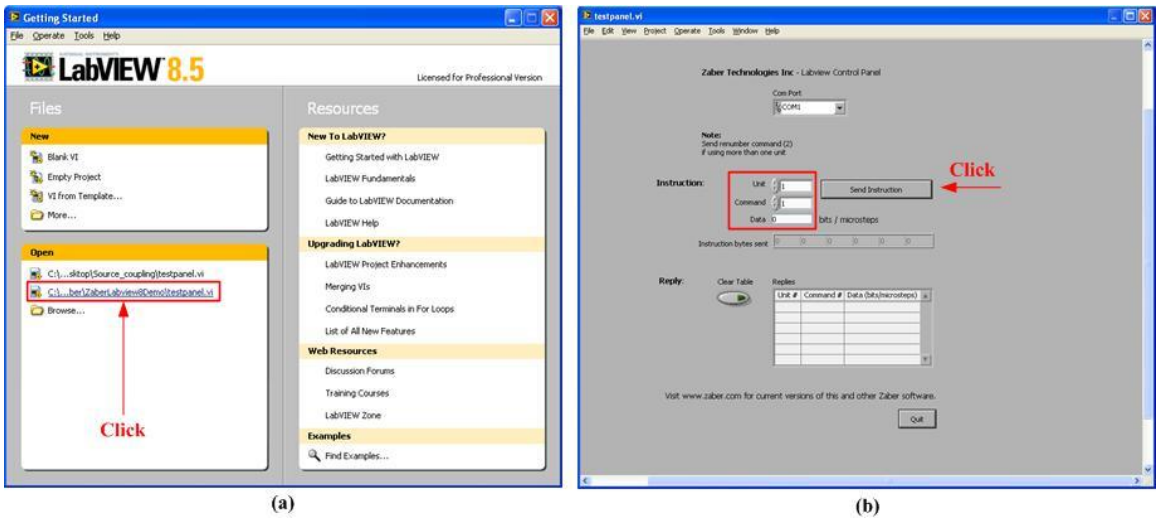

Figure 84 Labview program to initialize the motor stage

The unit and command values are both set to “1” then the data value is neglected.

Some initial parameters of Winspec are set as Fig. 85:

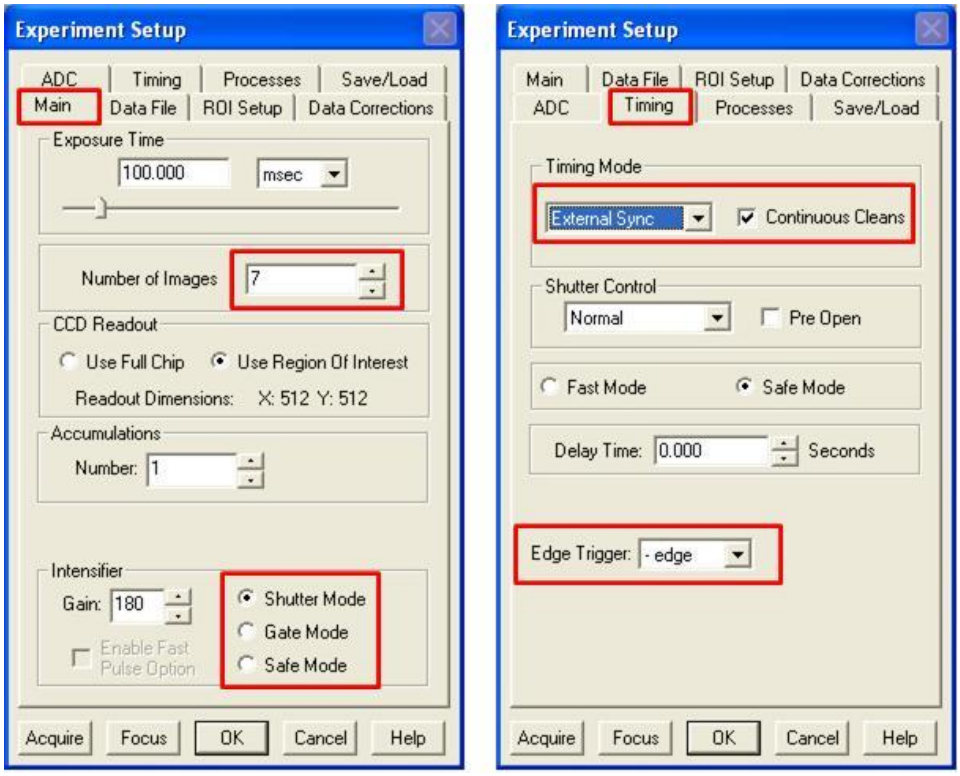

Figure 85 Winspec setting

In the “Main” tag, the number of Images is set to “7”. In the “Timing” tag, “Timing Mode” is set to “External Sync” with “Continuous Cleans; the “Edge Trigger” uses negative trigger edge.

A.4.2. When dog is anesthetized, keep the probe at one position:

A.4.2.2.1 Take the ultrasound images first by NI software: Measurement & Automation Explorer:

Select NI-IMAQ devices----imag0: NI PCI-1405----Channel 0: rs170

Then click “Grab”.

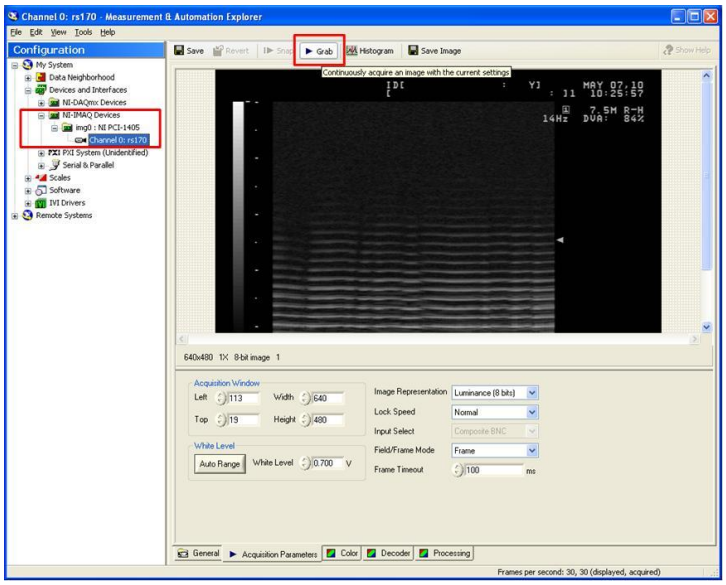

Figure 86 NI measurement and Automation Explorer

A.4.2.2.2 Start the CCD acquisition by Winspec, then trigger the motor stage by Labview program shown in Fig. 87. Change the default folder to if the position data file is different. Then click the “Run” button and the program will first need to select the position data file and the motor stage will move afterward.

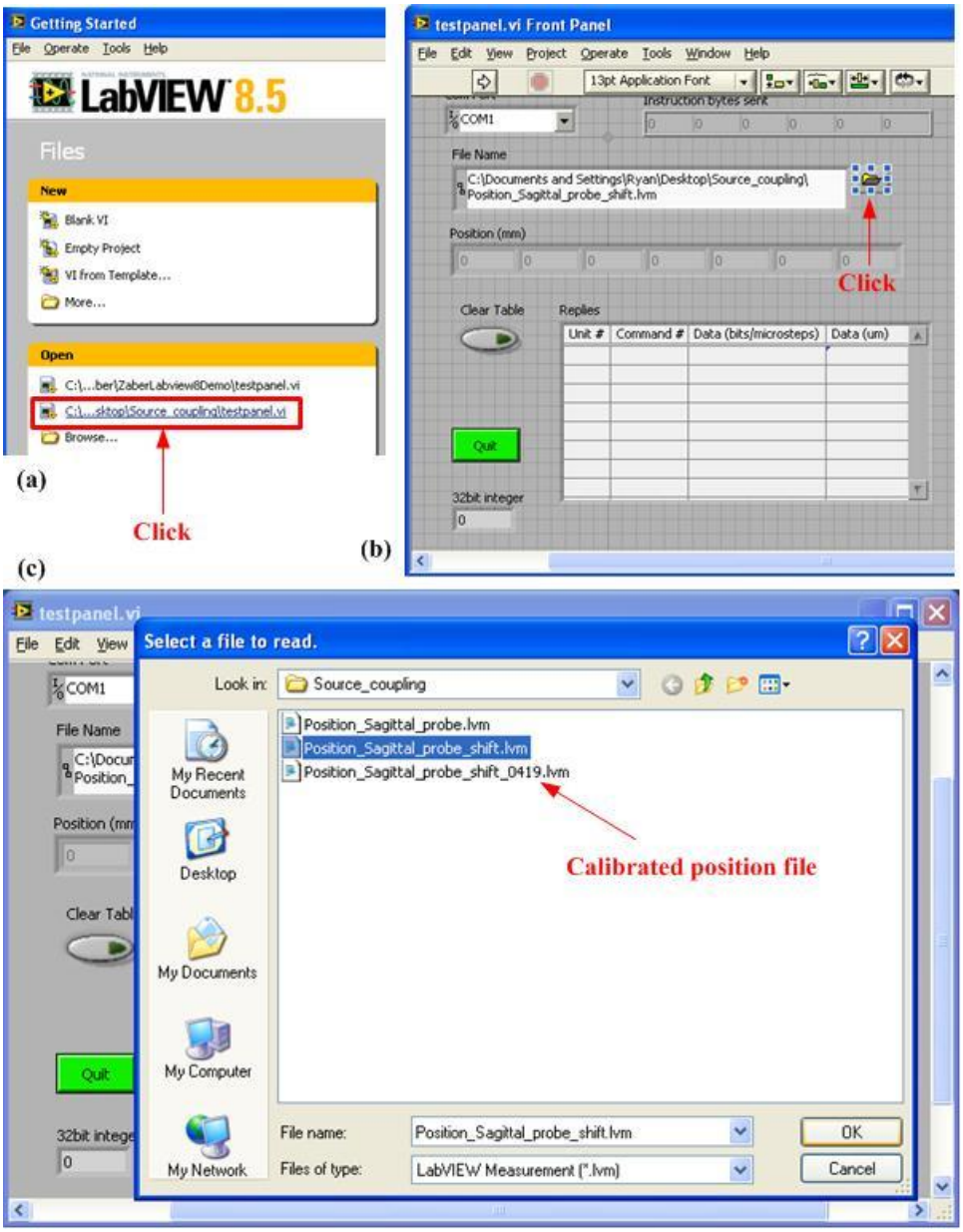

Figure 87 Labview program for CCD data acquisition

A.4.2.2.3 The measured data by Winspec is in the format of *.spe file. In order to use the Matlab based reconstruction algorithm to calculate, the file has to be converted to text file format which is shown in Fig. 88

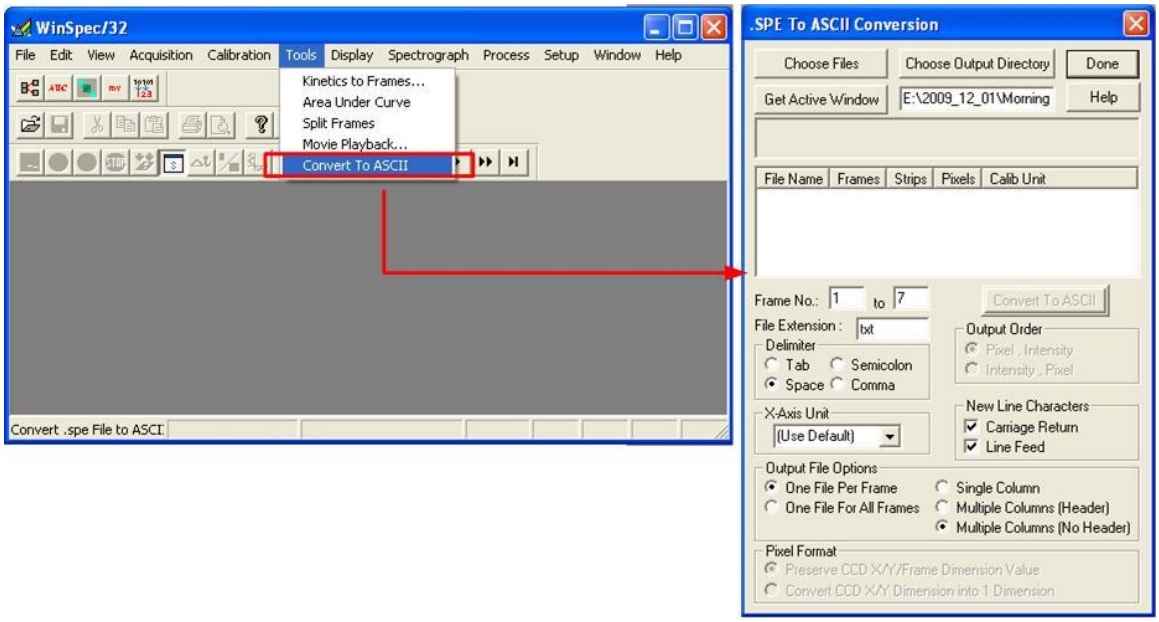

Figure 88 Winspec files output to text files

VITA

Zhen Jiang

Candidate for the Degree of

Doctor of Philosophy

Thesis: STUDY OF TRANS-RECTAL NEAR-INFRARED OPTICAL TOMOGRAPHY CONCURRENT WITH TRANS-RECTAL ULTRASOUND FOR PROSTATE IMAGING

Major Field: Electrical Engineering

Biographical:

Education:

Doctor of Philosophy in Electrical Engineering at Oklahoma State University, Stillwater, Oklahoma in July, 2010.
Master of Science in Microwave Engineering at Southeast University, Nanjing, China, 2005.
Bachelor of Science in Electronics and Information technology at Southeast University, Nanjing, China, 1998.

Experience:

Hardware Engineer	2006
Siemens Program and System Engineering Co., Ltd, Nanjing, China	
RF Engineer	2005
Huawei Technology, Shanghai, China	
Electrical Engineer	1998-2002
China Telecom Planning and Designing Institute (Jiangsu)	

Professional Memberships:

The International Society for Optical Engineering (SPIE)	2006—present
Optical Society of America (OSA)	2006—present

Name: Zhen Jiang Date of Degree: July, 2010

Institution: Oklahoma State University Location: Stillwater, Oklahoma

Title of Study: STUDY OF TRANS-RECTAL NEAR-INFRARED DIFFUSE OPTICAL TOMOGRAPHY CONCURRENT WITH TRANS-RECTAL ULTRASOUND FOR PROSTATE IMAGING

Pages in Study: 164 Candidate for the Degree of Doctor of Philosophy

Major Field: Electrical Engineering

Scope and Method of Study:

The objective of this study is to develop an endo-rectal NIR imaging probe coupled with TRUS in sagittal plane. The successful outcome of this research will find a way to improve the imaging contrast and help radiologists to locate the suspicious lesions in prostate which will ultimately improve the biopsy accuracy.

The combined system using an endo-rectal near-infrared (NIR) applicator integrated with a trans-rectal ultrasound (TRUS) probe is demonstrated. A continuous-wave (CW) NIR optical tomography system is integrated with a commercial US scanner to form the dual-modality imager. Sagittal trans-rectal imaging is performed concurrently by endo-rectal NIR and TRUS.

Findings and Conclusions:

The TRUS coupled trans-rectal NIR sagittal imaging probe is fabricated. The CW optical measurement demonstrated the quantitative estimation of the optical absorption coefficient is feasible when incorporating the TRUS *a priori* information. The use of condom is found to have minimum effects on NIR tomography measurement. Absorptive targets can also be recognized by optical stand-alone reconstruction which demonstrates the potential of finding targets ambiguous to US imaging.

In-vivo imaging of normal canine prostate and TVT tumors in the canine pelvic canal was performed by trans-rectal NIR tomography coupled with TRUS. The TVT tumor nodules were presented as hyper-absorption and hyper-scattering with respect to the normal prostatic and other pelvic tissues. Correlation of the TVT locations is found between trans-rectal NIR and TRUS images.

Dual-band *in-vivo* imaging of canine prostate with TVT tumors demonstrated a non-invasive optical measurement of [HbT] changes associated with tumor development. Using trans-rectal US-coupled spectral optical tomography the development and lateral involvement of the prostate cancer was detected earlier than using TRUS alone.

ADVISER'S APPROVAL: _____